FACULTY OF SCIENCE AND TECHNOLOGY

BACHELOR'S THESIS

Study programme / specialisation: Mechanical engineering/material science	The *spring* semester, *2023* Open / ~~Confidential~~
Author: Fana Tewelde	
Supervisor at UiS: Vidar Hansen Co-supervisor: Mats Ingdal	
Thesis title: Microstructure and mechanical properties of 3D-printed aluminium bronze	
Credits (ECTS): 20	
Keywords: Additive manufacturing Aluminium bronze Microstructure Mechanical properties	Pages: 79 + appendix: 10 Stavanger, *15.05.2023*

Abstract

Additive manufacturing has been growing rapidly in several industries since the late 1980s. In this thesis, mechanical properties and microstructure of a 3D-printed aluminum bronze have been investigated. Mechanical properties were identified through tensile tests, Charpy V tests and Vickers hardness tests. Microstructural investigation was done with optical microscope and SEM, including EBSD and EDS. The results obtained from the tensile test and Charpy V test should be considered as a preliminary indication rather than absolute representative for the aluminum bronze. This is due to certain errors that occurred during testing. Additional testing should have been performed to obtain more accurate and representative results. However, it was difficult to perform additional testing, due to the limited available material.

The three Charpy V tests that were carried out showed that the aluminum bronze mean absorbed energy were 33,7J, and the standard deviation was 11. For the three tensile test that was performed, it was found that the yield strength at 0,2% offset was 204,9MPa with standard deviation of 1,69. The mean tensile strength was found to be 533,0MPa with standard deviation of 3. The mean elongation at break was found to be 57,7% with standard deviation of 5,29, but the property was found to be approximately 45% when measuring manually. The modulus of elasticity varied quite a lot between test specimens, due to measuring errors. With SEM investigation performed on the fractured surfaces, ductile microstructural properties were observed. Almost a total of 1000 hardness indenters were done. The results showed that the material was hardest at the bottom near the base that the metal was 3D-printed onto. The mean hardness value measured was 135 with standard deviation of 10,4.

Dendritic structures were observed in the optical microscope. They were investigated further to determine the local solidification rate in the top and bottom part of the material. It was found that the cooling rate was 5,5% faster in the bottom than at the top.

With SEM and EDS analysis, it was possible to observe the iron-rich κ precipitates that were observed over larger regions, especially at the grain boundary areas. Additional time would be needed in order to get good results in the EBSD analysis, as certain areas were not diffracting. However, the FCC crystal structure were observed.

Abbreviations

AM	Additive manufacturing
APF	Atomic packing factor
BD	Building direction
CVT1	Charpy V test specimen 1
CVT2	Charpy V test specimen 2
CVT3	Charpy V test specimen 3
DED	Direct energy deposition
EBSD	Electron backscatter diffraction
HAZ	Heat affected zone
LD	Linear density
PBF	Powder bed fusion
PD	Planar density
SLM	Selective laser melting
SDAS	Secondary dendrite arm spacing
TT1	Tensile test specimen 1
TT2	Tensile test specimen 2
TT3	Tensile test specimen 3

List of content

List of figures

List of tables

Acknowledgement

I would like to thank my supervisor, Professor Vidar Hansen for his guidance, support and feedback through the duration of my thesis. I am also grateful for Sture Sørli and the team at NAM for providing me with the necessary materials to conduct my thesis. I also want to thank Johan Andreas Thorkaas for all the help and guidance in the lab and workshop, and A to Mats Ingdal for helping me with etching and in the lab. Further, a thank you to Wakshum Tucho for helping me with the SEM analysis, and Kjetil Høgemark for his help in preparing testing specimens.

Finally, I would like to thank my family and friends for the support, encouragement, and patience during this challenging yet instructive period.

All figures presented in this thesis, except Figure 2.10 and Figure 2.12 have been made by me in PowerPoint, Excel and Autodesk Inventor.

1. Introduction

Many manufacturing companies seek to automate production, minimizing waste, and achieve a more cost- and time-efficient production. Additive manufacturing (AM), also known as 3D-printing, is a growing manufacturing process that started in the late 1980s [5]. Today, several AM techniques are used in a variety of different industries. This revolutionary technique of manufacturing materials differs from traditional manufacturing processes like casting in that components are built by adding layers of material on top of each other instead of subtracting to get the desired shape and geometry. Some of the major advantages with AM is the flexibility that lies with the techniques regarding design, which allows for complex shaped components to be generated.

The metallic alloy studied in this thesis was a 3D-printed aluminum bronze delivered by Nordic additive manufacturing (NAM). NAM is a Norwegian manufacturing company based in Raufoss in the eastern part of Norway. They 3D-print metallic components using direct energy deposition (DED), which is an AM technique. NAM 3D-prints propellers of aluminum bronze for maritime- and offshore industries.

Aluminum bronze, which is a copper-based alloy, is known for its good mechanical properties, excellent resistance to corrosion and cavitation-erosion, which makes it suitable for maritime and offshore environments. Despite the attractive properties of aluminum bronze, the demand of the metallic alloy did not grow fast before after the second world war. The growing offshore oil industry led to the demand for propellers for larger and faster ships, and the need for strong and corrosion resistant alloy for submarines. Today, both casted and wrought aluminum bronze are used in components in marine- and offshore industries [3]. Other typical applications for aluminum bronze are pumps, valves, and bearings [6].

Even though AM is growing and used more and more in different industries, it is important to make sure that proper research and investigation is done to the mechanical properties and microstructure of the printed material. That is also what NAM wanted for the aluminum bronze. The aim of this thesis was therefore to investigate the microstructure and mechanical properties of the 3D printed aluminum bronze.

SINTEF is a Norwegian research institute with special expertise in technology, natural science and social science [7]. They performed certain mechanical tests on the same type of aluminum bronze as worked on in this thesis for NAM. Some of the results that SINTEF got will also be compared to the results obtained in this thesis.

2. Theory

2.1 Additive manufacturing

Additive manufacturing (AM) includes several different 3D-printing techniques used to build objects and components. The development of this revolutionary manufacturing method started in late 1980s and is still growing in different industries. Automotive, aircraft, aerospace, offshore constructions and components, architecture, biomedical and in clothes and shoe industries are among them [5] [8]. Unlike most conventional, subtractive manufacturing processes, AM builds 3D objects by adding layers of matter, instead of removing parts until getting the desired geometry. It gives the opportunity to build new component, add material to an already existing part or repairs. There are different types of AM, but they all share the same main processing steps. First, a 3D-model of the component that is going to be created is generated in a computer-aided design (CAD) software. Then, the model is converted into a SRL file format where the geometry of the solid model's surface is defined. Another software is then used to slice the model horizontally into layers. These layers are the path that the 3D-printer uses to print the component [8].

Different technologies and materials can be used in AM. One may classify two main metallic AM methods: powder bed fusion (PBF) and direct energy deposition (DED) [8]. The main difference between them lies in the way the feedstock is deposited. This paper will focus on DED, but a small introduction to PBF will be given in the following subchapter.

2.1.1 Powder bed fusion

With PBF, fine, pulverized metal from the powder stock is being laid over a specified surface or build platform, usually with a thickness of 0,1mm. A roller or blade is then used to distribute the material over the platform. After one layer is laid, a laser or electron beam scans over specific parts of the deposited powder, which melts and fuses it together. A new layer of pulverized material is added over the previous one and fused in the same way as the first layer. This process is repeated until the desired object is formed [9]. The remaining unfused powder is removed and may be reused after undergoing a recovery process [8]. A schematic illustration of PBF is shown in Figure 2.1. Large temperature gradient occurs in PBF. This means that the melting and solidification process is happening rapidly, which affects microstructural features and mechanical properties of metals built with PBF.

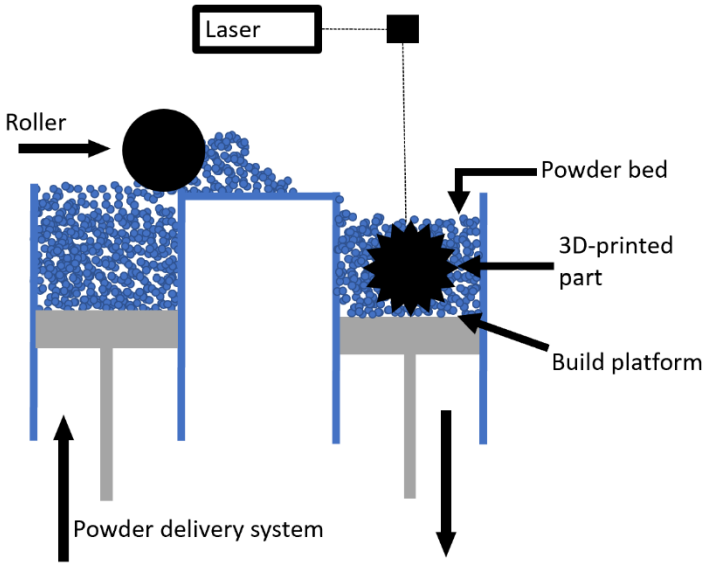

Figure 2.1 Schematic illustration of PBF.

2.1.2. Direct energy deposition

DED is a more complex AM technique than PBF. It is similar to PBF in the sense that a concentrated heating source is used to melt the metal. However, with DED the feeding and melting is happening at the same time. The material feedstock, which is either in powder or wire form, gets deposited through a nozzle to a base or directly onto the surface of an already existing component. As the material is exiting the nozzle, it is simultaneously melted by a laser, electron beam or a plasma arc [10]. The nozzle is fixed on a multiaxial arm, which makes it flexible to move in different directions and deposit metal in as good as any angle. Layer upon layer of defined thickness is laid in a specific direction. The deposition rate through the nozzle and the voltage through the heat source is specified to create complex shaped components. DED processes are usually carried out in a controlled chamber with reduced oxygen levels. Using electron beam as heat source requires the process to happen in vacuum. To prevent the deposit from oxidizing, shield gas is added to the metal as it gets deposited [11]. DED schematic illustration is shown in Figure 2.2.

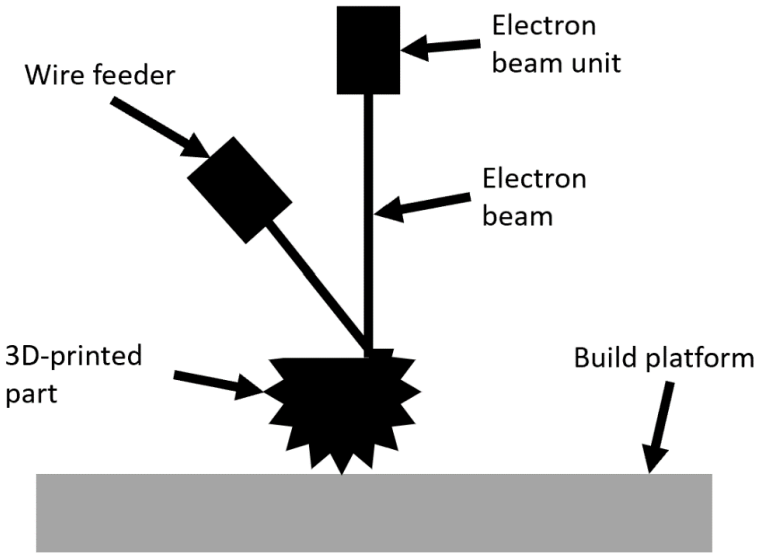

Figure 2.2 Schematic illustration of DED.

The microstructure and mechanical properties of a 3D-printed metal are affected by the printing method. Chemical in homogeneities and pores usually appears in different scales. The heat source also causes previous deposited layers to remelt and resolidify, which causes changes to the microstructure and mechanical properties [8].

2.1.3 Additive manufacturing vs conventional manufacturing

There are great benefits with AM compared to conventional manufacturing, such as casting. It allows for the creation of complex shaped components, which gives the opportunity for optimizing the design of parts and increase performance. Conventional manufacturing methods subtracts material to get the desired shape and geometry, which results in waste material. With AM, little to no waste material is produced, which makes it more economically and environmentally friendly. Additionally, the ease of design and modifications possibilities in CAD-systems, can make the production more time and cost efficient.

Some disadvantages are important to acknowledge with AM compared to conventional manufacturing. Creating bigger components are usually beneficial to produce with conventional manufacturing methods [8]. Further, when it comes to the variety of materials available for AM, there are some limitations. This is also the case for color options and finishing touches. One of the biggest and important difference with AM produced components are their mechanical properties. Usually, conventional manufactured parts have better mechanical properties than AM components [8].

2.2 Crystal structure of metals

The way the atoms are arranged in metals depends on the present atoms, nature of the bonds between the atoms, and the temperature. The microstructure is either randomly ordered, known as amorphous structure, or arranged in a specific, repetitive way, known as crystalline structure [12].

Most metals and metallic alloys form crystalline structures in the solid state at room temperature. The atoms or molecules are arranged in a periodic repetitive three-dimensional order that forms a space lattice, which is illustrated in Figure 2.3. Each interaction of the lines in the space lattice are called lattice point and represents an atom or a molecule. They refer to points in space with identical surroundings. A space lattice is built up of a number of small, repeat entities known as unit cells. They are usually shaped like parallelepipeds or prisms. In **Feil! Fant ikke referansekilden.**, one unit cell is highlighted in blue. All the other unit cells in the space lattice are identical to this blue unit cell [12] [8].

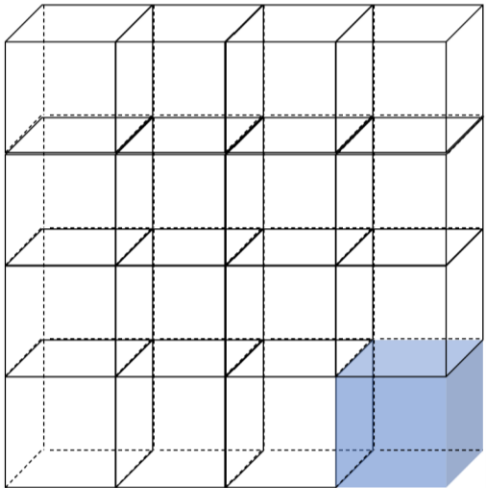

Figure 2.3 Space lattice built up of multiple unit cells. One of the unit cells is highlighted in blue.

Construction metals are polycrystalline, which means that the material is built up of different crystal structures. This causes variation in the material's behavior and mechanical properties. It is therefore worth looking into some of the common lattice structures that often appear in metals.

The different lattice structures are called Bravais lattices. They are categorized by the way in which the atoms are arranged. The lattice constants, a, b and c and the interaxial angles α, β and ϒ are used to specify the geometry of a unit cell. Most metals solidify into face-centered cubic crystal lattice (FCC), body-centered cubic crystal lattice (BCC), or hexagonal close-packed crystal lattice (HCP) [8] [12]. Figure 2.4 illustrates the unit cell of these three crystal structures.

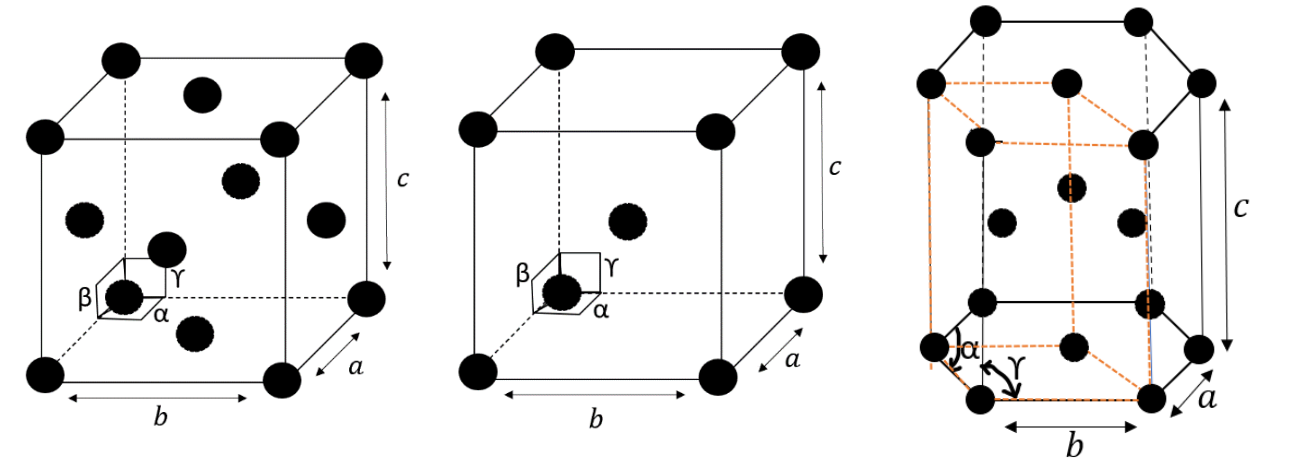

Face-centered cubic crystal structure (FCC) unit cell. $a = b = c$ and $\alpha = \beta = \Upsilon = 90°$	Body-centered cubic crystal structure (BCC) unit cell. $a = b = c$ and $\alpha = \beta = \Upsilon = 90°$	Hexagonal close-packed crystal structure (HCP) unit cell (three unit cells). $a = b \neq c$ and $\alpha = \beta = 90°, \Upsilon = 120°$

Figure 2.4 Unit cells for FCC, BCC and HCP.

FCC crystal structured materials are known for having good ductile properties. With this crystal structure, one atom is located at each of the eight corners and one on each of the six cube faces. This is the densest packed crystal structure for hard spheres with the same radius, therefore also referred to as close-packed structure. This will be further explained in this chapter. Each of the atoms located at the corners are shared with eight other neighboring unit cells, and the atoms located at the faces are shared with one adjacent unit cell. This results in a total of four atoms within an FCC unit cell. The length of the unit cell edges (a, b and c) are the same and related to the radius of the atom R in the following way:

$$a = b = c = 2 * R * \sqrt{2} \tag{2.1}$$

Since the length of a unit cell edges are dependent on the atomic radius, the size of a unit cell is dependent on the present elements in the material.

The atomic packing factor (APF) is a measure of how much of the total volume of a unit cell that has been occupied by atoms, assuming hard spheres. The formula for APF is as following:

$$APF = \frac{total\ volume\ of\ the\ atoms\ in\ the\ unit\ cell}{volume\ of\ the\ unit\ cell} \tag{2.2}$$

From Equation (2.2), one can find the APF for FCC in the following way, assuming hard sphere atoms with same radius:

$$APF_{FCC} = \frac{4 * \left(\frac{4}{3}\pi R^3\right)}{\left(2R\sqrt{2}\right)^3} = 0{,}74$$

This means that 74% of the total FCC unit cell volume is occupied by atoms. This is the most efficient (highest possible APF) packing for hard sphere atoms of equal sizes.

For BCC crystal structure, one atom is located at each corner and one atom at the center. This gives a total of two atoms within a BCC unit cell. The unit cell edges for BCC are of same length and related to the atomic radius in the following way [8]:

$$a = b = c = \frac{4*R}{\sqrt{3}} \qquad (2.3)$$

APF for BCC is as following, assuming hard sphere atoms with equal radius:

$$APF_{BCC} = \frac{2 * \left(\frac{4}{3}\pi R^3\right)}{\left(\frac{4R}{\sqrt{3}}\right)^3} = 0{,}68$$

Which means that 68% of the total BBC unit cell volume is occupied by atoms.

HCP is another common crystal structure, which has a hexagonal shaped unit cell. Six atoms are located on the top and bottom face, which are shared with six other neighboring unit cells. Additionally, three atoms are located on a crystallographic plane in between the two outer planes. This gives a total of six atoms within a HCP unit cell. As indicated in figure ++, the unit cell length a and b are the same, but not equal to c. According to D.W Callister and D.G. Rethwisch [8], the unit cell lengths in HCP are often related to each other in the following way :

$$\frac{c}{a} = 1{,}633 \qquad (2.4)$$

Knowing that the area of a hexagonal surface plane (Figure 2.5) is equal to $\frac{3\sqrt{3}}{2} * (side\ length)^2$, and $c = 1{,}633 * a = 1{,}633 * 2R$, the APF for HCP is

$$APF_{HCP} = \frac{6 * \left(\frac{4}{3}\pi R^3\right)}{\left(\frac{3\sqrt{3}}{2}(2R)^2\right) * (1{,}633 * 2R)} = 0{,}74$$

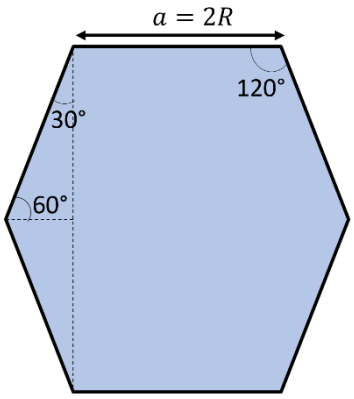

Figure 2.5 HCP surface plane.

HCP crystal structure is therefore referred to as closed-packed.

2.2.1 Point, direction, and planes within unit cells

Points, directions, and planes within a unit cell is often necessary to specify when studying metals. In this section, the focus will be on cubic unit cells. To specify specific points, also called lattice positions, three lattice position coordinates are used. They are linked to the x, y and z axes by which the origin is located at one of the corners in the unit cell. To find the coordinates, three-point indices, which can be named d, e, and f, are used as fractions of the unit cell lengths, a, b and c respectively. In other words, the lattice position coordinates, which can be named LP_x, LP_y and LP_z, can be expressed in the following way [8]:

$$LP_x = d * a \quad (2.5)$$
$$LP_y = e * b \quad (2.6)$$
$$LP_z = f * c \quad (2.7)$$

Figure 2.6 shows three lattice points and their respective point coordinates within a unit cell.

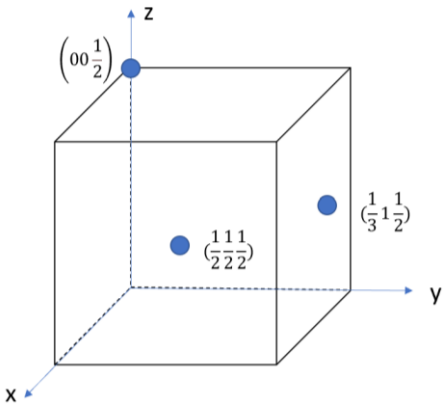

Figure 2.6 Lattice positions in a cubic unit cell.

Regarding crystallographic directions within a unit cell, a vector is specified by using the same coordinate system as for lattice positions. A direction coordinate, which can be called $[g, h, i]$, that has a start and an end point with the coordinates $(LP_1 LP_1 LP_1)$ and $(LP_2 LP_2 LP_2)$ respectively will have a crystallographic direction that is determined by the following way [8]:

$$g = q * \left(\frac{LP_2 - LP_1}{a}\right) \quad (2.8)$$
$$h = q * \left(\frac{LP_2 - LP_1}{b}\right) \quad (2.9)$$
$$i = q * \left(\frac{LP_2 - LP_1}{c}\right) \quad (2.10)$$

Where a, b and c are the unit cell lengths, and q is a constant that may be required to obtain a direction expressed with the smallest possible integers. Figure Figure 2.7 shows different crystallographic directions within a cubic unit cell. Negative coordinates are expressed with a line above the index. Using Equation (2.1) and Equation (2.3), one can for instance calculate the length of the [111] direction in FCC a BCC unit cell respectively in the following way:

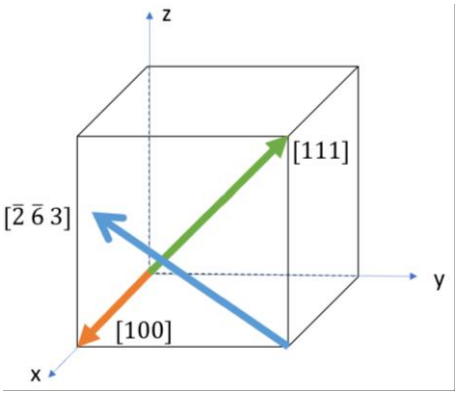

Figure 2.7 Crystallographic direction in a cubic unit cell

$$FCC:\ Length_{[111]} = \sqrt{\left(\sqrt{\left(2R\sqrt{2}\right)^2 + \left(2R\sqrt{2}\right)^2}\right)^2 + (2R\sqrt{2})^2} = 2R\sqrt{6}$$

$$BCC:\ Length_{[111]} = \sqrt{\left(\sqrt{\left(\frac{4R}{\sqrt{3}}\right)^2 + \left(\frac{4R}{\sqrt{3}}\right)^2}\right)^2 + \left(\frac{4R}{\sqrt{3}}\right)^2} = 4R$$

The orientation of crystallographic planes is determined by using the Miller Indices (hkl) in the following way [8]:

$$h = q * \left(\frac{a}{A}\right) \qquad (2.11)$$

$$k = q * \left(\frac{b}{B}\right) \qquad (2.12)$$

$$l = q * \left(\frac{c}{C}\right) \qquad (2.13)$$

Where A, B and C represents the intersection between the crystallographic plane and the axes a, b and c respectively. Parallel planes have the same indices. Figure Figure 2.8 shows two crystallographic planes, (111) and (110).

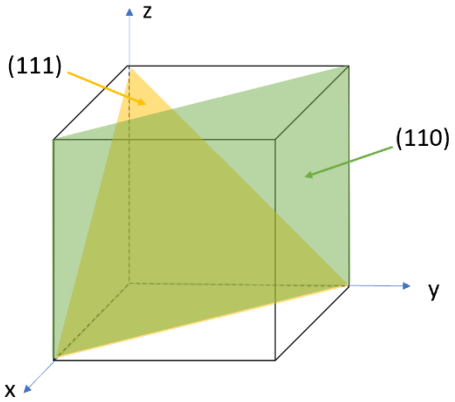

Figure 2.8 Crystallographic planes in a cubic unit cell.

It is often of interest to look at the atomic arrangement for a plane. The atoms laying on the (110) plane on an FCC and BCC unit cell is shown in Figure Figure 2.9.

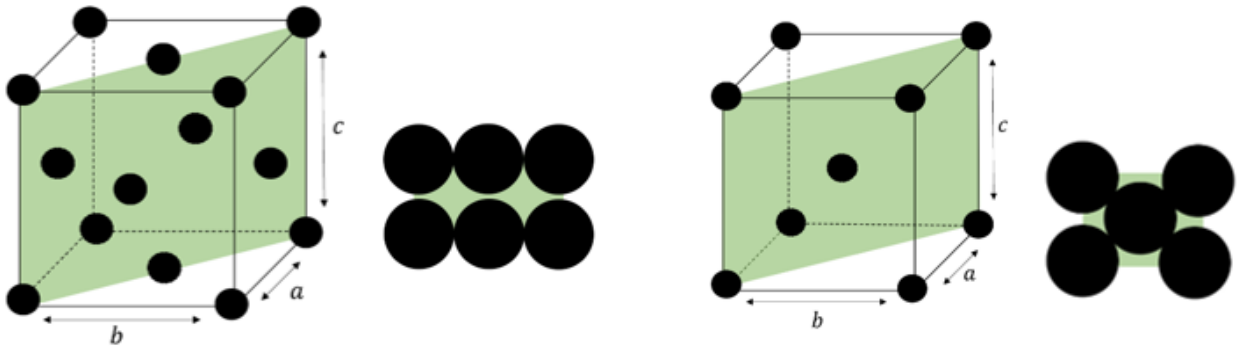

Figure 2.9 (110) plane in the FCC unit cell (left) and BCC unit cell (right)

Linear density (LD) and planar density (PD) are two important properties that are dependent on the crystal structure of a given material. They are especially of great interest when looking at dislocation movement and plastic deformation, which will be discussed in greater depth in chapter 2.2.2. LD describes the

number of atoms that are centered on a crystallographic direction per unit length. PD represents the number of atoms on a crystallographic plane per unit area [8]. This is expressed in the following way:

$$LD = \frac{number\ of\ atoms\ centered\ on\ direction\ vector}{length\ of\ direction\ vector}, unit: nm^{-1}\ or\ m^{-1} \quad (2.14)$$

$$PD = \frac{number\ of\ atoms\ centered\ on\ a\ plane}{area\ of\ plane}, unit: nm^{-2}\ or\ m^{-2} \quad (2.15)$$

The linear density of the [111] direction, shown in Figure Figure 2.7 for FCC and BCC (LD_{111}) in the following way:

$$FCC:\ LD_{[111]} = \frac{1}{2R\sqrt{6}}$$

$$BCC:\ LD_{[111]} = \frac{2}{4R} = \frac{1}{2R}$$

The planar density of the (110) plane shown in figure Figure 2.9 for FCC and BCC crystal structure respectively can be determined in the following way:

$$FCC: PD_{(110)} = \frac{2}{\left(\sqrt{\left(2R\sqrt{2}\right)^2 + \left(2R\sqrt{2}\right)^2}\right) * 2R\sqrt{2}} = \frac{2}{8R^2\sqrt{2}} = \frac{1}{4R^2\sqrt{2}}$$

$$BCC:\ PD_{(110)} = \frac{2}{\left(\sqrt{\left(\frac{4R}{\sqrt{3}}\right)^2 + \left(\frac{4R}{\sqrt{3}}\right)^2}\right) * \frac{4R}{\sqrt{3}}} = \frac{2}{\frac{16\sqrt{2}}{3}R^2} = \frac{3\sqrt{2}}{16R^2} = \frac{3}{8R^2\sqrt{2}}$$

How these properties affect dislocation movement will be explained in the following chapter.

2.2.2 Dislocations

No materials are formed by perfectly arranged microstructure. Within all materials, some type of microstructural defects occurs. Dislocations are a type of linear crystalline defects, where there are misalignments along an axis of atoms in a lattice. One type of dislocation is called edge dislocations. Here, either an extra portion of a crystallographic plane of atoms are placed in the structure, or atoms from a plane are missing. Another type of dislocations are screw dislocations. These dislocations are a result of applied shear stress. This makes the upper front region of the crystal shift one atomic distance to one side relative to the bottom part. Most metallic materials contain both edge and screw dislocations, in other words mixed dislocations [8] [12].

Movement of dislocations is often what creates plastic deformation, also referred to as permanent deformation. Intermetallic bonds between atoms in two adjacent atomic planes break and reforms with other atoms. Dislocation movements typically happens along preferred planes and directions, often called slip

planes and slip direction respectively. The combination of slip plane and direction is known as slip system. Dislocation motion tends to begin along the closest packed crystallographic planes (greater PD) and in the direction within that plane that has the highest LD. As already mentioned earlier in this chapter, FCC has the densest packed crystal structure. The $\{111\}$ family is a set of planes in the FCC crystal structure with the highest PD. The (110) plane illustrated in Figure 2.9 is one of the slip planes in the $\{111\}$ family. <110> is the direction in which slip occurs along within the $\{111\}$ family. The slip system for FCC is therefore $\{111\}$ <110>. There are a total of 12 slip systems for FCC crystal structure [8].

The atomic arrangement in BCC and HCP crystal structure also provides a relatively high number of slip systems compared to other crystalline structures. With BCC, there are three possible slip plane families, which are the $\{110\}$, $\{211\}$ and $\{321\}$ families. The first two slip plane families have 12 slip systems and the $\{321\}$ has a total of 24 slip systems. All the planes have the slip direction <111> [8]. One of the planes from the $\{110\}$ plane family is the (110) plane shown Figure 2.9. There are the same number of slip plane families in HCP as BCC, $\{0001\}$, $\{10\bar{1}0\}$ and $\{10\overline{11}\}$, with <11$\bar{\bar{2}}$0> slip direction. Each of the first two slip planes have three slip systems and the $\{10\overline{11}\}$, has six slip systems.

The relatively high number of slip systems in FCC and BCC, indicated that these structures allow for plastic deformation in a greater extent. Due to this, materials that are built up of FCC and BCC crystals are often quite ductile. Even though HCP also have multiple slip systems, they do not always allow for movement to happen. As a result, there are less active slip systems in HCP. Materials built up of HCP crystal structures are therefore more brittle. Other materials built up of crystal structures with fewer slip systems will also have limited possibilities for plastic deformation. That is common for brittle metals[8].

For most metals, the crystallographic orientation of the grains affects some of the mechanical properties. Materials with preferred crystallographic orientations of the grains are said to have anisotropic properties. Grain boundaries act as barriers for the dislocation motions because two adjacent grains have varying orientation. As a result, the slip plane must change its direction of movement, which results in a discontinuity of the slip plane from one grain into another. A crystalline structured metal that contains many small grains will therefore be more resilient to plastic deformation than a coarse-grained structured metals. The yield strength will for instance be higher for fine grained metals. The Hall-Petch equation (Equation (2.16)) mathematically expresses the yield strength (σ_y) as a property depending on the grain size in the following way [8]:

$$\sigma_y = \sigma_0 + \frac{k_y}{\sqrt{d}} \qquad (2.16)$$

Where $\sigma_0$and k_y are material dependent constant, and d is the average diameter of the grain.

2.3 Aluminum bronze

Aluminum bronze are copper-based alloys containing 4-14wt% aluminum and smaller amount of nickel iron, silicon and manganese The metallic alloy is known for its good mechanical properties, excellent resistance to corrosion and cavitation-erosion, which makers it suitable for the maritime and offshore industry [3]. Properties of alloying elements in aluminum bronze are represented Table 2.1.

Element	**Crystal structure at 20°C**	**Density in the solid state at 20°C (g/cm^3)**	**Atomic weight (amu)**	**Atomic radius (nm)**	**Melting temperature (°C)**
Aluminum (Al)	FCC	2,71	26,98	0,1431	660,4
Nickel (Ni)	FCC	8,9	58,69	0,125	1455
Copper (Cu)	FCC	8,94	63,55	0,128	1085
Iron (Fe)	BCC	7,87	55,85	0,124	1538
Silicon (Si)	Diamond cubic	2,33	28,09	0,118	1410
Manganese (Mn)	Cubic	7,44	54,94	0,112	1244

Table 2.1 Properties of alloying elements in aluminum bronze [8].

Copper is a precious metal that occurs naturally on earth, mostly from ores. It has been known since around 5 000 BC [13]. In the beginning, the metal was mostly used for weapon, tools and jewelry. The field of application expanded drastically with time. It has been used for electrical purpose for many years, however in the beginning of the 20th century is when it was massively used in modern electricity industry. Today, copper is used in multiple other industries as well [14].

Copper is usually manufactured as an alloy. Three main copper-based alloys are bronzes, brasses, and higher copper alloys. Aluminum bronze is a part of the bronze-family. Its mechanical properties heavily rely on the lattice structure, just like with any other metals. Copper, which has an FCC crystal structure, has good toughness, ductility, and formability properties. Other beneficial properties are the excellent resistance to corrosion, and electrical and thermal conductivity [14] [15].

Aluminum, which is the third most abundant element on earth, is a light base metal. However, due to the oxide films that covers the surface of the metal during oxidizing, aluminum is a relatively stable and protected from corrosion [12]. It has an FCC crystal structure and is the alloying element in aluminum bronze that contributes the most to resistance to corrosion [3]. Further, aluminum is highly formable. For many applications, aluminum is not strong enough. However, as an alloy, this mechanical property can be improved [16].

Addition of iron in the alloy enhances its toughness and strength, as well as its hardness and fatigue resistance. It also improves wear and corrosion resistance. Iron has a low solubility in aluminum bronze at room temperature. With certain heat treatments, the alloy may form iron-rich κ precipitates.

2.4 Phases and phase diagram of aluminum bronze

A phase refers to a homogeneous part of a system with uniform chemical and physical characteristics [8]. Most metallic construction materials are heterogeneous, which means that they consist of two or more phases. The number of phases, their sizes and crystallographic orientation within a metallic microstructure affects the mechanical properties of the material. The alloying elements and their concentrations, the heat treatment applied, and external pressure are factors that determines the present phases. Phase diagram is a tool used to show the phases that occurs within a material at given temperature, composition, and pressure at equilibrium.

The binary copper-aluminum phase diagram at the copper-rich end is shown in Figure 2.10. In the binary system, only copper and aluminum are the present elements. The phase diagram of CuAlFe5Ni5, which is an aluminum bronze alloy containing 10wt% aluminum and 5wt% iron and nickel each, is also shown in Figure 2.10 at the copper-rich end.

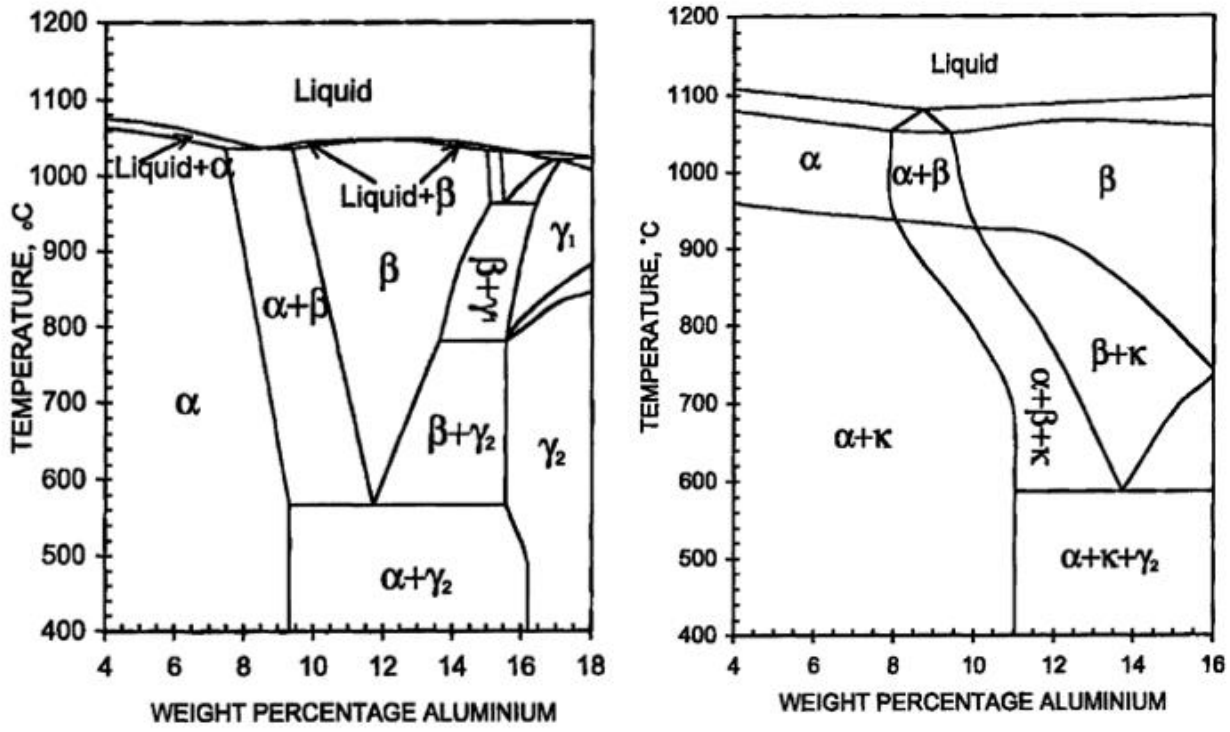

Figure 2.10 CuAl phase diagram at the copper-rich end (left), and CuAlFe5Ni5 phase diagram at the copper-rich end (right) [3].

2.4.1 Alpha (α) phase

In the CuAl binary phase diagram shown in Figure 2.10 one can observe that a copper-alloy containing up to approximately 9wt% aluminum will solidify as a single α phase. The same single phase appears in a CuAlFe5Ni5 alloy containing up to approximately 8wt% aluminum, however, only at higher temperatures. The α phase is a copper-rich solid solution with FCC crystal structure that provides ductility to the alloy [17]. It appears as light etched areas when observed in microscopes.

2.4.2 Betha (β) phase

β phase is an intermediate phase or solid solution, which forms at elevated temperatures when the aluminum content is above approximately 8wt%. An intermediate phase is a phase that is found in between the two composition extremes [8]. This phase has a BCC crystal structure and is stronger and harder than the α phase, but less corrosion resistant [17].

There is a eutectic point in the binary CuAl phase diagram at approximately 9wt% aluminum and temperature of 1050˚C. Here, the liquid transforms isothermally and reversibly into a two-phase solid region, $\alpha + \beta$, with approximately 8wt% and 10,5wt% aluminum respectively. This can be expressed in the form of eutectic reaction in the following way:

$$L(9wt\%\ al) \leftrightarrow \alpha(8\ wt\%\ al) + \beta(10{,}5\ wt\%\ al)$$

If the alloy contains around 10 to 15wt% aluminum at an elevated temperature, the metal solidifies in the single β phase.

2.4.3 Retained betha (β') phase

Retained betha phase, also called β' or martensitic betha phase, appears when β phase is rapidly cooled or quenched to room temperature [3]. It has a martensitic microstructure, which has needle-shaped grains, and HCP crystal structure. This phase strengthens the material.

2.4.4 Gamma 2 (γ_2) phase

γ_2 is another intermediate phase. It is strong, but less corrosion resistant and less ductile [17]. In CuAlFe5Ni5, this phase appears at lower temperatures in a three-phase region together with α and κ phase. The wt% aluminum is above approximately 11wt%.

2.4.4 Kappa (κ) phase and precipitates

κ phases or particles are intermetallic phases or compounds. They are either based on Fe_3Al, NiAl or FeAl. The particles forming the κ phase are small precipitates. These precipitates are beneficial and desirable to exist in the microstructure because they give strength and hardness to the material. Therefore, precipitation hardening, and age hardening are techniques often used on metals and metal alloys [17].

2.5 Precipitation hardening

Precipitation hardening, illustrated in Figure 2.11, can be seen at as a two-step heating process: solution heat treatment and precipitation heat treatment. During the solution heat treatment, the temperature is kept relatively high. All the elements within the alloy dissolves to form one single phase solid solution. Further, the alloy is immediately quenched, often to room temperature. This process is done so rapidly that there is no time for diffusion to occur. No diffusion means that there is no movement of the atoms, ions, or molecules within the material. As a result, only the same single phase solid solution will exist in a nonequilibrium state. This state is characterized as being relatively soft and weak [18].

During the precipitation heat treatment, single phase solid solution is heated to an intermediate temperature for a certain amount of time. Diffusion will occur, and second phase precipitates based on a combination of elements will appear. This process is called aging. The precipitates will hinder dislocation movement and strengthen the material. The alloy is then cooled again to room temperature. The aging time and temperature will affect the formation of the precipitates and consequently some of the material's mechanical properties [8].

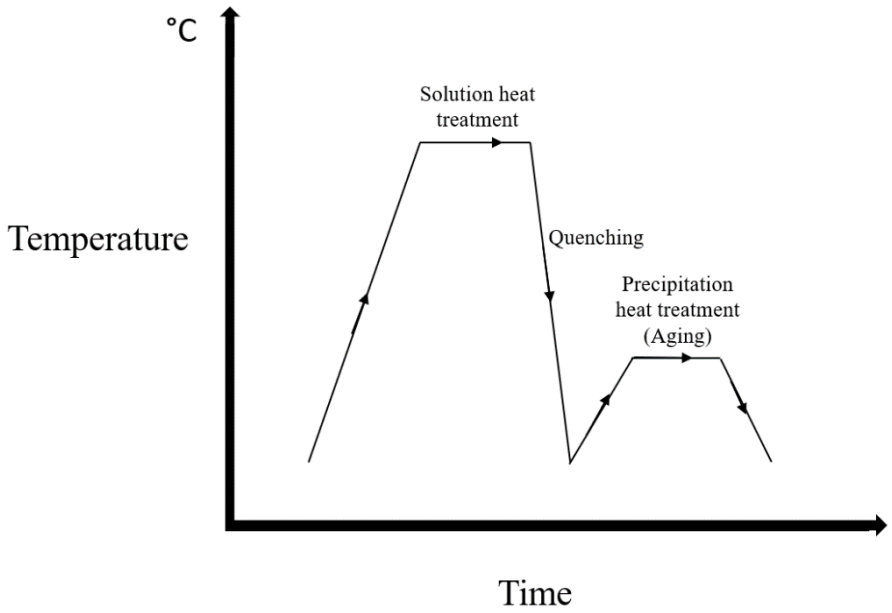

Figure 2.11 Precipitation hardnening diagram.

2.6 Heat affected zone

Heat affected zones (HAZ) are solid areas in the material adjacent to the melting pool that experiences changes in its mechanical and microstructural properties [19]. This is due to the elevated temperature that the HAZ are exposed to. This phenomenon is mostly known from welding, but also happens during 3D-printing and other operations.

The size of HAZ varies with the properties of the material and parameters of the heating source [19]. Thermal diffusivity, D_T, is a material-specific property that describes the rate of heat transfer in a material from a hot to a cold side. Thermal diffusivity is mathematically expressed in the following way [8]:

$$D_T = \frac{k}{\rho c_p} \tag{2.17}$$

Where k is the thermal conductivity, ρ the mass density, and c_p the specific heat at constant pressure.

A metal with a higher level of thermal diffusivity, usually has HAZ with smaller width, compared to metals with lower level of thermal diffusivity [19]. This is because higher thermal diffusivity levels means that the material is able to transfer the heat variation at a faster rate, which results in the material cooling quicker. As already mentioned, the width of the HAZ also depends on the heating source. The amount of heat applied, the concentration of the heating source and the duration of heating are parameters that will affect the size of the HAZ. Generally, a material that is exposed to heat for a longer period of time will have larger HAZ. Also being exposed to a heating source with higher heat input will result in greater HAZ, because the cooling rate will be slower than if the heat input was lower. Additionally, lowering the DED speed will increase the HAZ size.

2.7 Planar, cellular, and dendritic growth

Microstructures of metals usually contains planar, cellular, or dendritic structures [4]. They form during the solidification process in the solid-liquid interface after the formation of nuclei and affects the mechanical properties of the material. For pure metals, planar structure normally appears, while any of the three above-mentioned microstructures can appear in metal alloys, depending on the present elements and solidification process. For planar growth to happen and to be stable during solidification, the following criteria must be met, assuming steady state conditions:

$$\frac{G}{R} \geq \frac{\Delta T}{D_L} \tag{2.18}$$

Where G is temperature gradient, which measures the rate of temperature change at a specific direction [20], R is the growth rate, $\Delta T = T_L - T_S$ is freezing range (the temperature difference between the temperature at the liquidus line (T_L) and solidus line (T_S) in the phase diagram at a given composition), and D_L is the diffusion coefficient.

During the solidification process, when the liquid ahead of the solid-liquid interface has a positive temperature gradient, the heat is released through the growing solid. The temperature gradient is linear and evenly perpendicular to the interface, which results in the solid growing planarly into the liquid.

If the liquid has a negative temperature gradient, which means that the temperature decreases ahead of the solid-liquid interface in what is called undercooling, growth of either cellular or dendritic structure will occur. The formation of cellular structure is a result of small undercooling (high G and low R), while dendrites grow when larger undercooling occurs (low G and high R) [1]. Figure Figure 2.12 shows how the temperature gradient (G), growth rate (R) and alloying level affects the substructure during solidification.

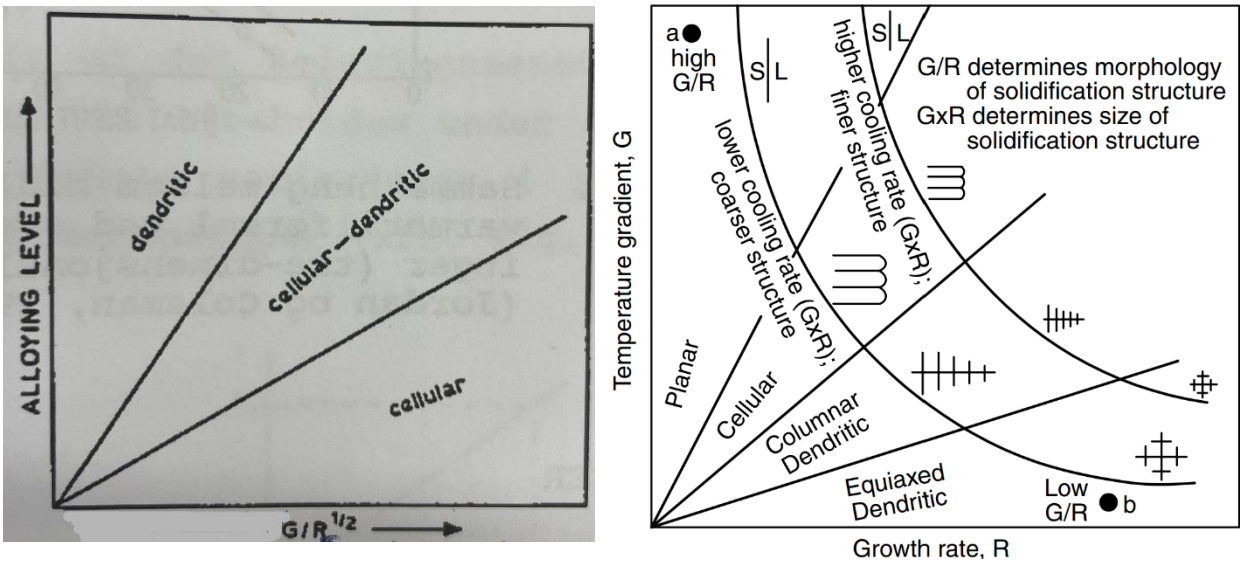

Figure 2.12 Parameters that affects the occurring substructures during solidification. Left: Alloying level as a function of (G/R)^-1/2 [1]. Right: G as a function of R [4].

Dendrites are three-lookalike structure that consists of a primary arm with secondary and sometimes tertiary arms that grows along preferable directions as a result of constitutional undercooling. The distance between the secondary arms, known as the secondary dendrite arm spacing (SDAS), is an important microstructural feature for materials with dendritic structures. SDAS is proportional to the local cooling rate (°C/s). Higher local cooling rate, which means shorter solidification time, results in smaller dendritic arm spacings and finer dendritic or cellular structures [4]. Research shows that decreasing SDAS increases strength and hardness, reduce interdendritic shrinkage porosity, and influences thermal and electrical conductivity [21].

Different measuring methods for determining the SDAS exists. The linear intercept method is one of them, where an optical microscope and an image-analyzing software is used to calculate the SDAS. A straight line parallel to the primary dendrite arm is drawn, and the number of secondary arms intersecting this line is

counted. In practice, this manual technique is somewhat unprecise, resulting in different results occurs between investigators. However, how much the variation affects the measurements is unclear [21]. Regardless, it is important to be consistent and accurate when using this method. Good specimen preparation is important to properly examine the dendrites.

2.8 Mechanical tests

2.8.1 Charpy test

Charpy is a standardized mechanical test used to measure fracture toughness for structural materials [8]. A test specimen has a standardized bar-shape with a square cross section and has a V- or U-notch machined into it. The specimen is placed in the bottom of the testing apparatus. A weighted pendulum hammer is released from a given height and corresponding initial potential energy. A knife edge mounted on the pendulum strikes the specimen on the opposite side of the notch, which fractures the specimen. The new height that the pendulum reaches is related to the energy absorbed by fracturing the specimen. The energy required to fracture the specimen is equal to the change of potential energy oof the pendulum hammer in the following way:

$$\Delta E_p = m * g * \left(h_i - h_f\right) \ , unit: J \qquad (2.19)$$

Where h_i and h_f are the initial and final height of the pendulum hammer.

The amount of energy absorbed by the specimen depends on the toughness of the material. As mentioned in the previous chapter, a ductile material requires higher amount of energy to be fractured, while brittle materi al absorb less energy before fracture occurs. In this way, one can carry out a Charpy test to determine whether a material has brittle or ductile features. By studying the fractured surfaces afterwards, toughness properties can also be examined.

2.8.2 Tensile test

Tensile test is a common stress-strain test done to determine the characteristics of a material when subjected to forces or load. Different mechanical properties can be addressed in a tensile test that are important in design. The principle of the tensile tests is to strain a test piece to fracture by applying a uniaxial tensile force along the long axis of the specimen. The shape of the specimen varies with standards and the given material. The test specimen has a circular or rectangular cross section that is uniform along the length. The end parts of the specimen are mounted into the holding grips of the tensile testing machine. When the force is applied by the machine at a programmed rate, the specimen gets elongated at a constant rate until fraction. During this process, the instantaneous applied load and the resulting elongations are measured. An extensometer is used to measure the elongation. A load cell is used to measure the applied tension.

The output data of a tensile test is usually recorded on a software on a computer that is connected to the tensile testing machine. It is represented by a stress-strain curve, where the vertical axis represents the applied force as stress, while strain is plotted along the horizontal axis, which is related to the elongation of the specimen. Figure Figure 2.13 shows a typical stress-strain curve for a brittle and ductile material. The elongation is a function of the tensile force. To minimize the effects of geometrical factors on the output data, one uses engineering stress (σ) and engineering strain (ϵ) as parameters. These parameters are often referred to as just stress and strain respectively. The definition of engineering stress for tension and compression is as following [8]:

$$\sigma = \frac{F}{A_0} \ , unit: MPa \qquad (2.20)$$

Where F is the force applied perpendicular to the cross section of the specimen, and A_0 is the initial cross-sectional area.

The engineering strain is defined in the following way:

$$\epsilon = \frac{l_i - l_0}{l_0} = \frac{\Delta l}{l_0} \qquad (2.21)$$

Where l_i is the instantaneous length and l_0 is the initial length. This property is unitless and normally expressed in percent.

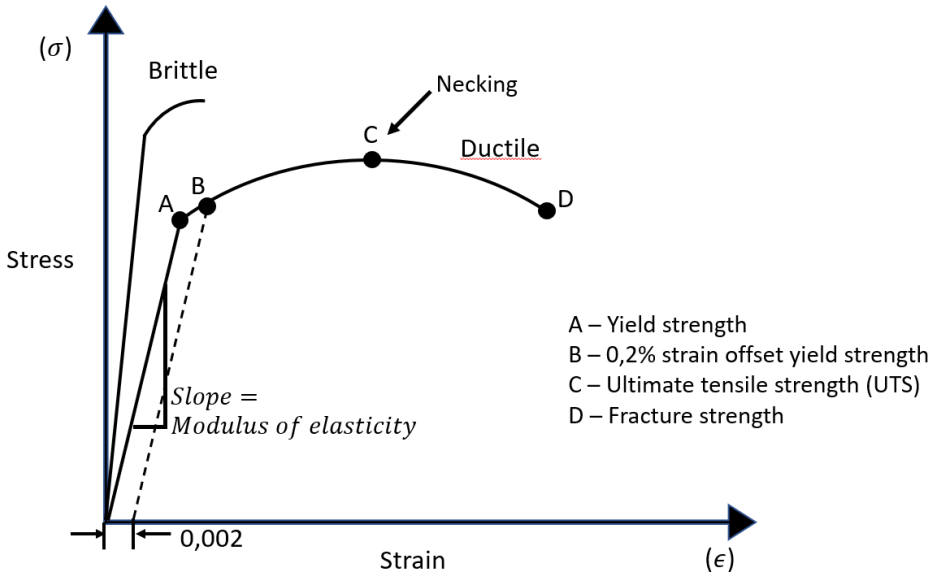

Figure 2.13 Stress-strain curve for a brittle and ductile material.

Looking at the stress-strain curve for the ductile material, the linear part of the curve represents the elastic deformation that the material undergoes. If the applied load is removed, the specimen returns to its original

shape. In this situation the relationship between stress and strain are represented by Hooks law in the following way:

$$\sigma = E * \varepsilon \, , unit: MPa \qquad (2.22)$$

The modulus of elasticity (E-module) corresponds to the slope of the linear part of the stress-strain curve. One can think of the modulus as stiffness or a materials resistance to elastic deformation [8]. Greater modulus of elasticity is typical for brittle materials and indicates higher stiffness. The elastic strain resulting from the applied stress is smaller.

The yield strength (σ_y) represents the limit at which the material can be deformed elastically, and is noted A in Figure 2.13. It is important to pay attention to this mechanical property because most structures are designed in a way that only allows for elastic deformation when exposed to stress. It is expressed in the following way:

$$\sigma_y = \frac{F}{A_0} \, , unit: MPa \qquad (2.23)$$

Where A_0 is the initial cross-sectional area.

The border between the elastic and plastic deformation can be difficult to determine for some materials. Therefore, a convention has been established by which a linear line is drawn parallel to the linear line of the stress-strain curve at a strain offset usually of 0,2%.

Other materials have a clear transition between the elastic and plastic region in the stress-strain curve in what is called a yield point phenomenon. Plastic deformation starts at the upper yield point at a given stress value. The stress decreases quickly and then fluctuates somewhat about a given stress value, called the lower yield point. For materials whit such behavior the yield strength is determined by the average stress at the lower yield stress.

When the material is deformed further beyond the yield strength, permanent or plastic deformation occurs. If the applied force gets removed, the material will not go back to its original shape. For crystalline materials, plastic deformation usually starts with the motion of dislocations as mentioned in Chapter 2.2.2. Point C in Figure 2.13 represents the tensile strength. This is the maximum stress the material in tension is exposed to. Up to this point in the plastic region, all deformation in the specimen has happened uniformly throughout the measuring region. From this point, the necking phenomenon begins, where all deformation continuous at this neck until it fractures at the end point of the stress-strain curve. The stress at the point of fracture, point D, corresponds to the fracture strength.

2.8.3 Vickers hardness test

Hardness of a material is a mechanical property that describes the materials resistance to local plastic deformation [8]. The surface of the testing material is subjected to a small indentation at a given force and under specific conditions. The size of the resulting indentation is measured, which corresponds to a hardness value. Hardness tests are easy and inexpensive to perform compared to other mechanical tests. They also have the great benefit of not destructing the specimen to fracture or heavily deformation.

Vickers hardness test is a hardness test method where a small pyramidal-shaped diamond penetrates the surface of the material. Figure 2.14 provides an illustration of the test. The depth and size of the resulting indentation is measured and determined by using a microscope. For the investigation to be done successfully, careful surface preparation may be necessary. The measured values are then converted into Vickers hardness values (HV). The formula for Vickers hardness value is as following [8]:

$$HV = 1{,}854 * \frac{P}{d_1^2} \qquad (2.24)$$

Where P is the applied load in kg and d_1 is the length of the square-shaped indentation´s diagonal. HV values less than 120-150 is considered soft and/or ductile [22].

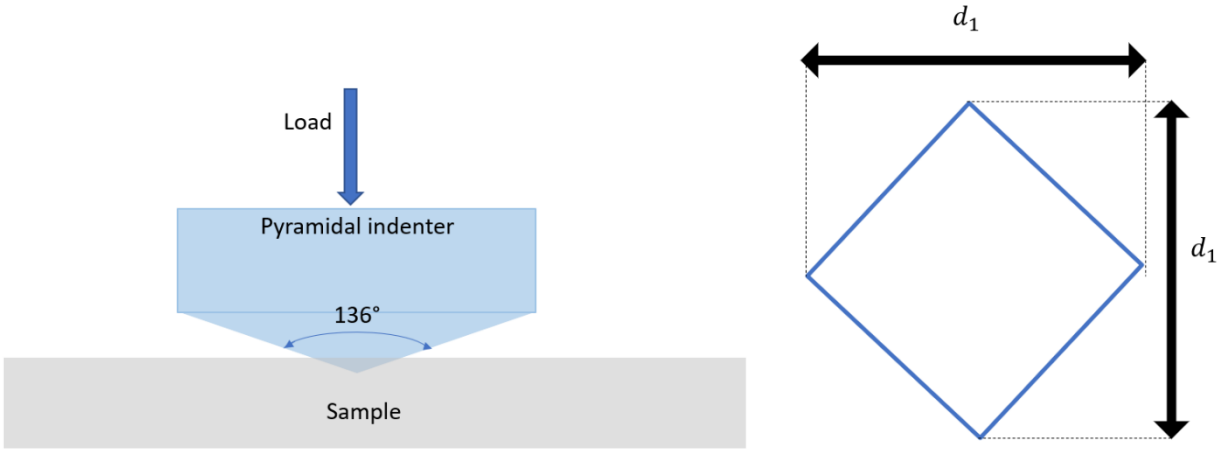

Figure 2.14 Schematic illustration of Vickers hardness test. A pyramidal indenter penetrates the surface of a sample with a given load (left). The diagonals of the resulting indent is measured with the optical.

2.9 Fracture

Uniaxial tensile fracture for ductile materials is characterized by extensive plastic deformation after necking. Figure 2.15 illustrates a ductile tensile fracture.

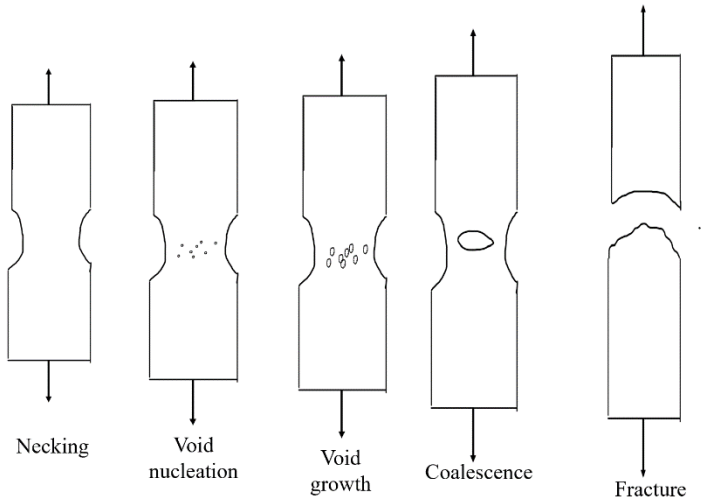

Figure 2.15 Uniaxial tensile fracture for ductile materials.

During necking, three-dimensional stress state is generated in the middle of the specimen. This causes the nucleation and growth of microvoids, particularly in the larger particles. The isotropic stress is greater in the center of the specimen than in the outer region. As a result, more microvoids are formed in the center region. When subjected to further strain, the voids eventually coalesce, which results in the formation of elliptical cracks in the center region. They are elongated perpendicular to the direction of the applied stress. Deformation bands at 45 degrees from the direction of applied force are formed, as shown in Figure 2.16. The deformation band causes concentrated strain and further formation of voids, which causes instability and eventually cup-and-cone shaped shear fracture. The inner region of the fractured surfaces are fibrous surface that is strongly deformed and elongated [23].

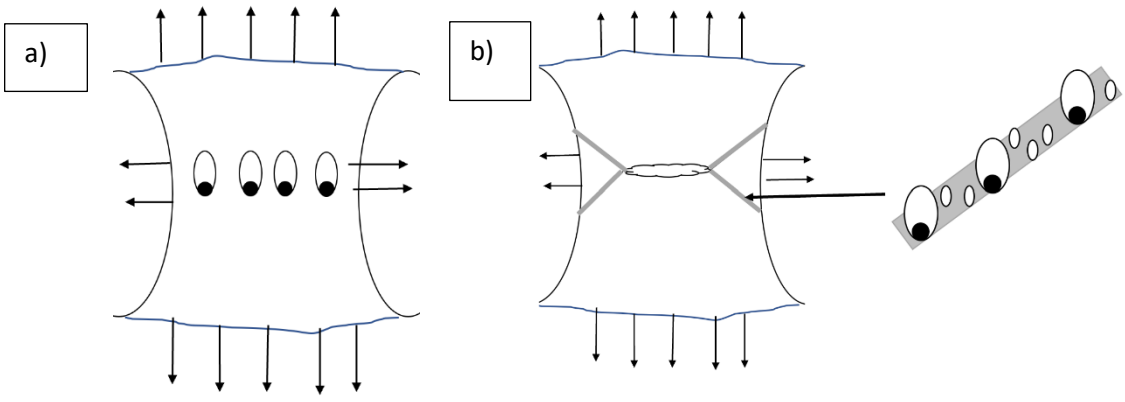

Figure 2.16) growth of microvoids in larger particles creates b) elliptical crack and deformation bands with further formation of microvoids.

Cracks that form in ductile materials during tensile test are referred to as stable cracks. Due to ductile materials ability to form plastically, the resulting cracks propagate relatively slow and are often elongated. These types of cracks are referred to as stable cracks, and are resistant to further expansion, unless the applied stress increases. Brittle cracks are said to be unstable. They tend to propagate quickly spontaneously, also at constant applied stress [8].

2.9 Microscopic analysis

2.9.1 Optical microscope

Optical microscopy, commonly known as light microscopy, is the most familiar microscope in metallography. uses visible light to examine the microstructure. When the light hits the surface of the material, the different regions of the surface will reflect the light differently. The reflected light then passes through the objective lens, which magnifies the image. The difference in reflection is what creates contrasts in the image that is generated. The maximum possible magnification is approximately 2000 times for an optical microscope, which makes it possible to review microstructures at 0,2µm [8].

It is usually necessary to do surface treatment on the specimen to examine important details of the microstructure. Normally, the surface gets smoothened by grounding and polishing, using abrasive paper and powder. Etching is also used as a surface preparation technique. Different grain structures and crystallographic orientations have different etching characteristics. The reflection of the light on the surface of the specimen will differ as a result of the different grain structure. This will create the contrasts in the images generated from an optical microscope.

2.9.2 Electron microscope

With electron microscopy (EM), beams of accelerated electrons are used instead of visible light radiation to generate microstructural images. It is possible to examine finer and smaller structural elements with EM than with an optical microscope because of the possibility of generating images with higher magnification. This is due to the electrons having shorter wavelength. Scanning electron microscopy (SEM) and Transmission electron microscopy (TEM) are two types of EM [8].

2.9.2.1 Scanning electron microscope

Scanning electron microscope (SEM) is used to analyze the surface and near surface areas of a sample. A focused beam of electrons is released towards a sample from an electron gun. The electrons accelerate to an energy between 1keV and 30keV [24]. The main components of SEM are the following:

- Electron gun
- Set of electron lenses (first condenser lens, second condenser lens and final (objective) lens
- Detectors for all signals of interest

- Connected computer and software for data output analysis

When the electrons hit the surface of a specimen, they will diffract simultaneously. The electrons that are reflected, also called backscattered, creates different types of signals, including secondary electrons, backscattered electrons (BSE), diffracted backscattered electrons (EBSD), photons, visible light, and heat. The different signals reveal information regarding morphology, chemical composition, phases, and crystalline structure and orientation. The secondary electrons that generate SEM-images can be magnified ranging from 10 to 50 000 times and provides very good depths of field. Photons generates X-rays, which is used for elemental analysis. Energy-dispersive spectroscopy (EDS) is used for chemical analysis. The specimen under SEM investigation must be electrically conductive [8] [25].

2.9.2.3 Electron backscattered diffraction

Electron backscattered diffraction (EBSD) is a technique used in SEM. It provides microstructural information regarding crystallographic orientation at specific locations, present phases, grains, texture and more. Crystallographic texture is the distribution of crystallographic orientations in a polycrystalline sample, which affects mechanical properties of the given material. The sample is tilted to a 70^{o} angle. The diffraction pattern consists of lines that are generated on a transmission phosphor screen. On the other side of the phosphor screen, a sensitive CCD camera records the pattern. The diffraction pattern is then sent to the computer where it gets analyzed. The assumed crystal structure of the sample gets compared to the positioning of the diffraction lines and the angle between them. The program calculates the crystallographic orientation and stores the pattern [24].

3. Experimentation

3.1 Aluminum bronze delivered by Nordic Additive Manufacturing

The chemical composition of the aluminum bronze delivered by Nordic Additive Manufacturing (NAM) is given in Table 3.1. Figure 3.1 shows the metal block as it was received from NAM. The block had the following dimensions: (101x63x30)mm (height x width x thickness). The metal has been printed using a DED method. It has been deposited in the xy-plane with a laser power of 1000W and at a speed of 1000mm/min. Figure 3.2 illustrates how the layers have been laid. No heat treatment had been done on the material.

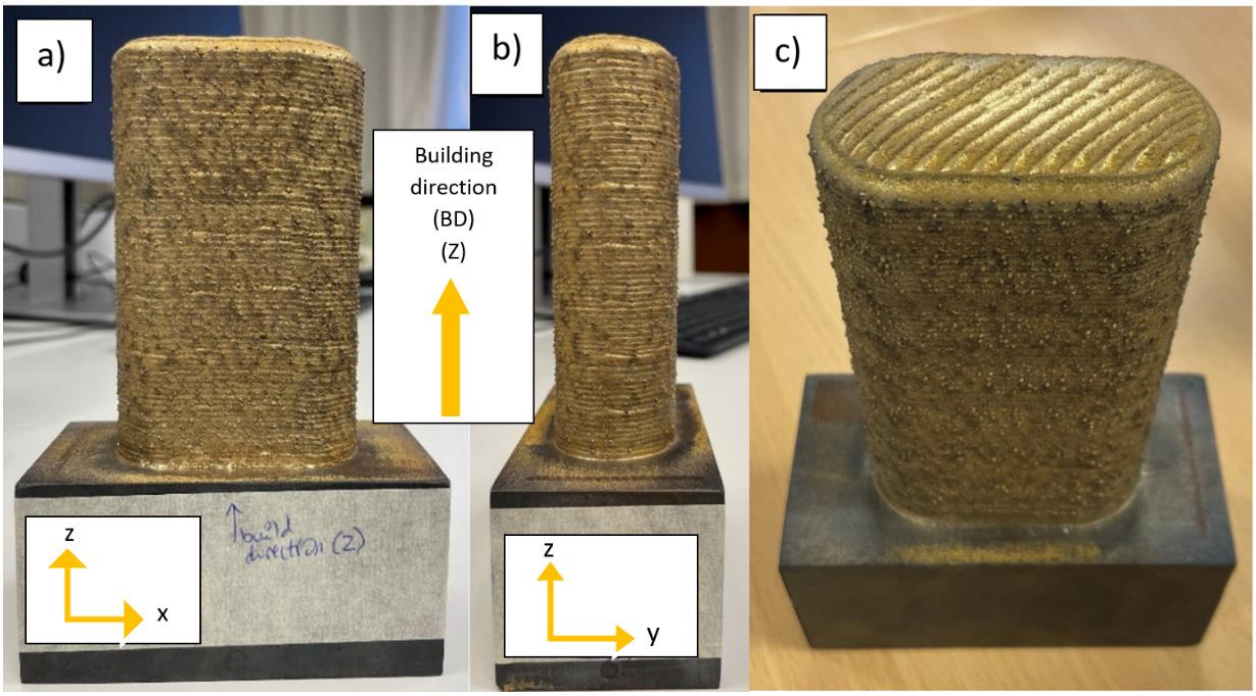

Figure 3.1 Photograph of the aluminum bronze block delivered by NAM. a) zx-plane, b) zy-plane and c) Perspective view. From this view, one can observe that the top layer has been deposited 45 degrees on the y-axis.

Chemical composition	**Value**	**Unit**
Al	9,42	WT%
Ni	0,005	WT%
Cu	89,38	WT%
Fe	1,10	WT%
T.A.O	<0,10	WT%
O	0,041	WT%

Table 3.1 Chemical composition of the aluminum bronze delivered by NAM.

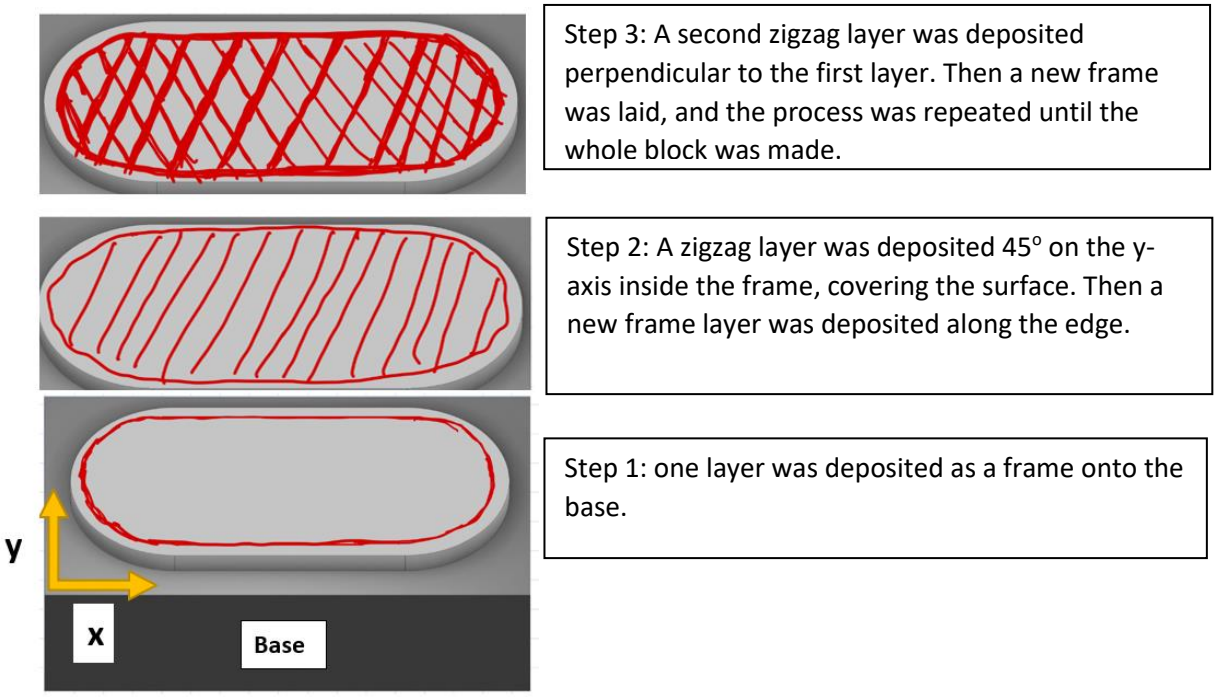

Figure 3.2 Illustration of the deposition method used for the 3D-printing of the aluminum bronze. A laser power of 1000W and 10mm/min printing speed.

3.2 Charpy V test and tensile test

From the metal block, three test specimens were sectioned for Charpy V test (CVT) and three for tensile test (TT). Figure 3. shows where the test specimens were located originally in the metal block.

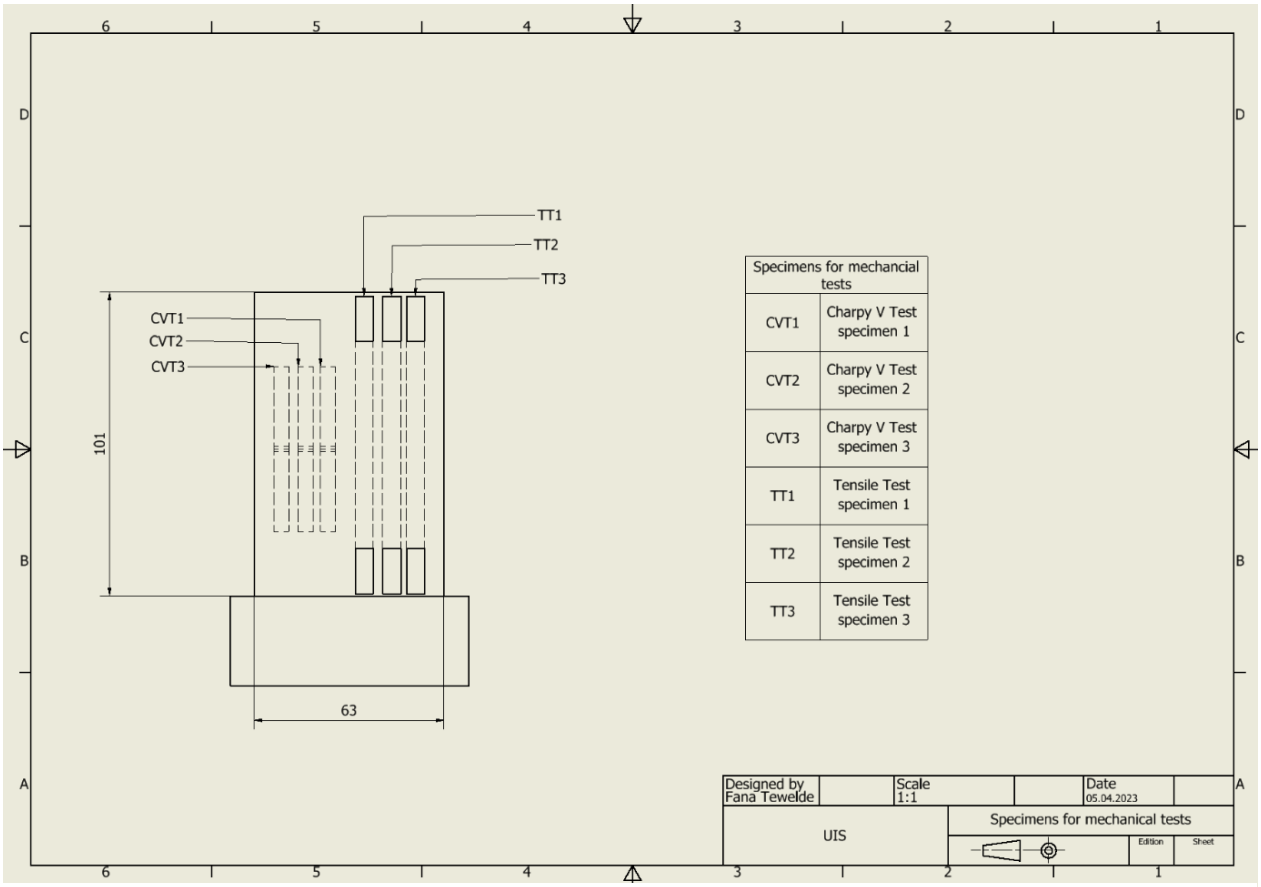

Figure 3.3 Drawing of test specimen for Charpy V test (CVT) and tensile test (TT) from the original metal block. Measured in mm.

3.2.1 Charpy V test specimen sectioning and preparation

The Charpy V test carried out in this work was done according to NS-EN ISO 148-1:2016 [2]. The dimensions for the three test specimens CVT1, CVT2 and CVT3 are represented in Figure 3.3 and Table 3.2. To ensure that sufficient material remained for other tests and inspections, subsize test piece with 5mm thickness was used instead of standard test piece with 10mm thickness.

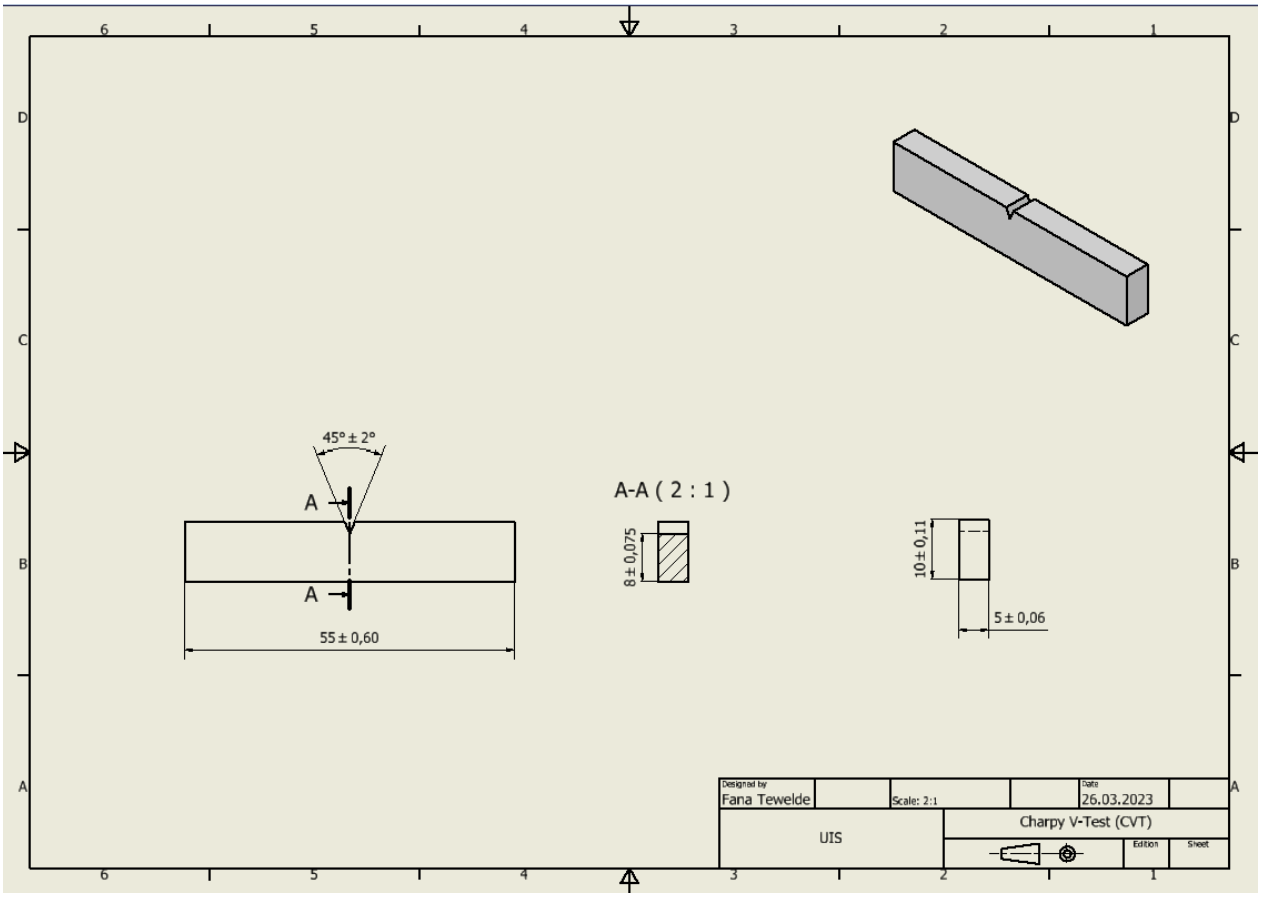

Figure 3.3 Drawing of Charpy V test specimen (CVT1, CVT2 and CVT3) and its dimensions in mm, according to NS-EN ISO 148-1:2016 [2]. Made in Autodesk inventor.

Designation	Unit	Value	Machining tolerance
thickness of test piece	mm	5	± 0,06
width of test piece	mm	10	± 0,11
length of test piece	mm	55	± 0,60
angle of notch	°	45	± 2

Table 3.2 Test specimen dimensions for CVT1, CVT2 and CVT3.

First, the metal block was cut in the Struers Discotom 10, which is an abrasive wet cutting machine, shown in Figure 3.4a). This cutting machine had a two mm cut off for each cut. The base that the metal was printed onto was initially cut off. Then, three specimens with thickness of 5 mm ± 0,06mm were cut. The automatic multicut method was used. Silicon carbide (SiC) 10S25 cutting wheel was used, as recommended by Struers for the given material [26] [27]. The lowest possible feed speed of 0,05mm/s was used to minimize the risk of an incorrect cutting path. It was also important that there was enough cooling liquid during cutting to prevent excessive heating that could affect the material and the results.

To get the desired length and width of 55mm ± 0,60mm and 10 ± 0,11mm respectively, the three test specimens where cut using the Mazak Vertical Smart 430A CNC milling machine, which is shown in Figure 3.4b). Finally, the V-notch was made by using the V-notch broaching machine, shown in in Figure 3.4c). The three test specimens, CVT1, CVT2 and CVT3 were now ready for testing.

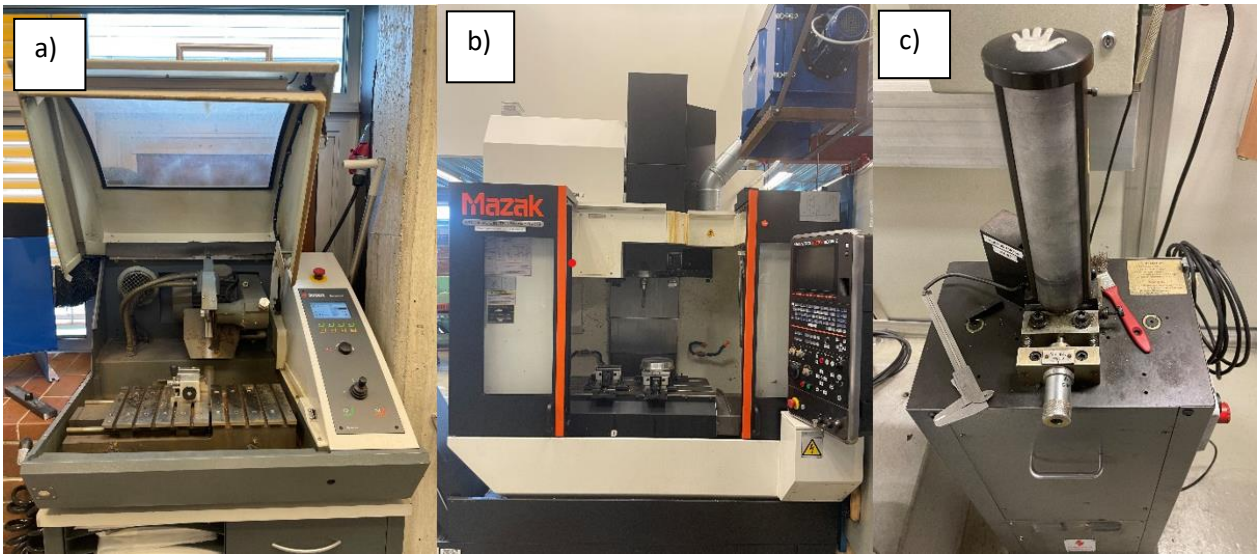

Figure 3.4 The three machines used for sectioning and preparation for the Charpy V test specimens. a) Struers Discotom 10, b) Mazak Vertical Smart 430A CNC milling machine and c) V-notch broaching machine.

3.2.2 Charpy V test

The Charpy V tests were carried out on the Zwick/Roell RKP450, shown in Figure 3.5 b), at room temperature. The testing machine had both a digital and analogue measurement installed to measure the absorbed energy. To make sure that the test piece was properly positioned in the machine, and for safety reasons, self-centering tongs were used, which is shown in Figure 3.5 a). The initial potential energy of the hammer was 450J. After performing the test, the absorbed energy was noted from the digital measuring device. The fractured surfaces were then studied by the naked eye and in SEM. It was important that the

fractured samples were stored separately to minimize the risk of damaging the fractured surfaces before the SEM examination.

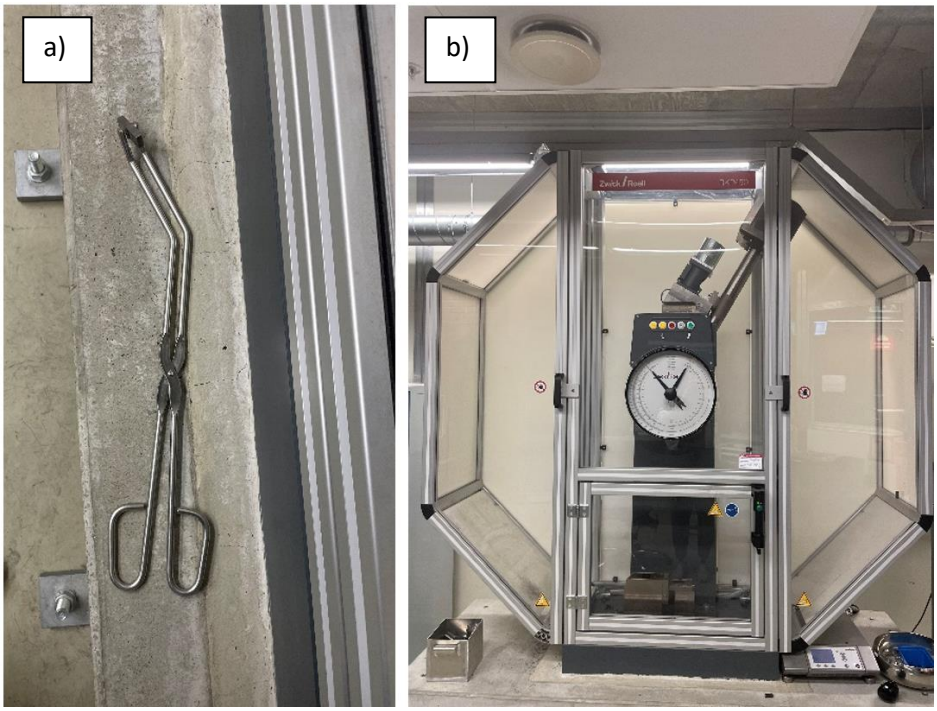

Figure 3.5 a) Self-centering tongs used to place the test specimens in the testing machine and b) Zwick/Roell RKP450 testing machine.

3.2.3 Tensile test specimen sectioning and preparation

The tensile tests carried out in this study was done partially according to NS-EN ISO 6892-1:2019 [28], but not entirely, due to the limitations regarding available material. It was therefore not possible to follow the standard's requirement regarding specimen sizes. The clip-on extensometer, which had a fixed length of 50mm, was used. Using this extensometer would ensure more trustworthy and representative results regarding the modulus of elasticity than other available extensometers in the lab. Consequently, the original gauge length (L_0) of the test specimens had to be at least 50 mm.

It was decided to make test specimens with rectangular cross-sections. Regarding the relations between the cross-sectional area (S_0) and the gauge length (L_0) of the test specimens, the following was followed, according to NS-EN ISO 6892-1:2019 [28]:

$$L_0 = k * \sqrt{S_0} \qquad (3.1)$$

Where $k = 5{,}65$ is the coefficient of proportionality. L_0 is the length of the parallel portion of the test piece on which elongation is measured. The maximum possible length of the tensile test specimens was dependent on the height of the metal block, which was approximately 99mm after the base was cut off. To determine

a suitable gauge length, taking into consideration the above-mentioned requirements and limitations, several drafts had to be designed in CAD and evaluated. Prior to finalizing the specimen dimensions, 3D-printed paper specimen copies were made and evaluated to ensure that the shape would fit nicely in the testing machine. The three specimens were then machined with the dimensions given in Figure 3.6 and Table 3.3. The specimens were called TT1, TT2 and TT3 (TT as in tensile test).

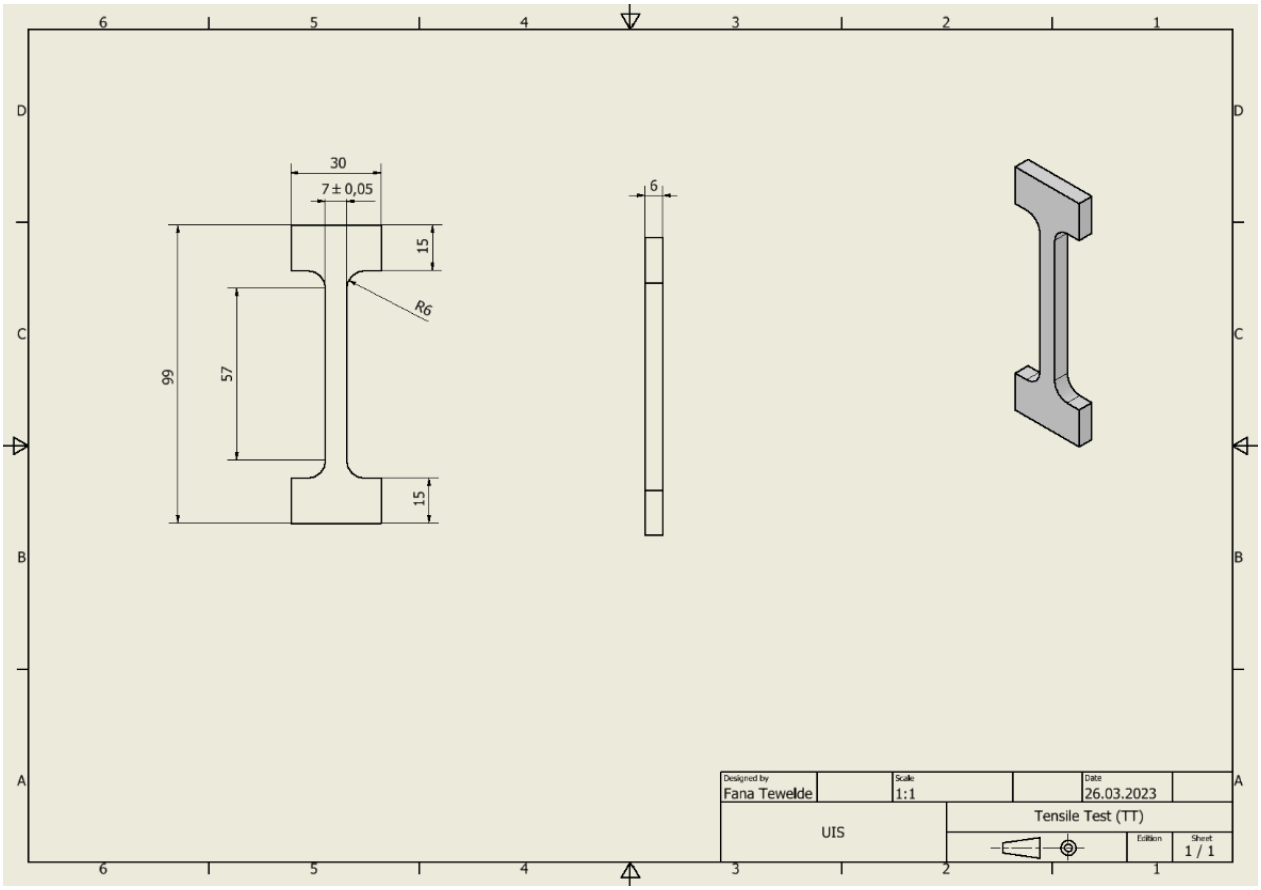

Figure 3.6 Drawing of tensile test specimen (TT1, TT2 and TT3) and its dimensions in mm. Made in Autodesk inventor.

Symbol	Unit	Designation	Value
L_t	mm	total length	99
L_c	mm	parallell length	57
L_0	mm	original gauge length	50
b_0	mm	original width of the parallel length	7±0,05
a_0	mm	original thickness	6
S_0	mm	original cross-sectional area of the parallel length	42
Radius	°	radius between the constricted area and the ends	6
B_0	mm	original width of the ends	30

Table 3.3 Tensile test specimen (TT1, TT2 and TT3) dimensions.

TT1, TT2 and TT3 were cut from the metal block on the Struers Disctom 10 to get the desired thickness. The same cutting method was used here as for the Charpy V test specimens. The Mazak Vertical Smart 430A CNC milling machine was used to get the right shape for the parallel length. The ends of the specimens, as shown in Figure 3.7 were slightly too wide for the grips to grip symmetric on the ends (the grips did not grip on the entire surface of the ends). It was crucial that the grips were gripping symmetrical about the long-axis of the specimen, as noted in the standard [28]. If this was not done successfully, the applied load would not pull axially, which could lead to the specimens bending and result in incorrect result. One of the sides on both ends were machined down so that the grips would pull evenly during the test. Figure 3.8 shows the bottom part of the specimens after removing some material from the right side of the ends.

Figure 3.7 The three tensile test specimens TT1, TT2 and TT3 before removing material from one side of each end.

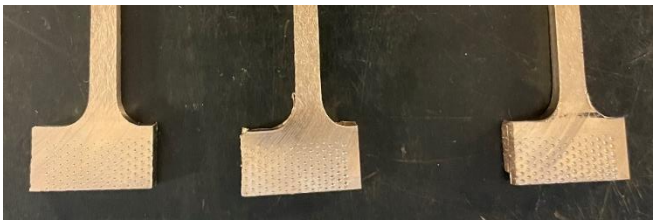

Figure 3.8 The bottom part of the three test specimens TT1, TT2 and TT3 after removing material from the right side of each end, making them ready for testing.

3.2.4 Tensile test

The tensile test was performed on the Instron 5985 testing machine, which is shown in Figure 3.9. It was carried out at room temperature. The extensometer had a movement capability of ± 10%. Since it was expected that the specimens would elongate beyond 10%, the test had to be stopped and the extensometer detached from the specimen during the test. It was crucial to prevent disruption during critical points of the test, as it could lead to incorrect measuring and results.

Figure 3.9 Instron 5985 tensile testing machine.

Wedge action tensile grips from Instron with a maximum load capacity of 30kN were used. Before placing the first specimen in the machine, the Bluehill Universal software was started on the computer connected to the Instron 5985. Required input values were given to obtain the desired results and output values. For the required input value regarding the thickness (a_0) and width (b_0) of the specimens, three arbitrary places were measured at the constricted area with a caliper, and the lowest value for thickness and width was used as input values. The extensometer measured a constant strain rate of $0{,}00025s^{-1}$ from the beginning of the test until the yield strength. From this point until the point of fracture, the strain rate was constant at $0{,}0067s^{-1}$. Additional information about the point at which the test was going to stop for the detachment of the extensometer was also given as input value.

Just before placing the specimen in the machine, the load cell was reset to zero. Then, one of the ends of the specimen was fasten to the bottom grip, and the upper grip was lowered to a level such that the upper end of the specimen could be fastened to it. When the specimen was properly fastened in the machine, the clip-on extensometer was clamped on to the constricted area. This procedure was followed for all the three specimens. However, TT2 and TT3, was accidentally placed with the unmachined side of the ends into the machine. This is further discussed in Chapter 5.2. After performing the tests, the resulting raw data generated on the Bluehill Universal was exported as a csv file to Python for further analyses. Stress-strain curves were plotted, and the results generated in Bluehill Universal were compared to the results generated in python. The tensile fractured surfaces were analyzed both by the naked eye and in SEM.

Figure 3.10 Fractured tensile specimens sectined and ready for SEM examination

3.3 Specimen preparation for optical microscope and SEM analyses

Multiple samples were extracted from the material block for microstructural examination using an optical microscope and SEM. The Olympus GX53 microscope and the Stream Essentials software were used for the optical analysis. Zeiss Supra 35VP microscope was used for SEM examination.

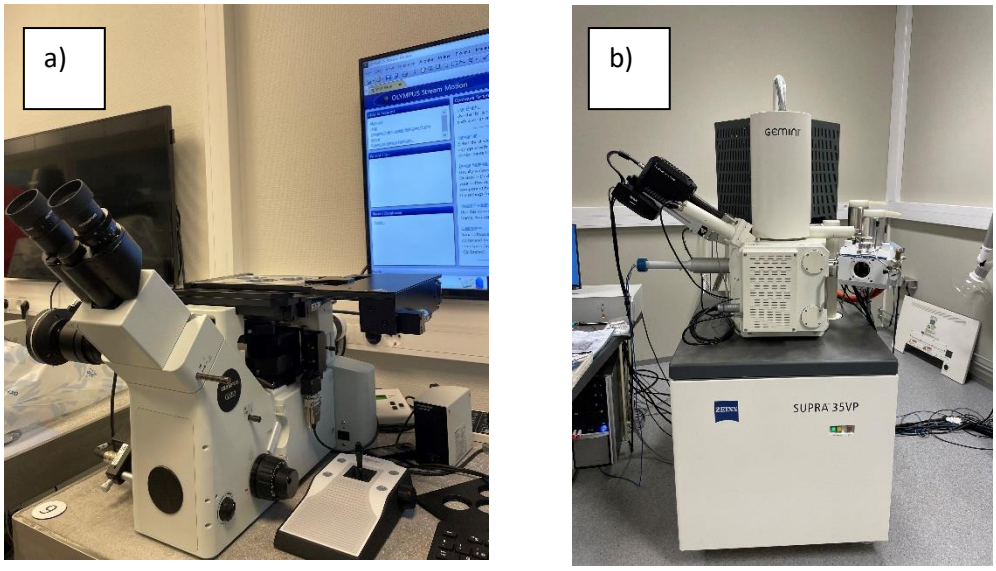

Figure 3.11 a) Olympus GX53 microscope and b) Zeiss Supra 35VP SEM

The samples were initially sectioned in the Struers Discotom 10, then cleaned and air dried. They were then hot mounted in Struers CitoPress-30. Samples that were going to be analyzed in optical microscope were mounted using multifast resin, while samples for SEM were mounted using polyfast, as this resin is electrically conductive.

Further, the samples were grinded and polished on Struers TegraForce-5. Initially, *Metallographic preparation of copper and copper alloys* [29] from Struers were used as grinding and polishing method. Challenges occurred as scratch free surfaces were difficult to achieve. Adjustments were made to the grinding and polishing method. An approximation of the final procedure is presented in Table 3.4.

Grinding					Polishing		
Step	1	2	3	4	5	6	7
	PG	FG 1	FG 2	FG 3	DP	DP	OP
Surface	Paper	Paper	Paper	Paper	MD-NAP	MD-Mol	MD-Chem
Abrasive type	SiC	SiC	SiC	SiC	Diamond	Diamond	
Abrasive size	#500	#1200	#2000	#4000	9µm	3µm	
Lubricant	Water	Water	Water	Water		DiaPro Mol R 3	OP-S
rpm	300	300	300	300	150	150	150
Force (N)	25	25	25	25	25	25	25
Time (min)	1	1	1	1	5	10	20

Table 3.4 grinding and polishing method. PG = plane grinding, FG = fine grinding, DP = diamond polishing, OP = oxide polishing, SiC = silicon carbide.

A specimen holder was used to grind the samples at the same time, to ensure similar surface treatments. The specimens were washed in the ultrasonic cleaner after each grinding and polishing step to prevent contamination that could scratch the sample surfaces. The surfaces were checked for each step to observe if less scratches appeared. Also, the grinding and polishing machine was washed and cleaned for each step. Some samples required additional polishing time to eliminate scratches. Before examining the samples in optical microscope or SEM, they were washed with ethanol and air dried.

Two of the samples, named top and bottom sample, were extracted from the zy-plane (ref Figure 3.1) for SEM examination, EBSD analyses and for localizing and measuring dendrites with the optical microscope. A third sample, extracted from the middle region of the block in the xy-plane, was also examined in SEM and EDS.

Both etched and unetched samples were examined in the optical microscope. Two different etching methods were tested. They were based on the *Metallographic preparation of copper and copper alloys* [29] from Struers were adjustments. Table 3.5 represents the etchant for the methods. Samples were initially etched for 15 seconds before examined under the microscope. Additional time were added if needed.

Method 1	**Method 2**
25ml water	34g sodium disulfate
2,5g ammonium peroxydisulfate	100ml sodium thiosulfate

Table 3.5 Methods for etching

3.4 Specimen preparation for Vickers hardness test

Two specimens, VHT1 and VHT2 (Vickers hardness test one and two respectively) were sectioned from the middle and the edge of the original block, as shown in Figure 3.12. The dimension of VHT2 was (70x30)mm (height x width), and (70x17)mm for VHT1. Initially, the plan was to have specimens that were of the same length as the block (99mm), one from the edge and one from the middle, to investigate how the material's hardness properties varied as function of:

1) distance from the top, and
2) the distribution of phases in the local region for each specific indention

However, this turned out to be more challenging than anticipated.

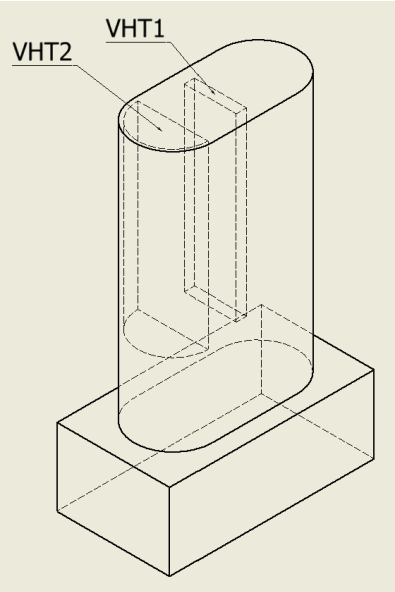

Figure 3.12 VHT1 and VHT2 extracted from the original block.

VHT1 and VHT2 were mounted into epoxy. There was no available equipment for such big samples to be mounted. Therefore, the samples had to be shortened from the bottom to a length of 70mm, instead of 99mm. Since it was desirable to determine hardness properties at the bottom as well, Vickers hardness test was also performed on the remaining bottom material of the block that was left on the base from the very first sectioning. The surface that the hardness test was performed on was approximately 3mm from the base.

To minimize the risk of contamination and scratches during grinding and polishing, the samples were mounting under vacuum. Figure 3.13 shows the samples placed in their mounting holders. An additional sample were mounted because the sample holder could hold three samples during grinding and polishing. The benefit of having three samples in the holder was to achieve equilibrium, which made it easier to grind and polish evenly throughout all the sample surfaces. The solidification time for the mounting was approximately 48 hours.

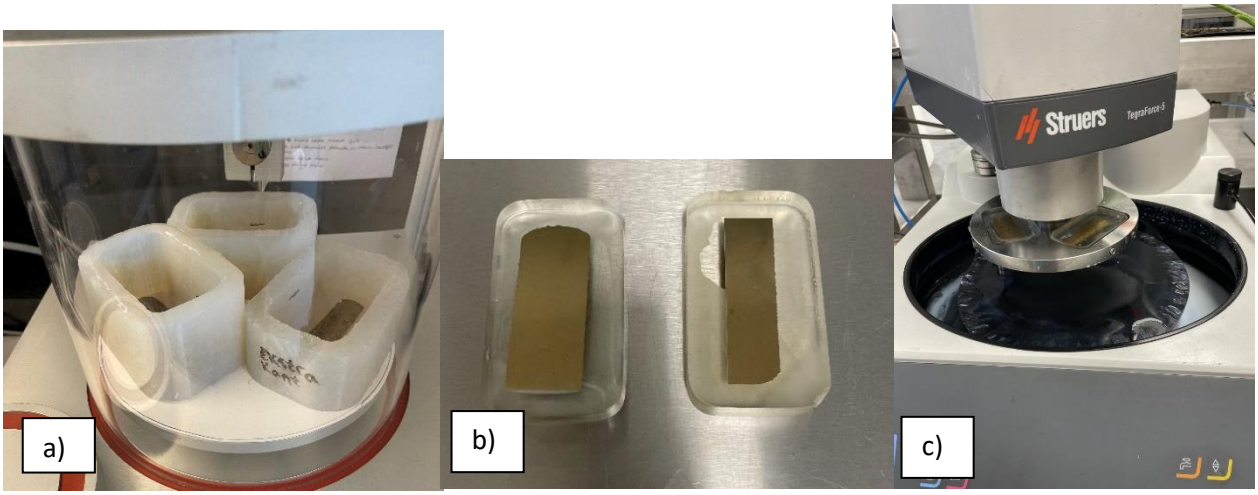

Figure 3.13a) VHT1, VHT2 and an extra sample placed in mounting holder ready for mounting, b) VHT1 (right) and VHT2 (left) mounted into epoxy and c) Grinding av polishing on Struers TegraForce-5.

It was attempted to use the same method for grinding and polishing as described in Table 3.4. However, it was not possible to use the ultrasonic cleaner because the specimens were too big. Therefore, they had to be washed manually with warm water, soap, and a clean sponge between each grinding and polishing step. The surfaces were still not scratch free. It was decided to try and grind and polish manually on Struers Pedemax-2 with one sample at the time, in case one of the samples were contaminated. Scratch free surface was still not achieved. Therefore, it was not possible to do the microstructural analysis, which was necessary to determine the distribution of phases. As a result, only Vickers hardness test was carried out.

3.5 Vickers hardness test

The Vickers hardness test was carried out according to NS-EN ISO 6507-1:2018 [30]. It was performed with HV5 load, 10 seconds dwell time, and a diamond indenter. VHT1 and VHT2 were performed on the automatic Falcon 5000 hardness testing machine, while the NOVA330 machine was used for the bottom specimen. 472 hardness indenters were done automatically on VHT1, distributed on seven lines. 467 hardness indenters were done on VHT2, which also were distributed on 7 lines. See Figure 3.14 for illustration. For each line, there were one millimeter between each indenter. There were 2 mm between each line of indention. 40 hardness indentions were done on the bottom sample, as illustrated in Figure 3.15.

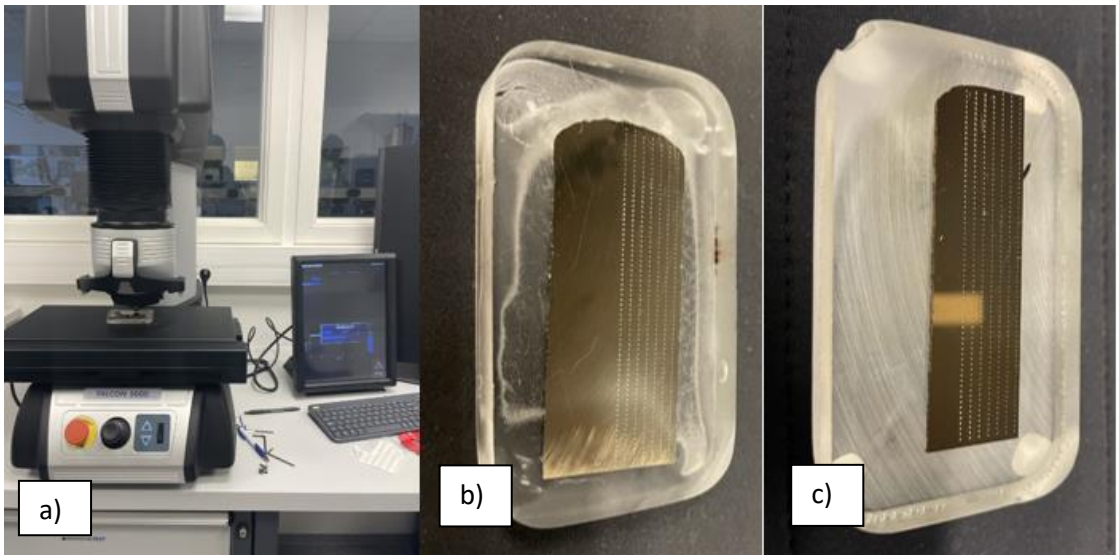

Figure 3.14 a) Falcon 5000 hardness testing machine, b) VHT2 467 indenters and c) VHT1 472 with indenters.

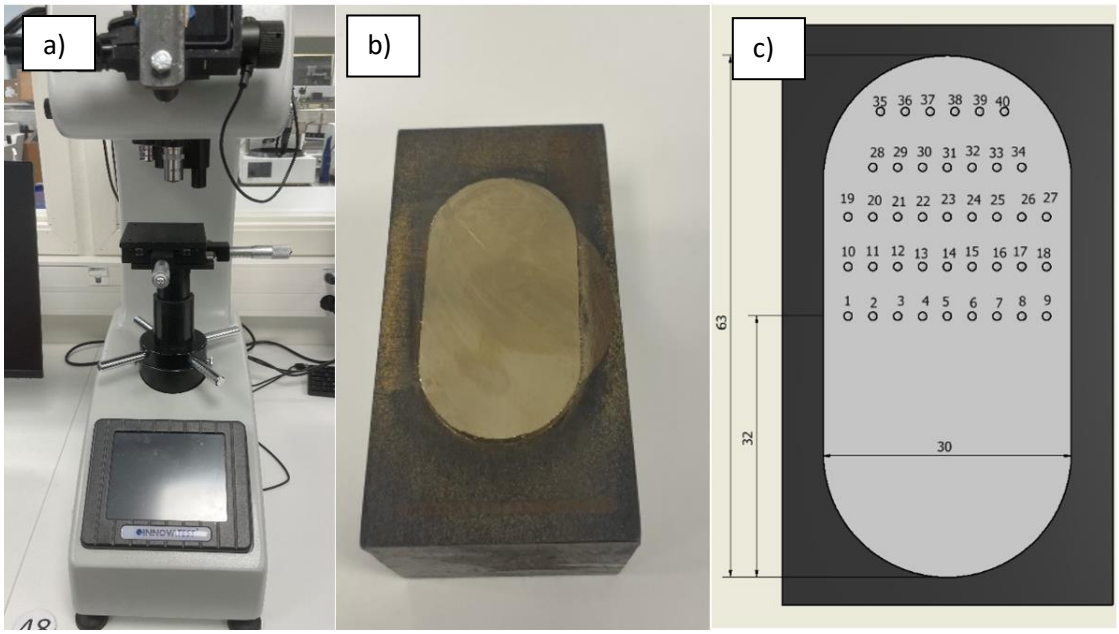

Figure 3.15 a) NOVA330 hardness testing machine, b) bottom sample, approximately 3mm from the base and c) Location on the bottom sample where the indenters were performed.

3.6 Dendrite measuring and local cooling rate calculations

It was desirable to identify the local cooling rate at the top and at the bottom of the original block. The two samples used for this purpose, named top and bottom sample, were located approximately five mm from the very top of the block and 10 mm from the base at the bottom. Each of the two samples had an area of approximately 110mm^2. The distance between the top and bottom sample was approximately 86 mm. Both surfaces were parallel to the building direction and in the zy-plane. A magnification of 100X was used on the optical microscope and the whole surfaces of the two samples were inspected. 11 dendrites were measured on the top specimen, and ten on the bottom.

For each dendrite that was found during inspection, a line was drawn on the secondary dendrite arms, parallel to the primary dendrite arm. The following formula was then used to calculate the average SDAS for that particular dendrite:

$$SDAS = \frac{L}{N-1} \tag{3.2}$$

Where L is the length of the drawn line, and N is the number of secondary dendrite arms crossing L. The number of lines that were needed to be drawn per dendrite depended on how linear the primary arm was. Equation (3.2) was used for each line and the average SDAS per dendrite was calculated. After measuring the SDAS on every appearing dendrite, the average SDAS on the total sample was calculated. Equation (3.3) was used to calculate the local cooling rate on each sample.

$$\lambda = B * \dot{T}^{-n} \tag{3.3}$$

Where λ is the average SDAS, B is a material dependent constant, set to be 50 in this case, $\dot{T}$ is the cooling rate ($°C/s$), and n is a constant equal to 1/3.

4. Results

4.1 Charpy V test

Table 4.1 represents the results from the Charpy V test regarding the absorbed energy for CVT1, CVT2 and CVT3. They were measured with the digital measuring instrument. CVT1, which absorbed the highest amount of energy, absorbed approximately 56% more energy than CVT3, which absorbed the least amount of energy. The fractured surfaces are shown in Figure 4.1.

Initial potential energy (of the hammer) [J]	450
Absorbed energy CVT1 [J]	46.4
Absorbed energy CVT2[J]	28.7
Absorbed energy CVT3 [J]	26.1
Mean [J]	33.7
STD	11.0

Table 4.1 Absorbed energy results from Charpy V tests. Measured with the digital measuring instrument.

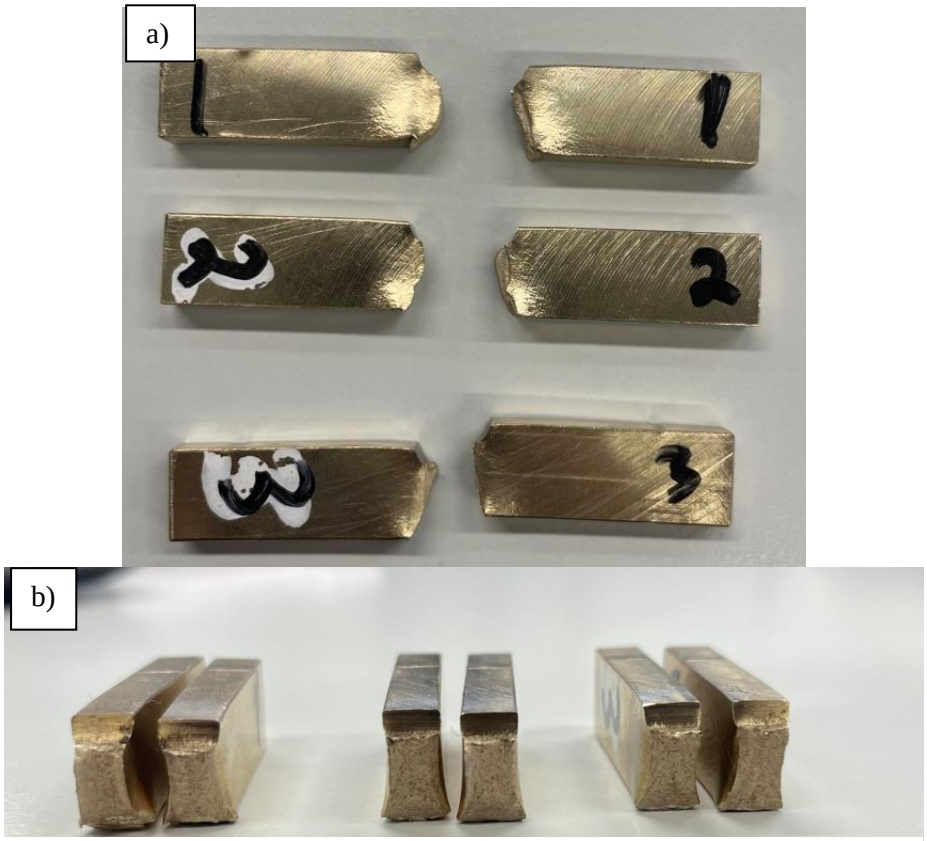

Figure 4.1 Fractured Charpy specimens. a) the numbers marked 1, 2 and 3 corresponds to CVT1, CVT2 and CVT3 respectively. The edge of the fractured surface on CVT1 were quite round-shaped. b) CVT1 to the left, CVT2 in the middle and CVT3 to the right.

The fractured surfaces from all three specimens were in general quite fibrous. They were taller on the side edge of the surfaces compared to the inner part of the surfaces. Especially CVT1 formed quite a round-shaped edge (Figure 4.1). This drastic difference in height from the outer and inner region of the surface were not as drastic for CVT2 and CVT3. When studying the fractured surfaces with the naked eye, it was also possible to observe dark spots.

By studying one of the fractured surfaces from CVT1 in SEM with 39x magnification (Figure 4.2), one could observe elongated cracks. Most of them were elongated in a direction parallel to the long side of the V-notch, and perpendicular to the direction that the hammer was striking the specimen (looking at Figure 4.2, the hammer was striking in a direction from right to left). The cracks appeared mostly near the V-notch region, but also further down in the fractured surface.

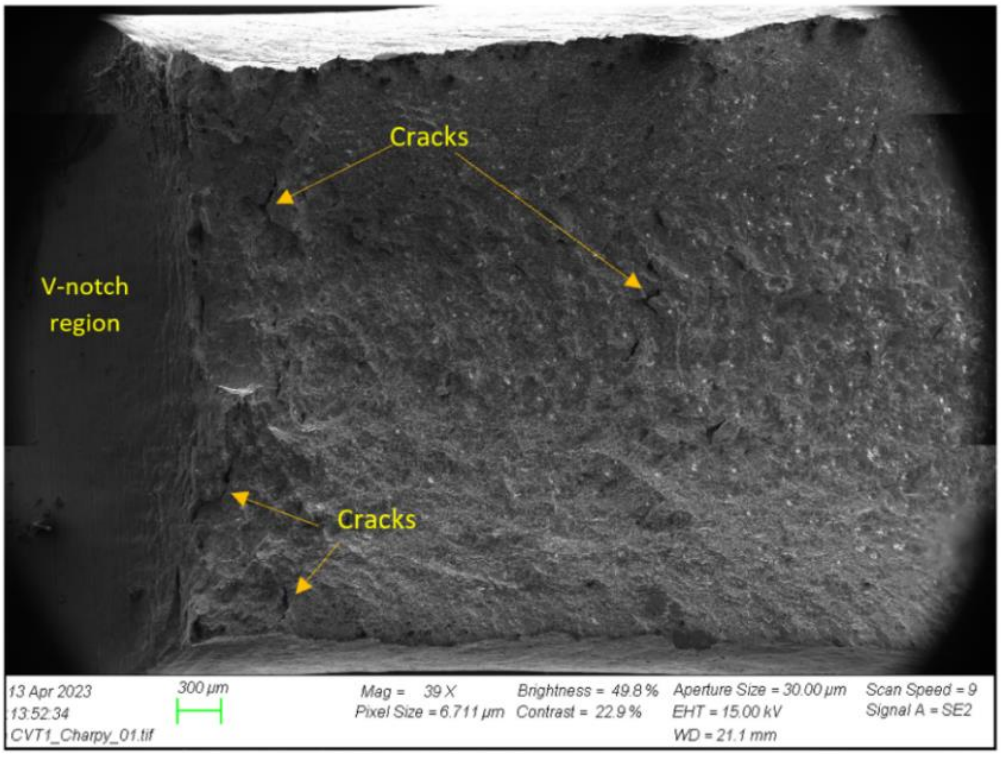

Figure 4.2 SEM image with 39x magnification of CVT1 fractured surface.

Hardly any cracks were observed in SEM on the fractured surface of CVT2 and CVT3 with 46x magnification (4.3a)) and 56x magnification (4.3b)) respectively. Small white particles were also observed on all the three specimen's fractured surfaces. No pores were observed in SEM on these images.

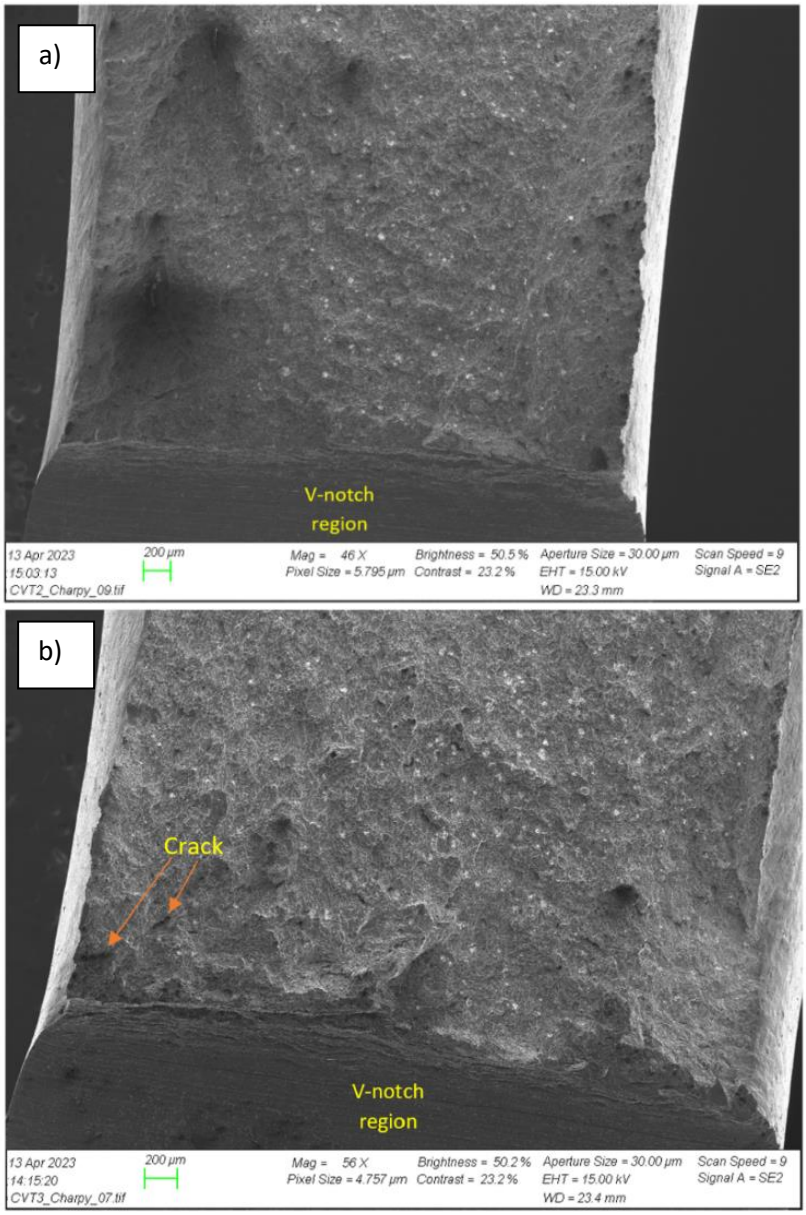

4.3 a) SEM image with 46x magnification of CVT2 and b) 56x magnification of CVT3, both showing hardly any cracks.

From examining the same fractured surface in SEM with a higher magnification (Figure 4.4), it was discovered that the surfaces consisted of elongated dimples. Many of the dimples were parabolic shaped. It was possible to observe microvoids within the dimples in Figure 4.4d).

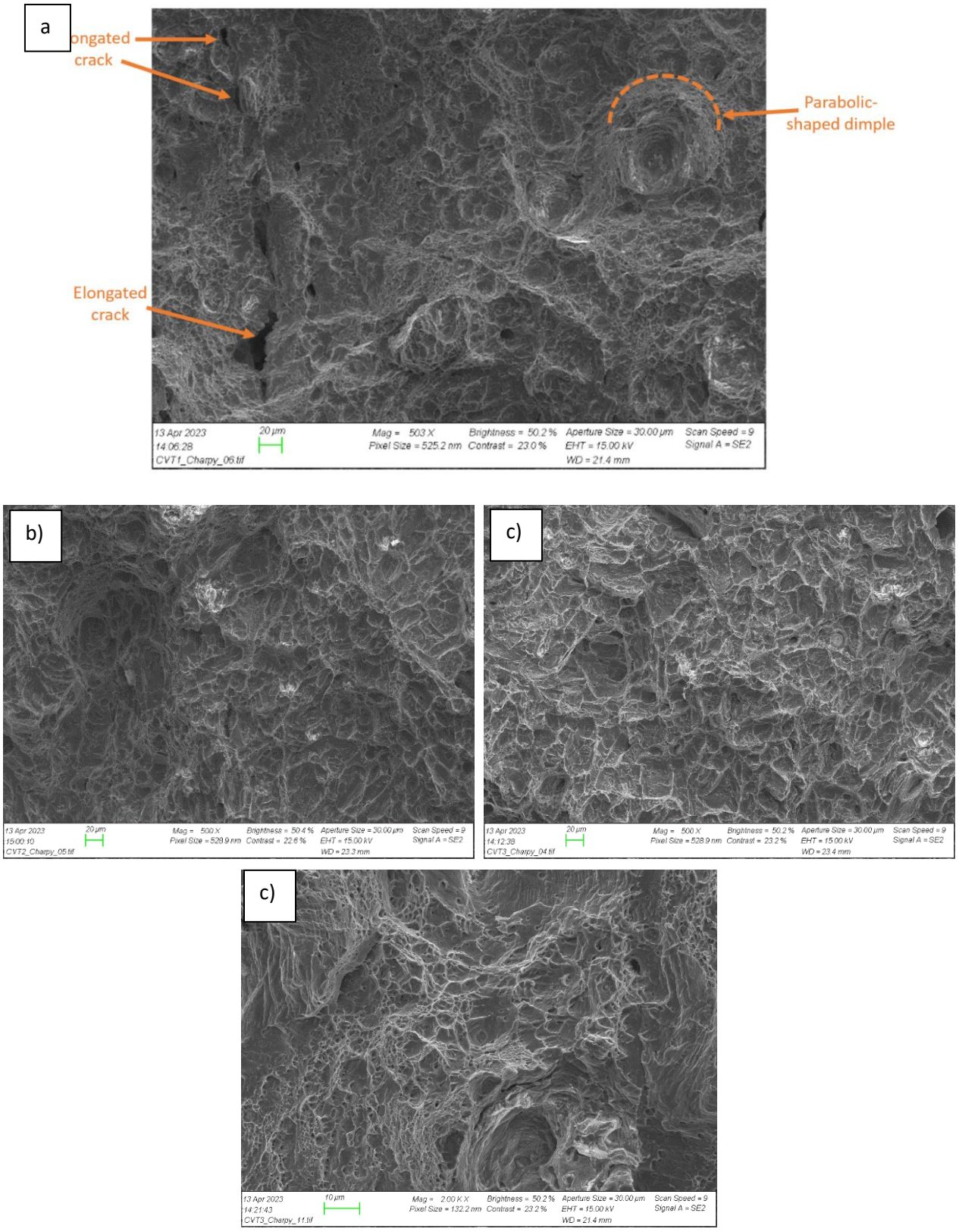

Figure 4.4 SEM images of fractured surfaces of a) CVT1 (503x magnification), b) CVT2 (500x magnification), c) CVT3 (500x magnification) and d) CVT3 (2.00Kx magnification).

4.2 Tensile Test

The stress-strain curves for TT1, TT2 and TT3 shown in Figure 4.5 were generated in Python by importing the raw data from the csv-file from Bluehill Universal. The stress-strain curves generated directly by Bluehill Universal are not as precise as the ones generated in Python. However, they are included in Appendix A. Stress-strain curves generated for each specimen separately are also included in Appendix A.

The small drop or disturbance that one could observe in the stress-strain curves were a result of the test being stopped to detach the clip-on extensometer. It was done successfully at a non-critical point, minimizing any disruption for the results.

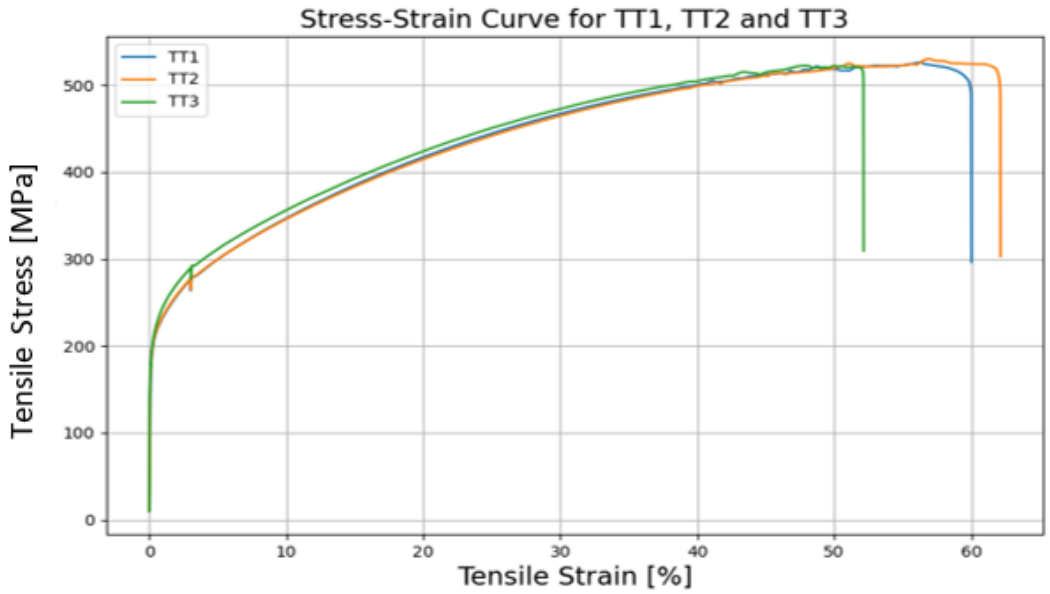

Figure 4.5 Stress-strain curve for TT1 (blue line), TT2 (orange line) and TT3 (green).

Based on Figure 4.5, the results did not vary much between the three tensile test specimens. However, the results regarding the modulus of elasticity (shown in Table 4.2) varied quite a lot between the specimens. To investigate this further, a new plot was plotted in Python, focusing on the elastic region. The result is shown in Figure Figure 4.6.

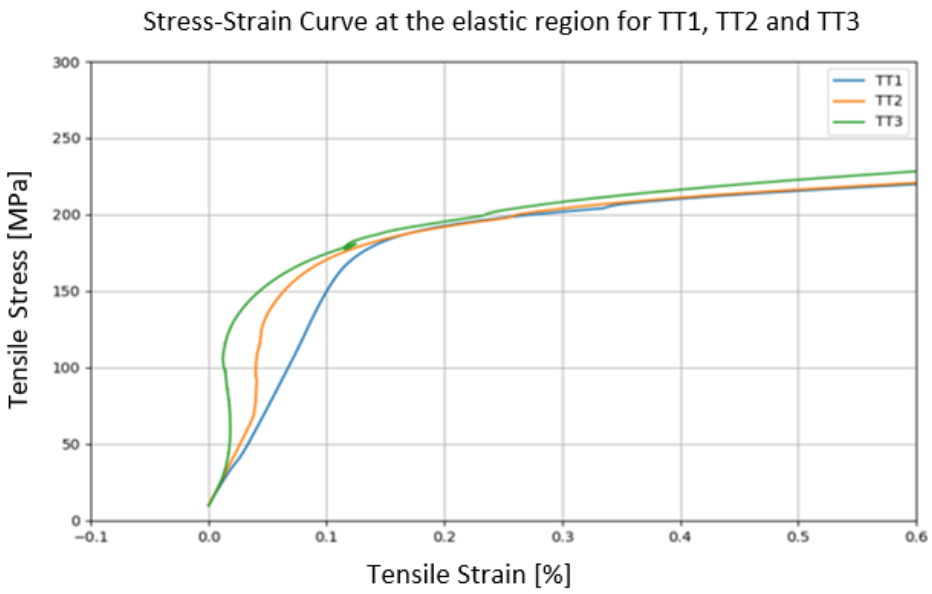

Figure 4.6 Stress-strain curve at the elastic region for TT1, TT2 and TT3 showed measuring error.

It was clear from Figure 4.6 that the elastic region of the curves was not linear for TT2 and TT3, which indicated that something interrupted the test. Possible reasons for this error are discussed in Chapter 5.2. Regardless of the cause for this error, it is important to state that the E-module, especially for TT2 and TT3 should not be considered as representative results for this material.

The results presented in Table 4.2 were generated by the Bluehill Universal software. One additional column was included with the tensile strength generated in Python. Based on the mean values, the ultimate tensile strength was approximately 38% higher than the yield strength. The elongation at break generated by the software were higher than expected. When the elongation for TT1 were measured manually, it was found to be approximately 45%.

	Modulus of Elasticity [GPa]	Yield strength (offset 0.2%) [MPa]	UTS [MPa]	UTS calculated in Python [MPa]	Elongation at tensile strength at non-proportional elongation [%]	Elongation at break at non-proportional elongation [%]
TT1	132	206.82	546.49	546.49	55.93	59.6
TT2	195.31	204.23	527.9	530.07	57.3	61.82
TT3	345.65	203.64	522.56	522.56	47.51	51.75
Mean	224.32	204.90	532.32	533.04	53.58	57.72
STD	109.74	1.69	12.56	3.76	5.30	5.29

Table 4.2 Tensile test results.

Figure 4.7 shows the specimens after fracture. All the fractured surfaces were quite fibrous and had the cup-and-cone fracture shape, as shown closely on TT1.

Figure 4.7 Fractured tensile test specimens. 1, 2 and 3 corresponds to TT1, TT2 and TT3.

From the SEM examination of TT1 at 46x magnification (Figure 4.8) one could observe the height differences on the fractured surface. Some black spots were also possible to observe at this magnification.

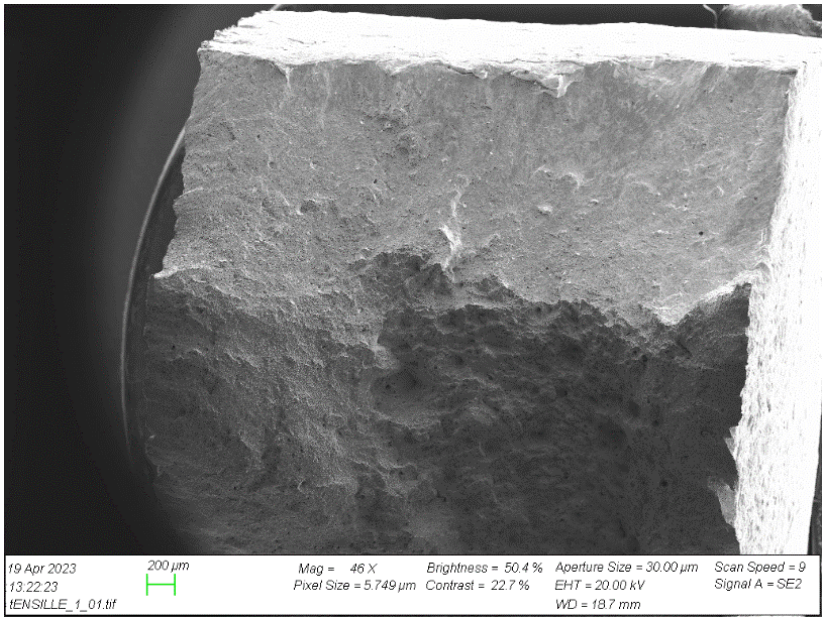

Figure 4.8 SEM image of TT1 fractured surface with 46x magnification.

At 2 000x magnification (Figure 4.9) one could observe elongated dimples and microvoids.

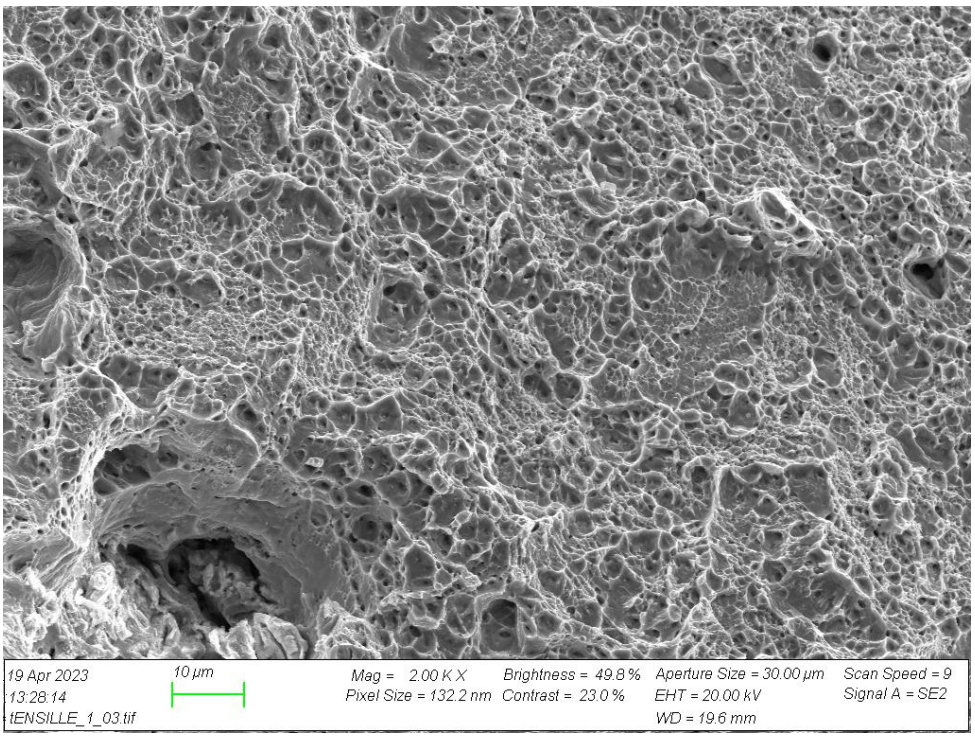

Figure 4.9 SEM image of TT1 fractured surface with 2.00Kx magnification.

4.3 Vickers hardness test

A summary of the results from Vickers hardness test performed on the bottom part of the block are presented in Table 4.3. The hardness values for every indenter are presented in Appendix B.

Mean HV:	152.6
STD:	7.3
Max HV:	166.8
Min HV:	139.3

Table 4.3 Vickers hardness test results from the bottom sample.

The results from Vickers hardness test performed on VHT1 are shown in Figure 4.10 and Table 4.4. The top line of indention is from the middle part of the original block. The bottom line of indention was supposed to be done closer to the edge of the material. However, it was executed approximately 6mm away from the edge. The colormap and corresponding scale shown in Figure 4.10a) and b) corresponded to the measured hardness values over the VHT1.

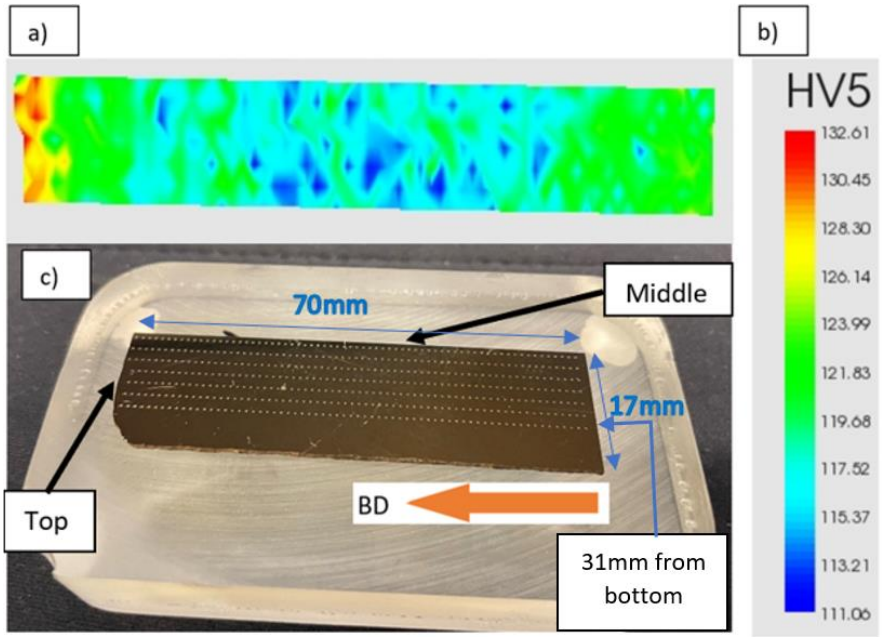

Figure 4.10 Vickers hardness test results for VHT1. a) colormap over the area corresponding to VHT1 and b) the corresponding scale. C) the 472 harndess indenters distributed on 7 lines with 2mm between each line.

VHT1	
Mean HV	118,9
STD	3,8
Max HV	133
Min HV	110,0

Table 4.4 Vickers hardness results for VHT1.

Figure 4.11 shows the Vickers hardness values for the top and bottom line as a function of distance from the top.

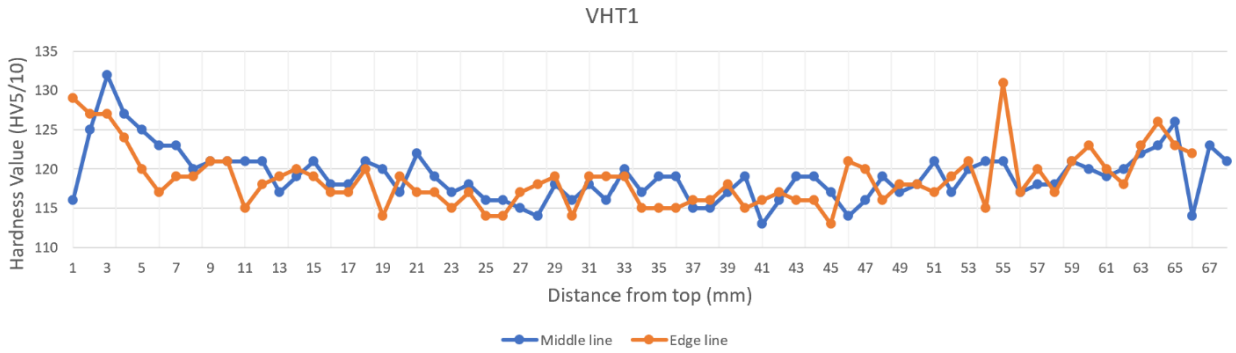

Figure 4.11 Hardness as a function of distance from the top for the top and middle line in VHT1.

The results from the Vickers hardness test performed on specimen VHT2 are shown in Figure 4.12 Table 4.5. The top line of indention is from the edge of the original block and the bottom line from the middle. The result of the test is presented in the same way as for VHT1.

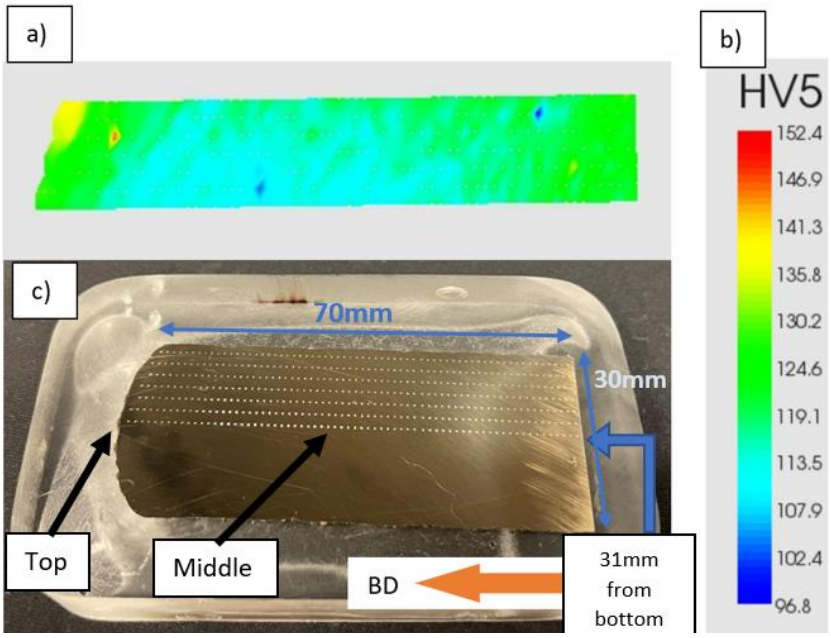

Figure 4.12 Vickers hardness test results for VHT2. a) colormap over the area corresponding to VHT2 and b) the corresponding scale. c) the 467 harndess indenters distributed on 7 lines with 2mm between each line.

VHT2	
Mean HV	117,5
STD	5,3
Max HV	141,191
Min HV	101,9

Table 4.5 Vickers hardness results for VHT2.

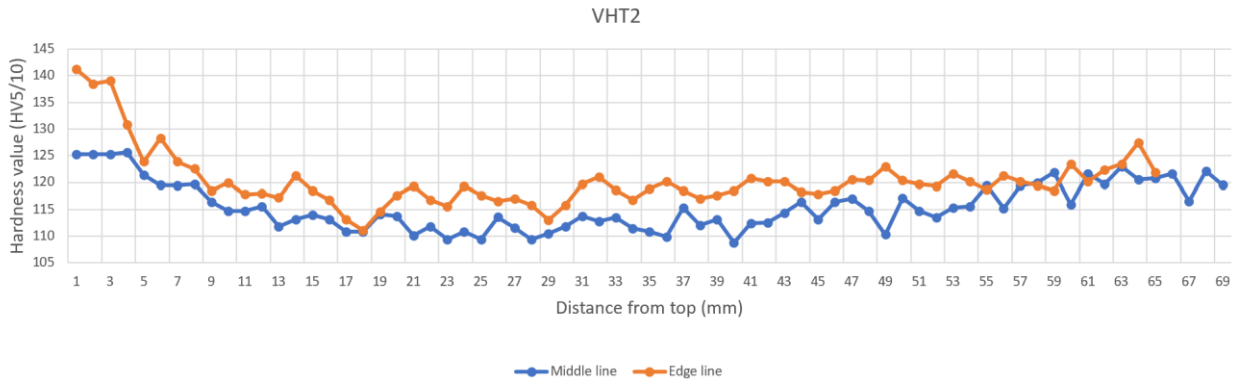

Figure 4.13 Hardness as a function of distance from the top for the top and middle line in VHT2.

A total of almost 1000 hardness indenters were done on the material. Combining all the results from the hardness tests for VHT1, VHT2 and the bottom sample, a summary of the results is presented in Table 4.6.

TOTAL HARDNESS RESULTS	
Mean HV	135,0
STD	10,4
Max HV	166,8
Min HV	101,9

Table 4.6 Total result from the Vickers hardness tests performed on the material.

4.4 Optical microscope

The optical microscopic images shown in **Feil! Fant ikke referansekilden.** and **Feil! Fant ikke referansekilden.** from etched samples did not turn out to help investigate the microstructure successfully . However, they are included because they are still results that are important for future work. Dendritic structures were observed in unetched samples (Figure 4.16). It was difficult to identify other microstructural features when examining the microstructure in the optical microscope, without SEM examination. The yellow area observed in Figure 4.15 could possibly be an oxide. The darker areas that appeared in Figure Figure 4.14 were not diffracting in the SEM analysis, which made it difficult to draw any conclusion regarding them.

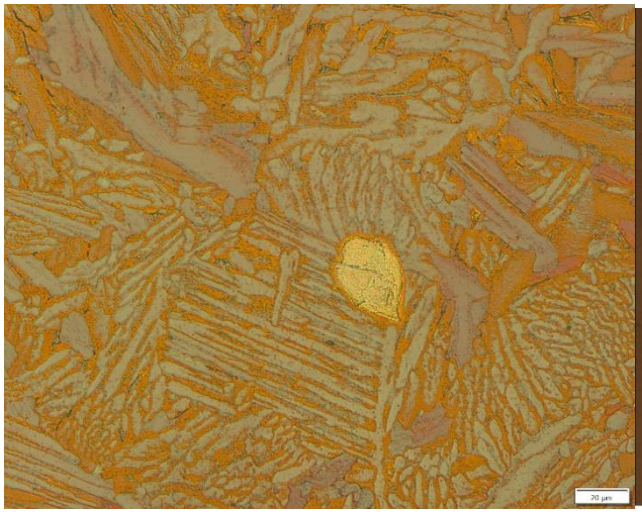

Figure 4.15 Etched sample from the middle of the block in the zx-plane. Etching method 2. Etching time: 30 seconds. The length of the scale bar in the bottom right corner is 20µm.

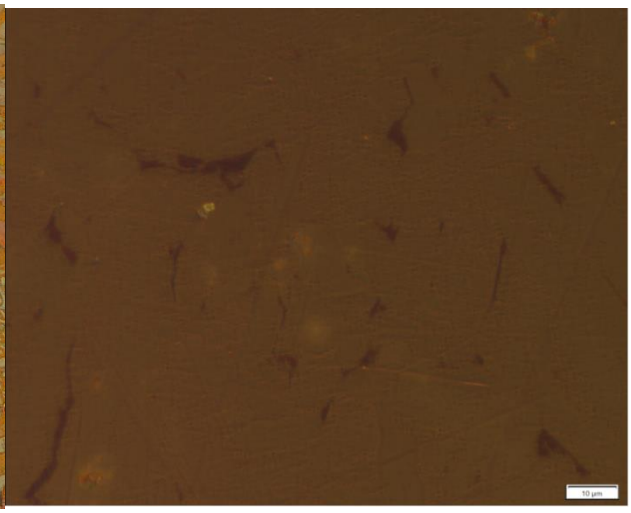

Figure 4.14 Etched sample from the middle of the blcok in the zx-plane. 100x magnification. Etching method 1. Etching time: 45 seconds. The length of the scale bar in the bottom right corner is 10µm.

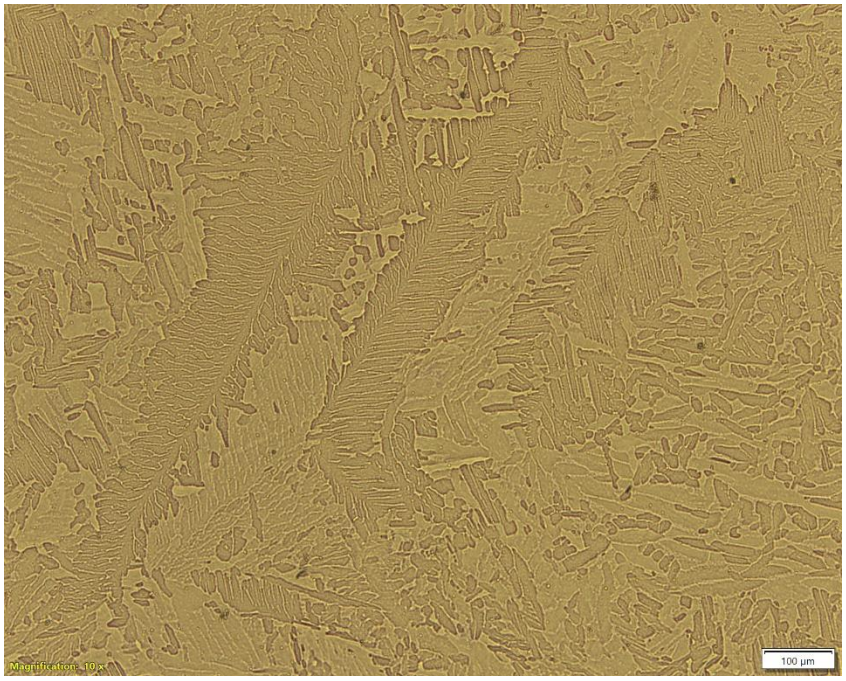

Figure 4.16 Dendritic structure appearing in unetched sample from the top in the zy-plane. The length of the scale bar in the bottom right corner is 100µm.

4.5 Dendrite measuring and local cooling rate calculations

All the calculations for the SDAS can be found in Appendix C. The mean SDAS for the top and bottom sample are represented in Table 4.7. Figure Figure 4.17 shows one of the dendrites from the top sample that were used in the calculations. Additional dendrites are included in Appendix C.

	Top	Bottom
Mean SDAS [µm]	11,01	9,28
STD	2,07	1,63

Table 4.7 Mean SDAS and STD for the top and bottom sample.

Using the mean SDAS value for the top and bottom sample, and Equation $\lambda = B * \dot{T} - n$ (3.3), the following local cooling rate were calculated for the top and the bottom sample:

$$\dot{T}_{top} = \left(\frac{SDAS}{B}\right)^{-\frac{1}{3}} = \left(\frac{11{,}01}{50}\right)^{-\frac{1}{3}} = 1{,}656℃/s$$

$$\dot{T}_{bottom} = \left(\frac{SDAS}{B}\right)^{-\frac{1}{3}} = \left(\frac{9{,}28}{50}\right)^{-\frac{1}{3}} = 1{,}753℃/s$$

$$\left(1 - \frac{\dot{T}_{top}}{\dot{T}_{bottom}}\right) * 100\% = \ 5{,}5\%$$

The mean cooling rate was $1{,}656℃/s$ for the top sample and $1{,}753℃/s$ for the bottom sample. The bottom had a 5,5% faster local cooling rate compared to the top.

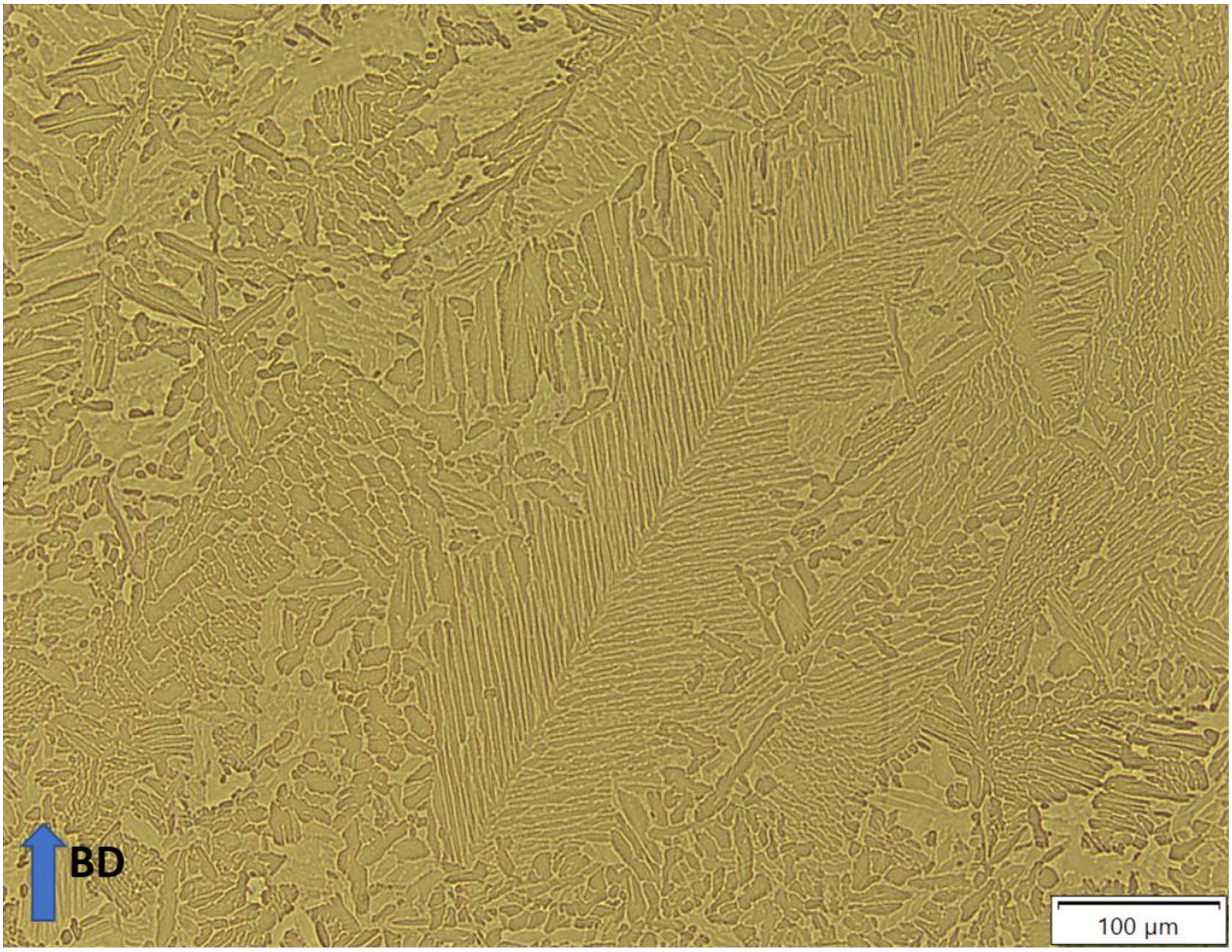

Figure 4.17 one of the dendrites from the bottom sample zy-plane.

4.6 SEM

SEM images of the top sample from the zy-plane is shown in Figure 4.18 and Figure 4.19. κ precipitates or particles were present at grain boundaries and near grain boundaries. The grains were lamella shaped. A different crystal structure was appearing near the grain boundaries. Similar microstructures were observed in the bottom sample, which is included in Appendix D.

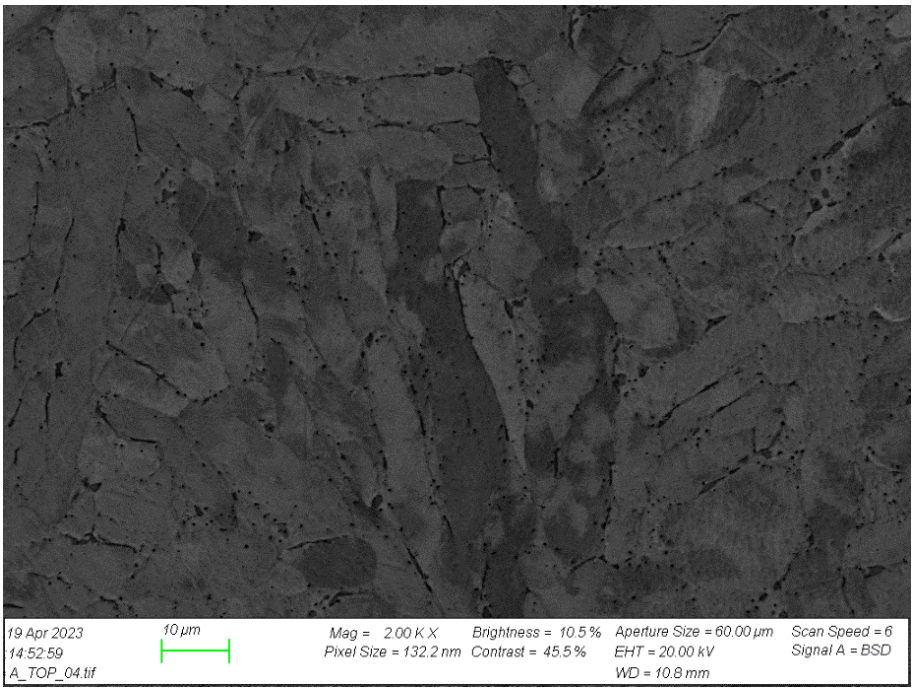

Figure 4.18 SEM image with 2.00k x magnification of the top sample from the zy-plane showing lamella-shaped grains. Precipitate particles were located at the grain boundaries.

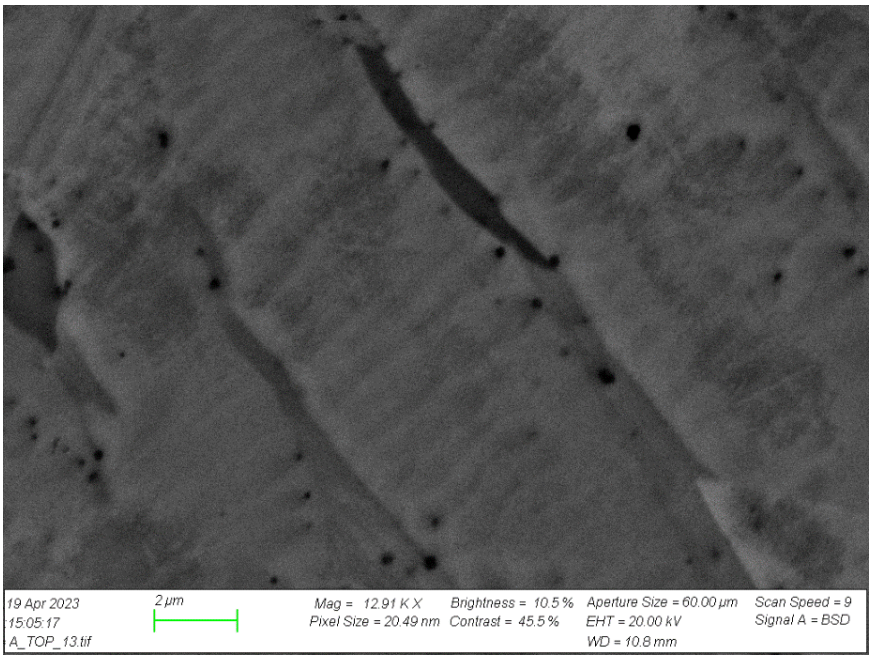

Figure 4.19 SEM image with 12.91k x magnification of the top sample showed a different crystallographic structure at near grain boundaries.

From the middle sample studied in the SEM one of the few observed cracks were seen, as shown in Figure 4.20.

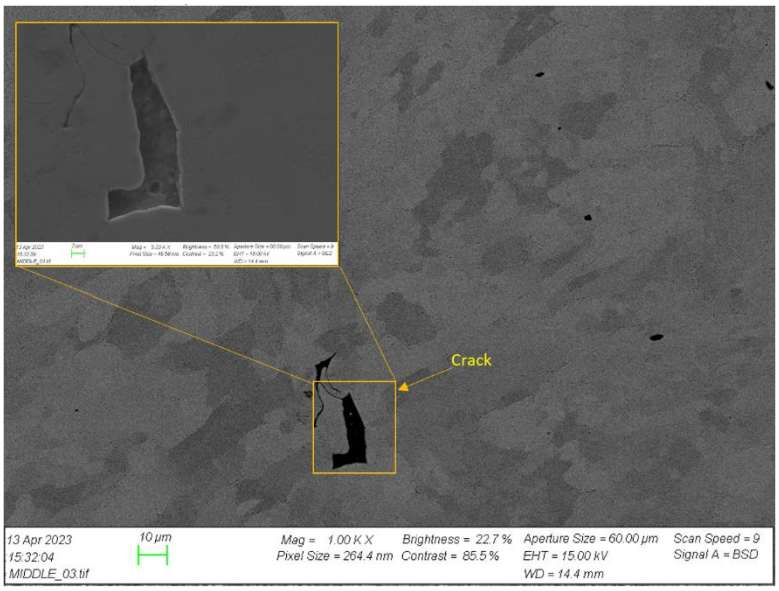

Figure 4.20 SEM image with 1.00 x magnification of the middle sample from the xy-plane showed one of the few cracks that were observed.

4.6.1 EBSD

The EBSD orientation color code shown in Figure 4.23b) was used to evaluate the crystallographic orientation of the appearing grains in the top sample with the color map shown in Figure 4.23. Some parts of the surface were not diffracting, which resulted in the uncomplete colourmap. However, the copper-rich FCC crystal structure were diffracting. The graph shown in Figure 4.21 presents the distribution of the varying grain size diameter. The average grain size given was 19,4µm with standard deviation of 17,6. The average area of the grains were 66,0 μm^2 with standard deviation of 52,2. The standard deviation were this high due to big differences in grain size. Raw data regarding grain size is included in Appendix E. Figure 4.21 showed elongated lamella-shaped microstructure. Unfortunately, the knowledge of the direction of printing got lost during the EBSD analysis of this sample.

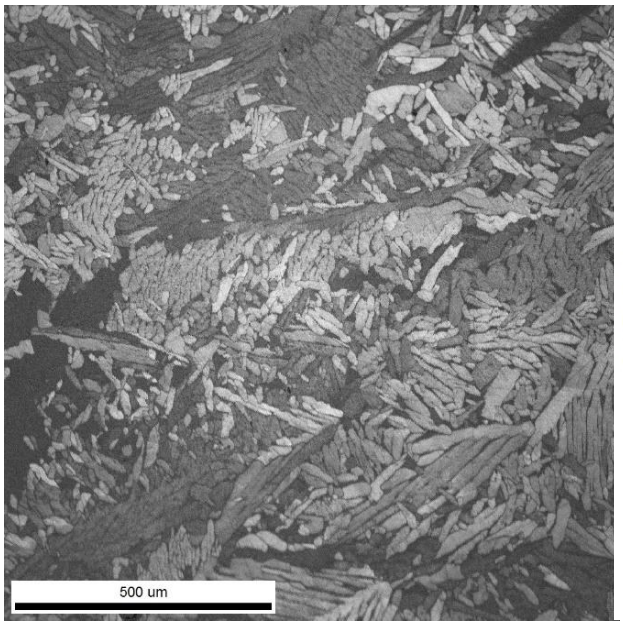

Figure 4.21 Quality image of the top sample.

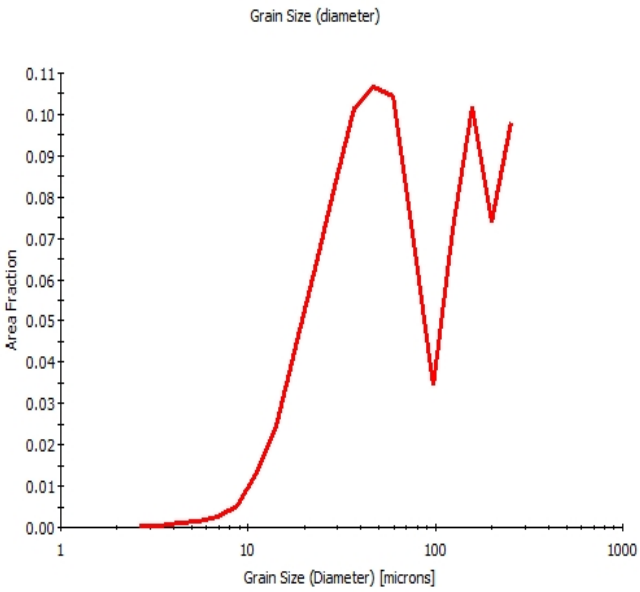

Figure 4.22 Grain diamter size distribution in the top sample.

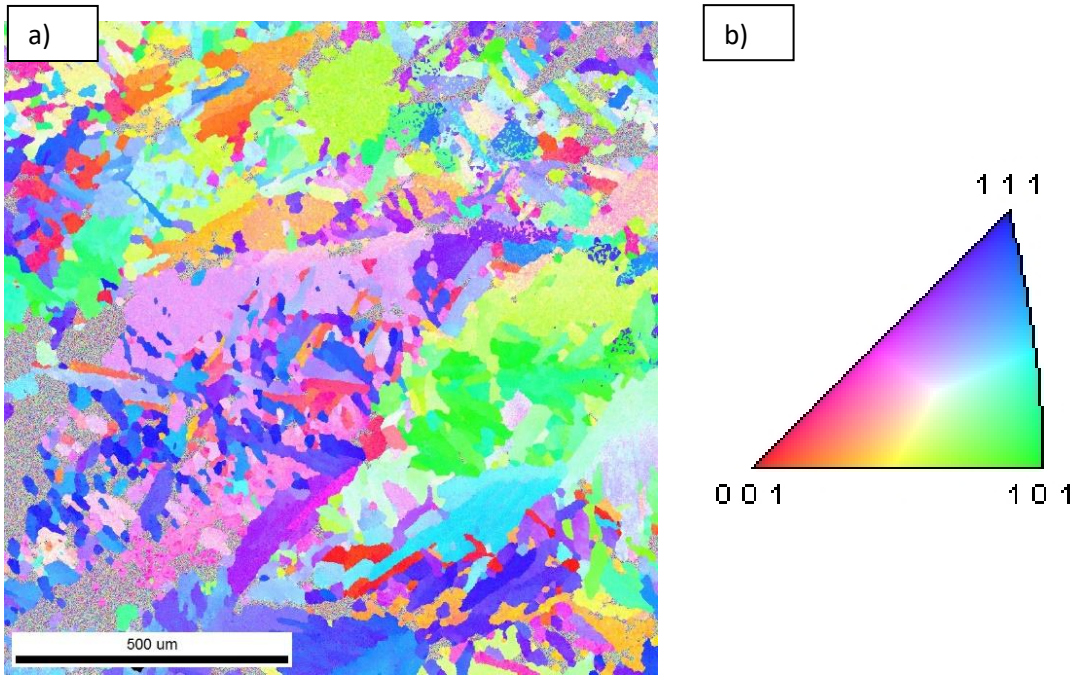

Figure 4.23 a) Crystallographic orientation color map of the top sample and b) orientaion color code.

Figure Figure 4.25 of the bottom sample showed elongated grains, however the clear lamella structure that were observed in the top sample were not appearing as clearly in the bottom sample. The average measured grain size was 19µm with standard deviation of 17,6. The average area of the grains were 52,2 μm^2 with standard deviation of 52,2. The raw data is included in Appendix E. The bottom specimen showed a more or less complete colormap. Using the same inverse pole figure as for the previous sample (figure++) and the color map, one could observe that the crystallographic orientation varied throughout the surface. Most of the grains were standing somewhat vertically in the BD.

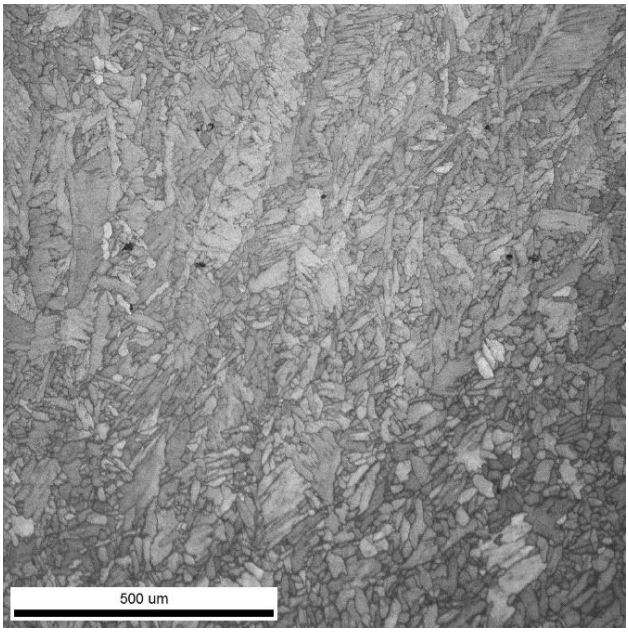

Figure 4.25 Quality image of the bottom sample.

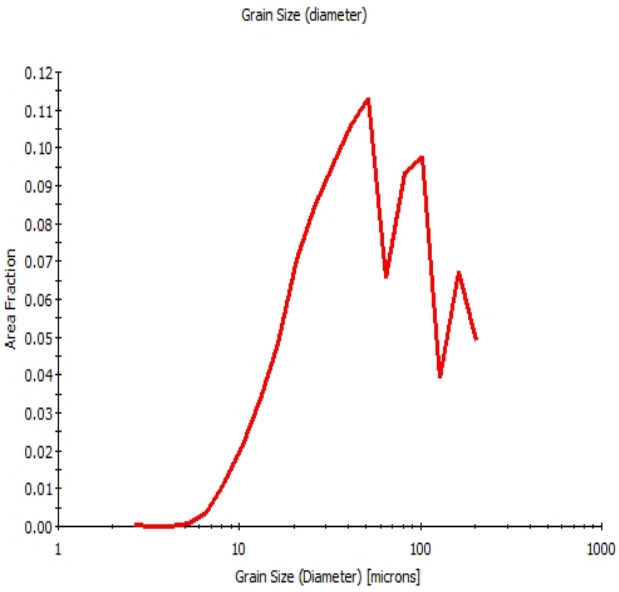

Figure 4.24 Grain diamter size distribution in the bottom sample.

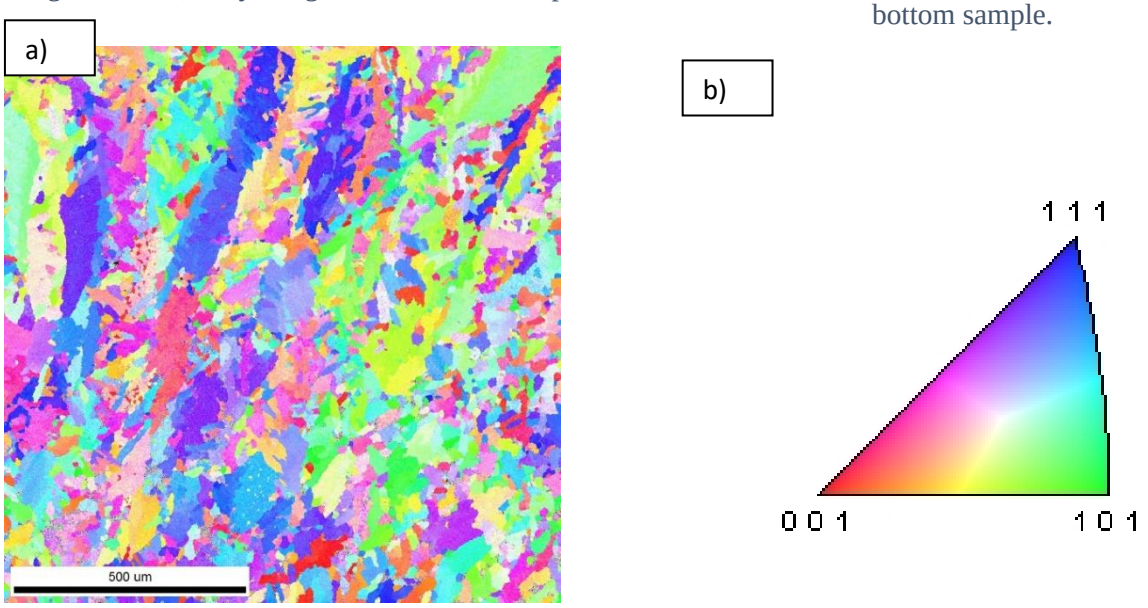

Figure 4.26 a) Crystallographic orinentaion colour map of the bottom sample and b) orientaion color code.

4.6.2 EDS

The EDS analysis were performed on the middle sample to identify the chemical composition of the κ particles and the matrix, as shown in figure Figure 4.27. Figure 4.28 and Table 4.8 EDS Chemical analysis of the of the κ particles.shows the resulting chemical composition of the κ particle. Figure 4.29 and Table *4.9* shows the resulting chemical composition for the matrix.

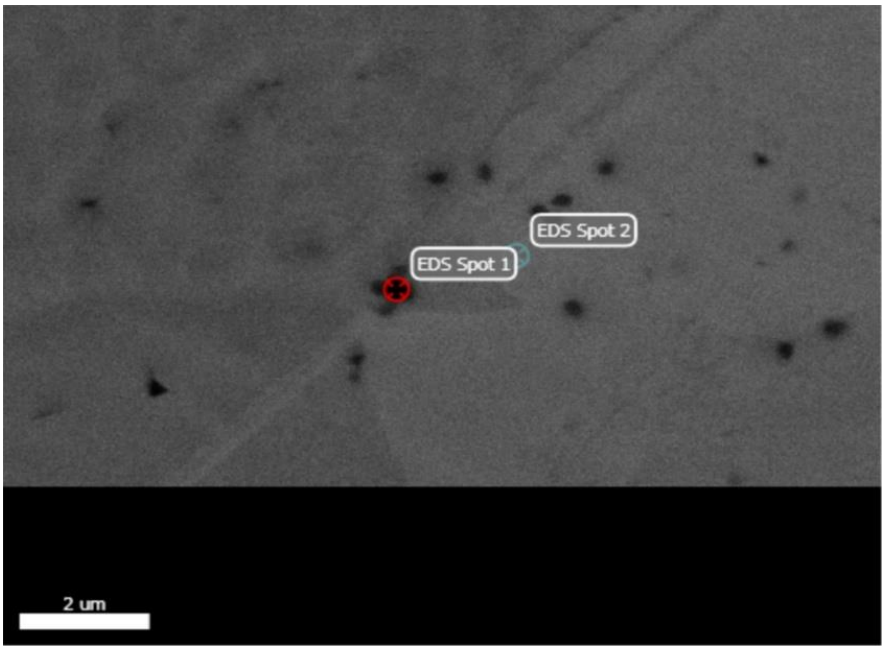

Figure 4.27 EDS analysis of the κ particles (Spot 1) and matrix (spot 2).

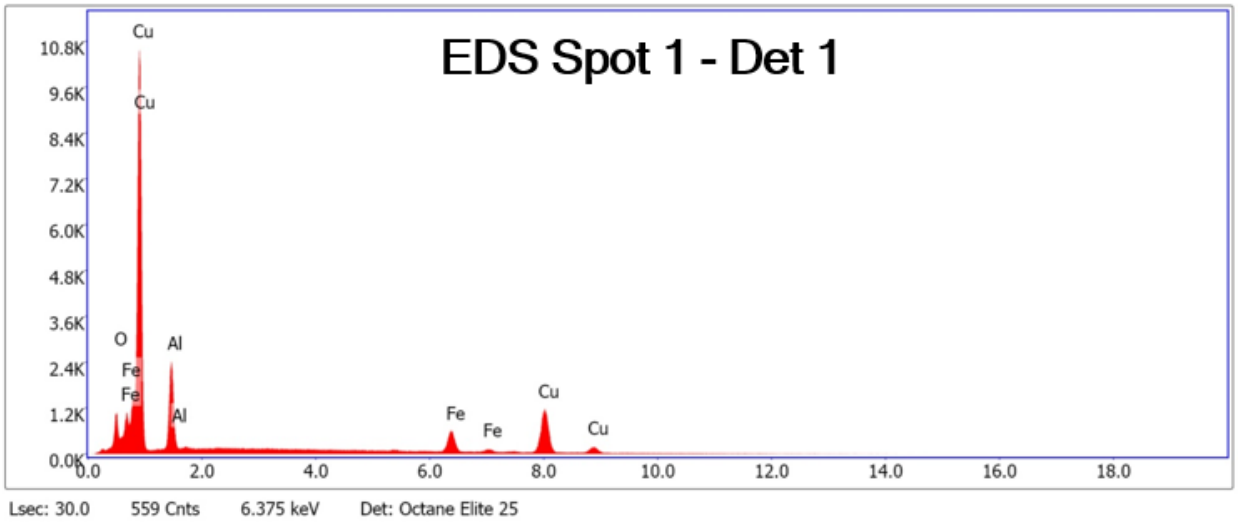

Figure 4.28 EDS chemical analysis of the of the κ particles

Element	Weight %	Atomic %	Net Int.	Error %	Kratio	Z	A	F
O K	3.89	11.81	439.33	7.88	0.0242	1.2890	0.4832	1.0000
AlK	12.69	22.88	1329.14	7.52	0.0679	1.1476	0.4655	1.0009
FeK	13.81	12.03	514.90	5.18	0.1497	0.9913	0.9957	1.0978
CuK	69.61	53.28	1198.69	3.87	0.6594	0.9494	0.9941	1.0037

Table 4.8 EDS Chemical analysis of the of the κ particles.

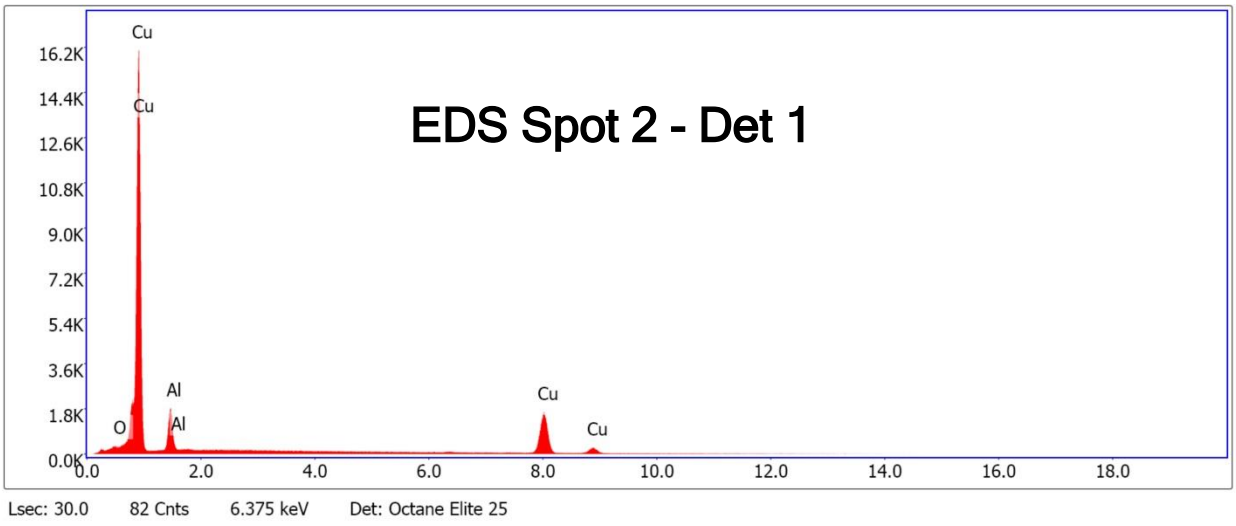

Figure 4.29 EDS chemical analysis of the of matrix.

Element	Weight %	Atomic %	Net Int.	Error %	Kratio	Z	A	F
O K	0.98	3.37	117.15	11.27	0.0060	1.3162	0.4661	1.0000
AlK	9.10	18.60	975.23	8.12	0.0463	1.1724	0.4337	1.0009
CuK	89.92	78.03	1716.06	3.51	0.8778	0.9745	1.0003	1.0014

Table 4.9 EDS Chemical analysis of the of the matrix.

5. Discussion

5.1 Charpy V Test

More cracks appeared in CVT1, compared to CVT2 and CVT3. This was also the specimen that absorbed the most energy during the Charpy V test. If the cracks that appeared in the Charpy specimens were there originally from the 3D-printing and not a result of the Charpy test, one would have expected the specimen with the highest number of cracks, CVT1, to be the easiest specimen for the hammer to strike through. In other words, the specimen with the most cracks should absorb the least amount of energy. However, this was not the case according to the SEM examination that was done on the fractured surfaces. The opposite was seen. The specimen with the most cracks absorbed the most amount of energy. This could have indicated that the cracks were not there originally, but rather a result of the Charpy test.

The fact that CVT1 absorbed the most energy, approximately 56% more energy than CVT3, could have been a sign that this specimen was the most ductile out of the three specimens. As a result, the pendulum experienced more resistance from the material during the strike.

The different results that were seen in CVT1 compared to CVT2 and CVT3 regarding the absorbed energy might be due to the machining of the V-notch during the preparation. The V-notch that was made with the V-notch broaching machine did not turn out to be centered on the first specimen, CVT1. This problem with the broaching machine was fixed before creating the notch on CVT2 and CVT3. However, the incorrect positioning of the notch on CVT1 could have led to incorrect results. This might be the reason why the results for the first specimen differed from the two others.

The three Charpy V specimens had different fractured surfaces that one could observe with the naked eye. The fractured surface of CVT1 had quite a round-shaped edge, and were deformed plastically to a greater extend, compared to CVT2 and CVT3. This could have indicated that CVT1 were more ductile. However, this might also have been related to the placing of the V-notch on CVT1, as mentioned above.

Regarding the observation obtained from the SEM analysis, not many differences were seen between the three specimens. Most of the appearing dimples in all the specimens were elongated and parobol-shaped, which is typical for ductile materials. Microvoids or pores were also observed in SEM. These could be the source for the cracks that appeared.

Generally, to achieve results that reflect the properties of a material accurately, it is necessary to conduct more than three tests. This is important because errors are prone to occur during practical work. By performing multiple tests, including trial tests, would reduce the chances for errors and increase the

probability of obtaining representative results. However, in this case, the limited available material prevented the execution of additional tests. With that said, the results presented in this thesis are not necessary entirely unrepresentative. Furthermore, it would also have been interesting to carry out Charpy test on specimens orientated perpendicular to the printing direction, to observe how the results potentially could have varied.

5.2 Tensile test

The results for the three specimens regarding the modulus of elasticity varied quite a lot, which is most likely due to measurement errors. It was also not expected that the values were going to be this high, especially for TT2 and TT3. When the stress-strain curve was plotted in python, focusing on the elastic region, one could observe that the graph was not linear for TT2 and TT3, which also indicated that something was incorrect. In certain parts of the elastic region, the slope of the graph was negative, which is not possible. This was most likely due to the incorrect positioning of TT2 and TT3 in the testing machine. Figure 5.1 shows how TT3 were placed in the machine.

Figure 5.1 TT3 after fracture. The incorrect positioning of the specimen in the grips resulted in the load not to pull uniaxially along the long axis of the specimen.

Figure 5.2 illustrates how TT1 was gripped correctly in the testing machine. One can see the marks left on the ends of the specimens after performing the tensile test due to the gripping. The length of the region at which the grip was holding onto one of the ends of TT1 evenly from the centerline of the specimen, such that the load would be applied uniaxially along the long axis of the specimen.

Figure 5.3 illustrates how TT2 was gripped incorrectly in the testing machine. The grip was not gripping evenly over the center line of the long axis of the specimen, which resulted in the load not to be applied uniaxially. This could have caused the specimen to bend somewhat, which again could lead to the extensometer to slip on the specimen. This is most likely why the E-module was measured incorrectly. The same applied to TT3, which is included in Appendix A. The results regarding the E-module for TT2 and TT3 are therefore not representative. The E-module for TT1, which was 132GPa, could have been a representative result. However, more tests are required in order to confirm if this result is valuable.

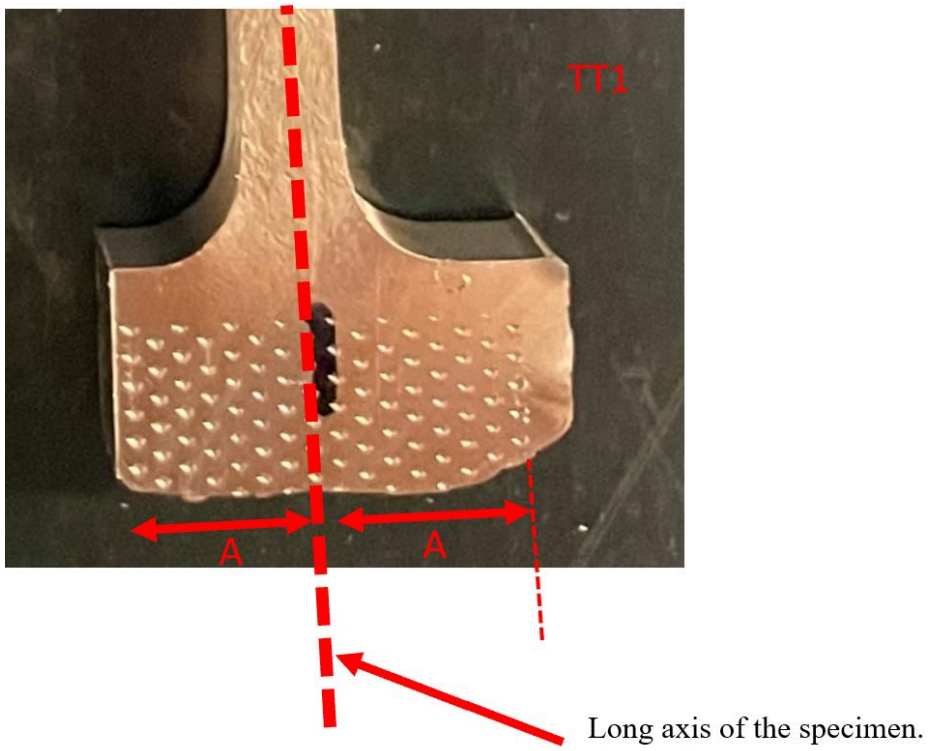

Figure 5.2 One can see the marks left on the ends of the specimen after performing the test due to the gripping. A + A = the length at which the grip was holding onto one of the ends of TT1. This was done successfully, such that the load would be applied uniaxially along the long axis of the specimen.

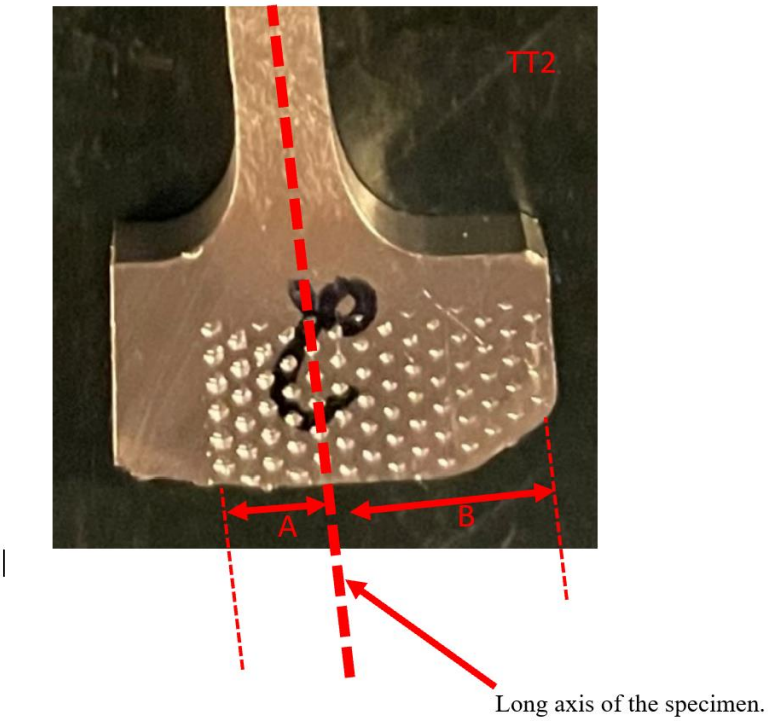

Figure 5.3 A + B = the length at which the grip was holding onto one of the ends of TT2.It was not gripping evenly over the long axis of the specimen, which caused the load to not apply uniaxially along the long axis of the specimen.

Table 5.1 compares the tensile test results from the test performed in this thesis and the test done by SINTEF for NAM on the same material.

	Aluminum bronze	Aluminum bronze (SINTEF)
Youngs modulus of elasticity [GPa]	224,32	-
Yield strength Rp 0,2 [MPa]	204,9	353
UTS [MPa]	533,04	672
Elongation at break [%]	57.72	17,3

Table 5.1 Tensile test results compared with SINTEF results.

Regarding the yield strength, the results did not vary much between the three specimens. Comparing the mean yield strength found in this thesis, which was 204,9 MPa, to what SINTEF measured, the difference is about 45 MPa.

The tensile strength did not vary much between the specimens and seemed to be somewhat representative. The values were a bit lower than that of the results from SINTEF. Regarding the total strain, the results were

quite high, also compared to the results from SINTEF. The elongation at break for TT1 were studied afterwards and were to be approximately 45%, which was still quite high.

When the fractured surfaces were studied, typical shear fractures were observed. The fractures were cup-and-cone shaped and quite fibrous. During necking, the microvoids that formed and kept growing into cracks as the test went on are the reason for the dimples and microvoids that were observed in SEM. The formation of elongated elliptical cracks in the center region of the specimen caused the creation of deformation bands 45 degrees from the direction of the applied force, which resulted in the cup-and-cone shear fractures that were observed after the tests were finished. The shape of the dimples that were observed in SEM, were also indicating that the material was ductile, because they were elongated.

Just like with the Charpy V-test, in order to obtain representation information regarding tensile properties of the material, conducting more than three tensile tests is necessary. To determine the E-module, it was necessary that the specimens were at least 50mm long. Due to the limited amount of material given, running additional tests were not possible. Additionally, it would have been interesting to perform the tests with specimens orientated perpendicular to the printing direction to observe differences.

5.3 Vickers hardness test

All the hardness values calculated were less than 150HV, which, according to the theory (chapter 2.8.3), indicates that the aluminum bronze was ductile and soft.

The hardness results from both VHT1 and VHT2 showed that the hardness values were highest at the top of the material and decreased towards the middle part, and then started to increase again. However, the hardest part of the block was the bottom part. This could be due to higher cooling rate or faster solidification process at the bottom, due to the low temperature of the base material that the aluminum bronze were printed onto. This would have led the formation of smaller grains and more grain boundaries that worked as barriers for dislocation movements. The mean value for VHT1 and VHT2 were 119 and 117 respectively, and there were not big differences in overall hardness between the two specimens.

On specimen VHT2, there was a systematic decrease in hardness properties between the inner and outer part of the specimen. This was not clear from the color map of VHT1. It could be because the test done on the edge line on VHT1 was not done as far at the edge as with VHT2. It could also have been due to the change of hardness as a function of displacement in the middle part of the block (VHT1) did not vary as much as for VHT2. This could indicate that the variation in solidification rate were greater in the outer part of the block than in the middle.

There could have been contamination in the bottom material from the base material, which could have affected the results. Another factor that should be considered when comparing VHT1 and VHT2 to the results from the bottom sample, is that they were from different planes. VHT1 and VHT2 were from the zy-plane, which is parallel to the BD, and the bottom sample are from the xy-plane, which is perpendicular to the BD. There are reasons to assume that this also affected the results.

A more precise explanation for the results would have been achieved if the microstructure of the specimens were investigated in microscope. The material has anisotropic properties, which means that the specific area where the indenter penetrated the surface would vary, depending on the local microscopic properties. Observation of the microstructure of VHT1 and VHT2 was not done because of the challenge that occurred of achieving a scratch free surface, which was crucial for a successful microscopic investigation. The size of the specimens were too big to fit into the ultrasonic cleaner. Ideally, the ultrasonic cleaner would have been used between each step of the grinding and polishing process, to minimize contamination. Since this, unfortunately, was not achieved, the surface contained scratches that made the specimen not suitable for microstructural investigation.

5.4 Optical microscope and local cooling rate

Dendritic structures were observed on most unetched sample under optical microscope examination. The calculated results indicated that the bottom sample had a local solidification rate that was approximately 5,5% faster than in the top sample, which was expected, as the base contributed to faster rate of solidification during printing. It would have been interesting to calculate the size of the SDAS in the dendrites in samples from the middle of the block, to see if the local solidification rate was even lower. This would be assumed as the middle region is exposed to more heat.

Other microstructural properties were not successfully identified with the optical microscope. Additional time should have been spent on etching to improve the optical microscopic images and investigation.

5.5 SEM

5.5.1 EBSD

Some of the regions in the crystallographic orientation color maps were not diffracting, especially for the top sample. This was most likely because the surface of these specific areas had been removed during polishing in the preparation process. However, it indicated that these areas on the surface were of different chemical composition or phases and reacted differently to the mechanical preparation.

Regarding the grain size determined in the EBSD analysis, the biggest grains were approximately 200µm in diameter in the bottom sample. Looking at the size of the dendrites observed in the same sample in the optical microscope, they were bigger than the grains observed in the EBSD analysis. It was not expected

that the dendrites were bigger than the grains, because dendrites do not have different crystallographic orientation. It could be an indication that the observed dendrites are not from the same area as the EBSD analyses has been done. The EBSD-analyses were done on an area of approximately (1000µm*1000µm) 1000mm of the sample, which is around 1/10th of the total sample area. Therefore, the grains where the dendrites were located were likely bigger than the once found in the EBSD analyses.

6. Conclusion

The results from the Charpy V test and tensile test indicated that the aluminum bronze was quite ductile. Regarding the specific values that was found from the two tests, such as the absorbed energy in the Charpy tests and the E-module in the tensile test, they should not be treated as entirely representative. This was due to the sources of error that occurred when the tests were carried out. The SEM images could also have been affected by this. Additional Charpy tests and tensile tests should be performed to obtain more representative results regarding toughness and tensile properties of the material. Three samples for each test was simply not enough.

The results regarding the hardness values indicated that the aluminum bronze was ductile and soft. The results were more or less representative. However, the results, which heavily depended on the microstructure, were not explained at a microscopic level due to the difficulties with achieving scratch free surfaces. For future work, different specimen preparation methods should be tried to successfully investigate the microstructure, which heavily affects the hardness properties.

From SEM analysis, it was possible to identify the iron-rich κ precipitates, which contributes to strength and hardness to the material. The EBSD analysis on the aluminum bronze were not entirely successful, because of the difficulties with identifying other phases than the FCC. Despite trying different preparation methods and input values to the EBSD program regarding assumed phases, the results did not improve. However, with more time, the results would probably improve, and is therefore recommended for future work. TEM analysis should also be performed to obtain valuable information, such as the relevant phases. Unfortunately, due to time constrains, this was not done in this thesis, but should be a part of future work.

7. References

[1] Ø. Grong, *Sveisemetallurgi*. 1990.

[2] *Metallic materials Charpy pendulum impact test Part 1: Test method (ISO 148-1:2016)*, NS-EN ISO 148-1:2016, 2016.

[3] H. J. Meigh, *CAST AND WROUGHT ALUMINUM BRONZES PROPERTIES, PROCESSES AND STRUCTURE*. Maney, 2000.

[4] S. Kou, *WELDING METALLURGY*, 2. ed. Wiley - Interscience, 2003.

[5] "About Additive Manufacturing " Loughborough University. https://www.lboro.ac.uk/research/amrg/about/ (accessed.

[6] B. Lloyd, J. Peter, R. Joshua, G. Dro, and G. Michael, "Strain Rate Dependency of Bronze Metal Matrix Composite Mechanical Properties as a Function of Casting Technique," *Journal of Materials Engineering and Performance,* vol. 21, no. 7, pp. 1462-1467, 2012/07/01 2012, doi: 10.1007/s11665-011-9996-y.

[7] I. T. Tore. "SINTEF." https://snl.no/SINTEF (accessed.

[8] D. W. Callister Jr. and D.G. Rethwisch, 10., Ed. *Callister´s Materials Science and Engineering*. Wiley, 2020.

[9] "About Additive Manufacturing Powder Bed Fusion." Loughborough University. https://www.lboro.ac.uk/research/amrg/about/the7categoriesofadditivemanufacturing/powderbedfusion/ (accessed.

[10] C. V. "The Complete Guide to Directed Energy Deposition (DED) in 3D Printing." 3dnatives.com. https://www.3dnatives.com/en/directed-energy-deposition-ded-3d-printing-guide-100920194/#! (accessed.

[11] "WHAT IS DIRECTED ENERGY DEPOSITION (DED)?" https://www.twi-global.com/technical-knowledge/faqs/directed-energy-deposition (accessed 15.02.2023.

[12] A. C. Reardon, *Metallurgy for the Non-Metallurgist*, 2. ed. Ohio, USA: ASM International, 2011.

[13] B. Pedersen. "Kobber." Store Norske Leksikon. https://snl.no/kobber (accessed 28.04.2023.

[14] E. M. Schlesinger, *Extractive metallurgy of copper*, 5th ed. Amsterdam: Elsevier, 2011.
[15] L. Collini, *COPPER ALLOYS - EARLY APPLICATIONS AND CURRENT PERFORMANCE - ENHANCING PROCESSES*, Croatia, Rijeka, 2019.
[16] T. K. B. Pedersen, "Aluminium." [Online]. Available: https://snl.no/aluminium
[17] I. Richardson and C. Powell, "Guide to Nickel Aluminum Bronze for Engineers." [Online]. Available: https://www.copper.org/applications/marine/nickel_al_bronze/pub-222-nickel-al-bronze-guide-engineers.pdf
[18] D. W. Callister Jr. and D. G. Rethwisch, *Callister´s Materials Science and Engineering*, 10. ed. Wiley, 2020.
[19] "WHAT IS THE HEAT AFFECTED ZONE (HAZ)?" https://www.twi-global.com/technical-knowledge/faqs/what-is-the-heat-affected-zone (accessed 06.04.2023.
[20] A. K. Rosvold. "gradient (temperaturgradient)." https://snl.no/gradient_-_temperaturgradient (accessed 22.04.2023.
[21] C. R. E. Vandersluis, "Comparison of Measurment Methods for Secondary Dendrite Arm Spacing," doi: https://doi.org/10.1007/s13632-016-0331-8.
[22] M. Lindegren. "Hardness Testing and Specimen Preparation." Struers. https://www.struers.com/en/Knowledge/Hardness-testing# (accessed.
[23] T. L. Anderson, *FRACTURE MECHANICS Fundamentals and Applications*, 4. ed. Taylor & Francis Group, 2017.
[24] J. H. J.P. Goodhew, R. Beanland, *Electron Microscopy and Analysis*, 3. ed. Taylor & Francis, 2000.
[25] S. Swapp. "Scanning Electron Microscopy (SEM)." https://serc.carleton.edu/research_education/geochemsheets/techniques/SEM.html (accessed.

[26] Struers. "ABOUT CUTTING." https://www.struers.com/en/Knowledge/Cutting# (accessed 09.04.2023.
[27] *CONSUMABLE CATALOG*, p. 19. [Online]. Available: https://publications.struers.com/catalogue/consumables-english/?page=18&_ga=2.11691380.11493996.1681046522-2107650265.1676644622.
[28] *Metallic materials Tensile testing Part 1: Method of test at room temperature (ISO 6892-1:2019)*, NS-EN ISO 6892-1:2019, 2019.
[29] Struers. "METALLOGRAPHIC PREPARATION OF COPPER AND COPPER ALLOYS." Struers. https://publications.struers.com/brochures/english/application-notes/copper/?_ga=2.213165204.1442933143.1684021948-2107650265.1676644622 (accessed 17.02.2023.
[30] *Metallic materials - Vickers hardness test - Part 1:: Test method (ISO 6507-1:2018)*, NS-EN ISO 6507-1:2018, 2018.

Appendix

Appendix A - Tensile test results

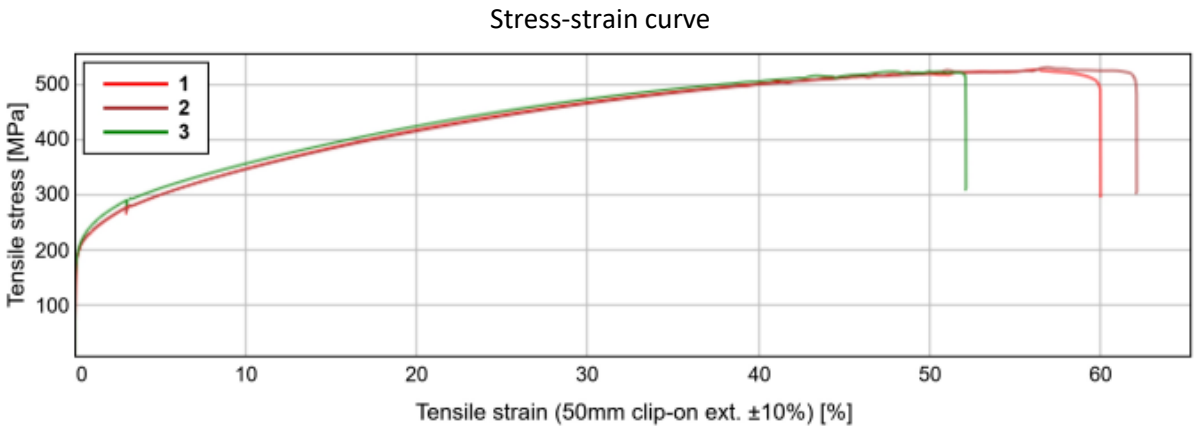

Figure A.1 Stress-strain curve for TT1, TT2 and TT3 (here noted 1, 2 and 3 respectively) generated by Bluehill Universal.

	Modulus (Automatic Young's) [GPa]	Tensile stress at Yield (Offset 0.2 %) [MPa]	Tensile stress at Tensile strength [MPa]	Tensile stress at Break (Standard) [MPa]	% Elongation at tensile strength at Non-proportional elongation (Standard) [%]	% Elongation at break at Non-proportional elongation (Standard) [%]
1	132.00	206.82	526.49	497.17	55.93	59.60
3	195.31	204.23	527.90	506.35	57.30	61.82
4	345.65	203.64	522.56	517.46	47.51	51.75

Table A.1 Stress-strain results for TT1, TT2 and TT3 generated by Bluehill Universal. Number 1, 3 and 4 corresponds to TT1, TT2 and TT3 respectively.

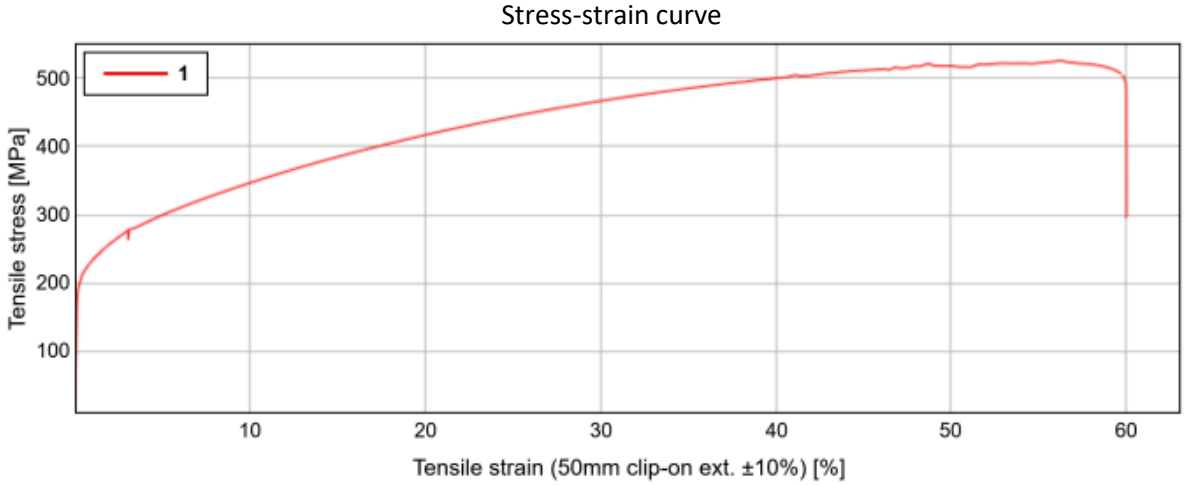

Figure A.2 Stress-strain curve for TT1 generated by Bluehill Universal.

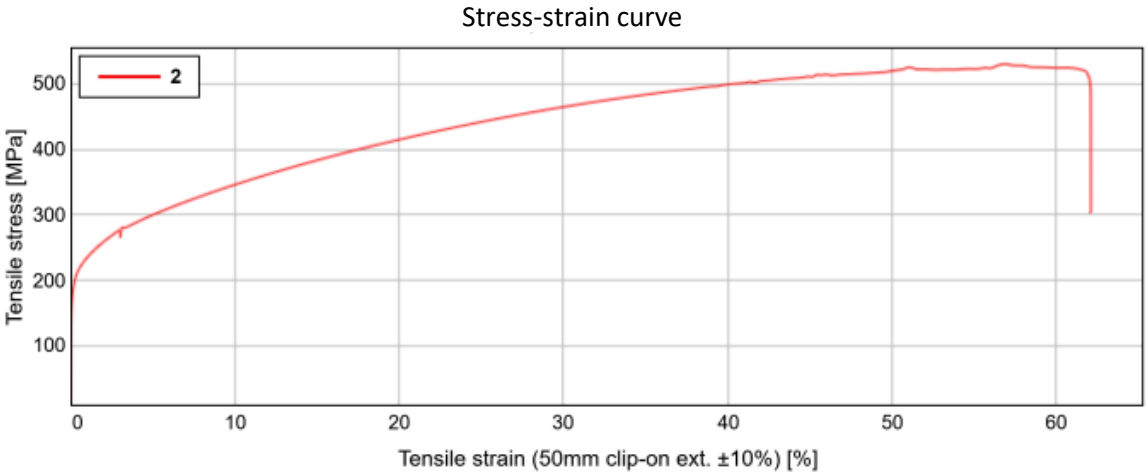

Figure A.3 Stress-strain curve for TT2 generated by Bluehill Universal.

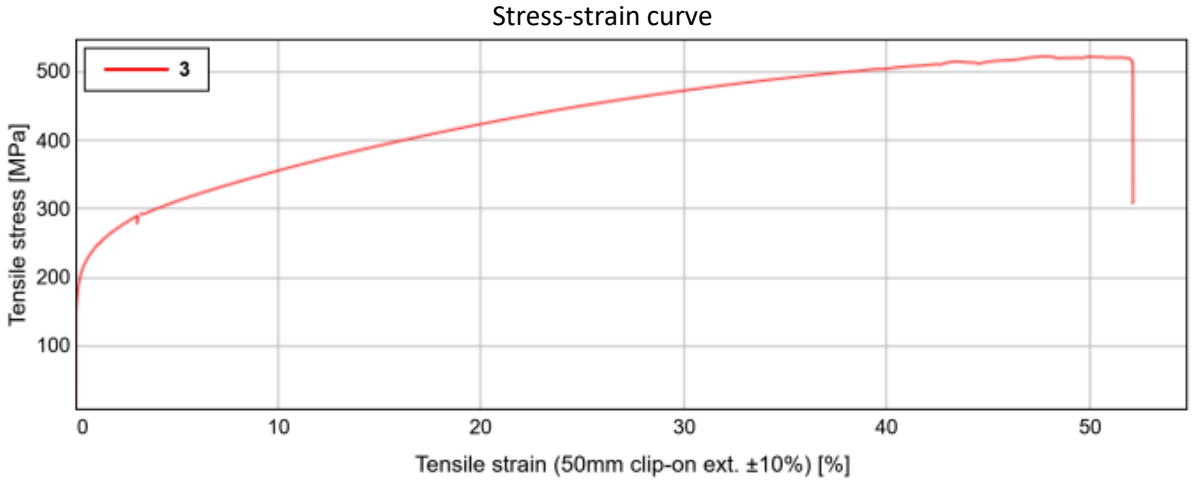

Figure A.4 Stress-strain curve for TT3 generated by Bluehill Universal.

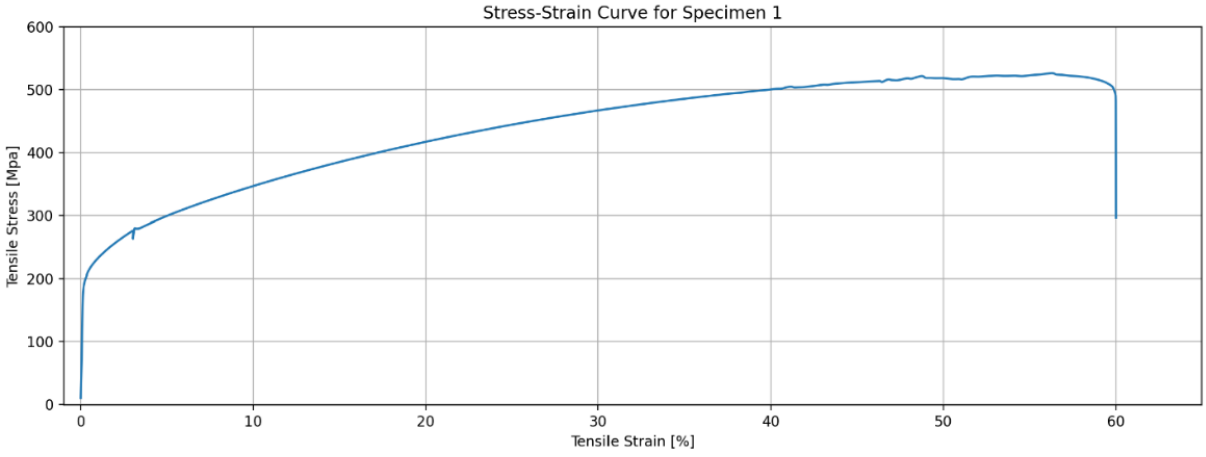

Figure A.5 Stress-strain curve for TT1 generated in Python.

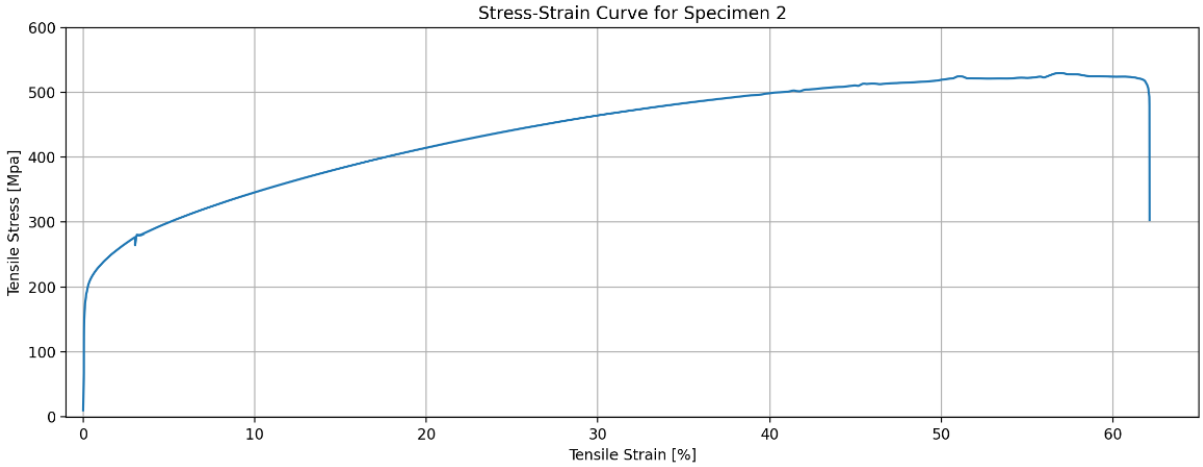

Figure A.6 Stress-strain curve for TT2 generated in Python.

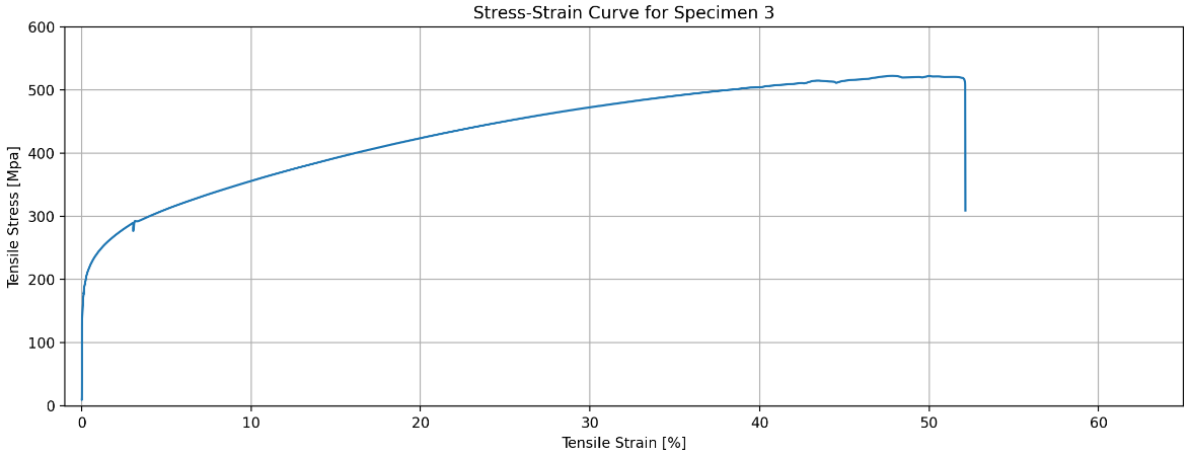

Figure A.7 Stress-strain curve for TT3 generated in Python.

Figure A.8 TT3 placed incorrectly in the testing machine.

Appendix B – Vickers hardness test results

Row 1, Nr:	HV5/10	Row 2, Nr:	HV5/10	Row 3, Nr:	HV5/10	Row 4, Nr:	HV5/10	Row 5, Nr:	HV5/10
1	159.2	10	160.0	19	150.0	29	154.2	36	141.8
2	166.8	11	163.5	20	152.3	30	145.8	37	147.6
3	160.1	12	155.9	21	147.0	31	149.1	38	144.9
4	158.8	13	151.9	22	140.4	32	142.4	39	141.6
5	159.5	14	154.3	23	144.1	33	139.3	40	144.4
6	156.0	15	151.9	24	143.2	34	142.1		
7	162.4	16	152.6	25	143.1	35	143.3		
8	153.7	17	149.8	26	141.7				
9	152.2	18	149.8	27	141.1				

Table B.1 Vickers hardness results for the bottom sample.

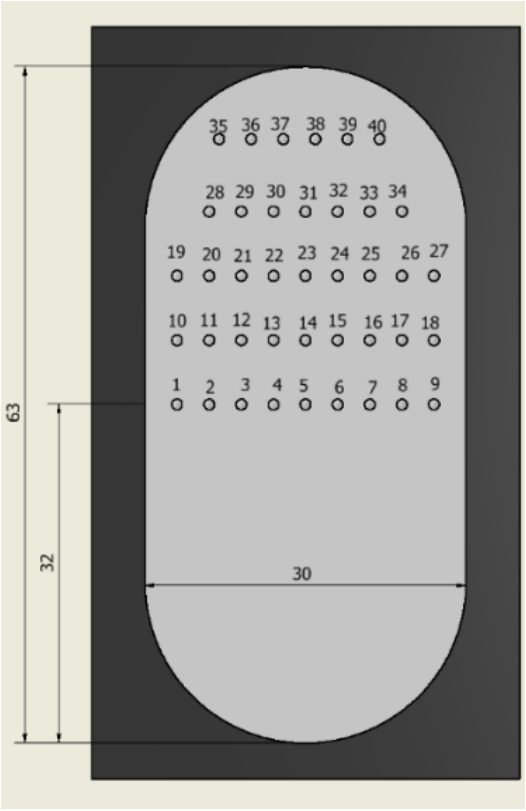

Figure B.1 Illustration of the location of the indenters on the bottom sample.

Appendix C – SDAS calculations

SDAS (unit: mikrometer)							
Sample	Top				Bottom		
	Dendrite 1				Dendrite 1		
	SDAS1	13,5084211			SDAS1	8,0209091	
	SDAS2	13,595			SDAS2	9,7184615	
	SDAS3	11,3671429			SDAS3	11,457143	
	Mean		12,8235213		Mean		9,7321712
	STD		1,26200341				
					dendritt 2		
					SDAS1	9,48	
	Dendrite 2				SDAS2	10,007692	
	SDAS1	10,55					
	SDAS2	10,9863333			Dendrite 3		
	Mean		10,7681667		SDAS1	11,971429	
					SDAS2	10,142857	
	Dendrite 3				SDAS3	11,090909	
	SDAS1	9,07			Mean		11,068398
	SDAS2	8,54545455					
	Mean		8,80772727		Dendrite 4		
					SDAS1	9,43	
	Dendrite 5				SDAS2	9,7825	
	SDAS1	13,2885714			SDAS3	11,97625	
	SDAS2	14,5788889					
	Mean		13,9337302		Dendrite 5		
					SDAS1	10,768571	
	Dendrite 6				SDAS2	11,946667	
	SDAS1	10,7746667					
	SDAS2	8,92307692			Dendrite 6		
	SDAS3	11,8			SDAS1	9,1611111	
	SDAS4	9,25			SDAS2	9,429	
	Mean		10,1869359		SDAS3	6,3636364	
					Dendrite 7		
	Dendrite 7				SDAS1	8,0245455	
	SDAS1	12,1			SDAS2	7,5	
	SDAS2	12			SDAS3	7,5	
	SDAS3	12,8909091					
					Dendrite 8		
					SDAS1	9,2352941	
	Dendrite 8				SDA2	7,2727273	
	SDAS1	11,78			SDAS3	9,8333333	
	SDAS2	9,5					
	SDAS3	12					
					Dendrite 9		
					SDAS1	8,5263158	
	Dendrite 9				SDAS2	9,5789474	
	SDAS1	9,58333333			SDAS3	10,071429	
	SDAS2	9,82055556					
	SDAS3	6,63636364			Dendrite 10		
						7,56125	
						7,622	
	Dendrite 10					6,3333333	
	SDAS1	13,1433333					
	SDAS2	13,32625					
	Dendrite 11						
	SDAS1	10,1428571					
	SDAS2	7,13157895					
		Top				Bottom	
	TOTAL MEAN	11,0112591				9,2787968	
	TOTAL STD	2,06892198				1,6294502	

Table C.1 SDAS calculation

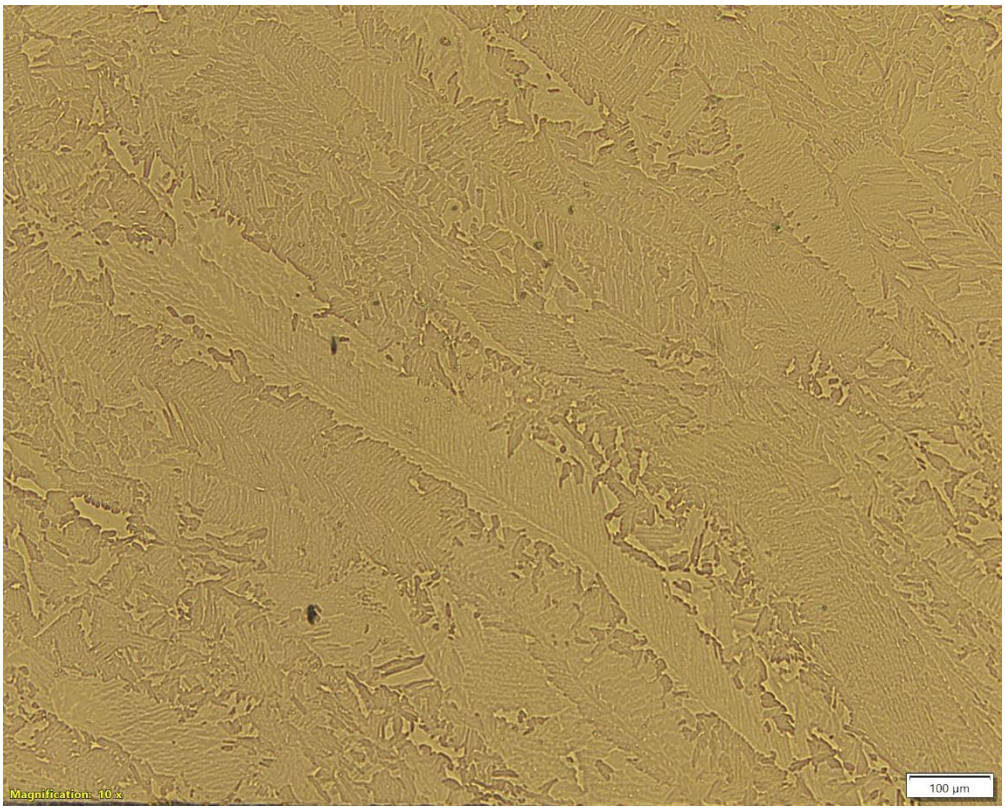

Figure C.1 Dendritic structure in the bottom sample.

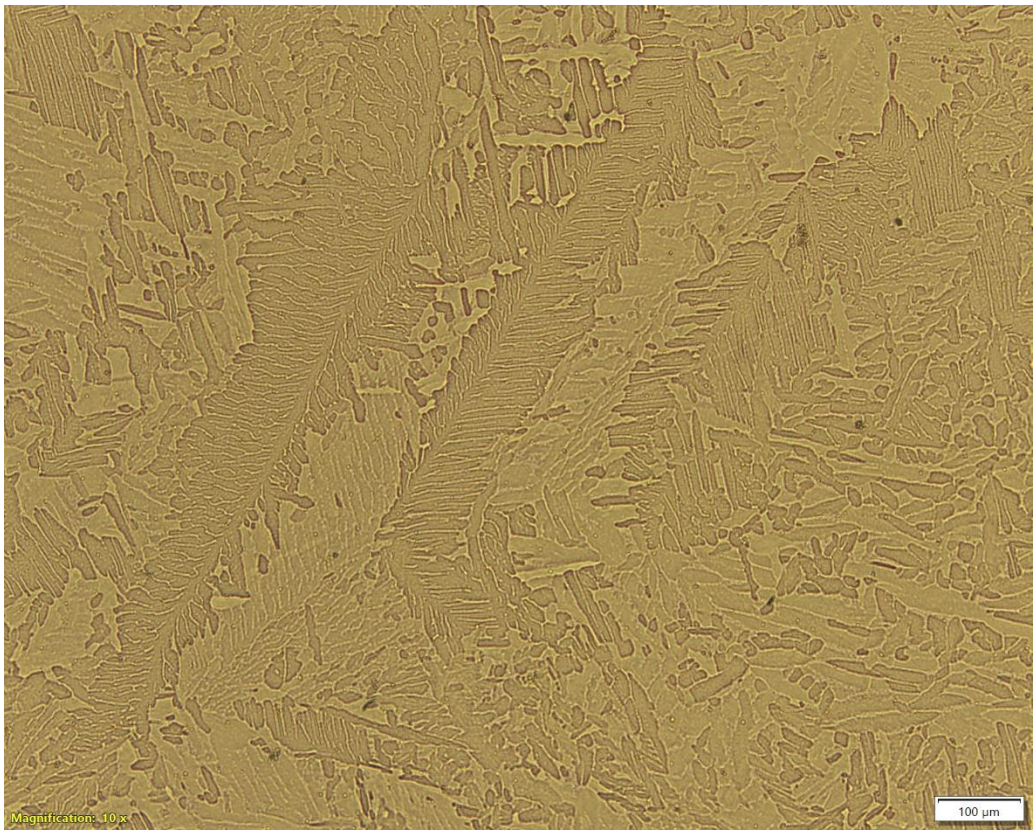

Figure C.2 Dendritic structure in the top sample.

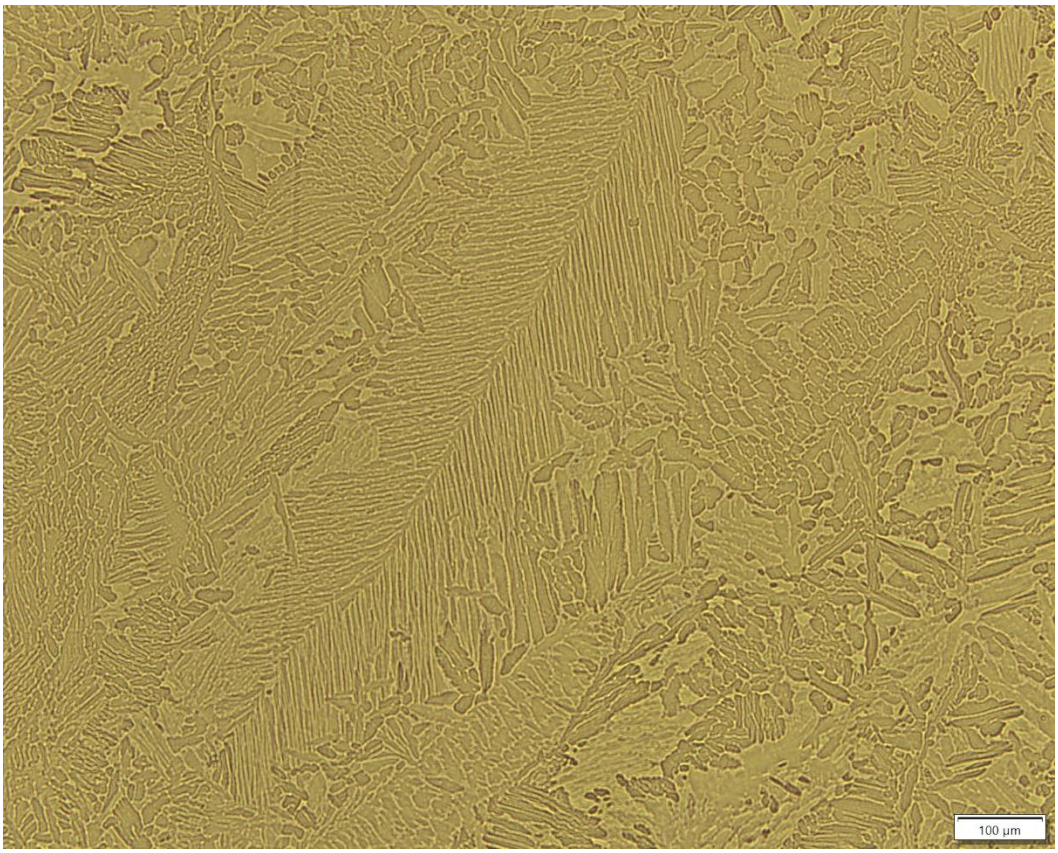

Figure C.3 Dendritic structure in the bottom sample.

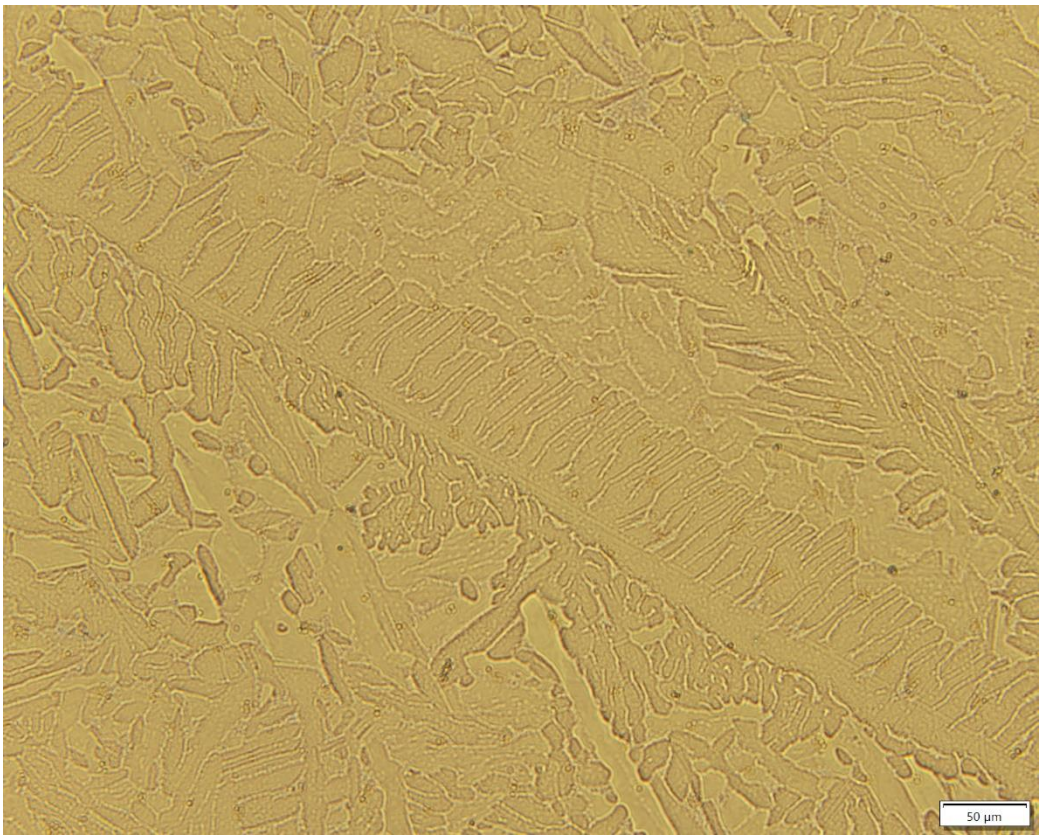

Figure C.4 Dendritic structure in the bottom sample.

Appendix D - SEM images of the bottom sample (xy-plane)

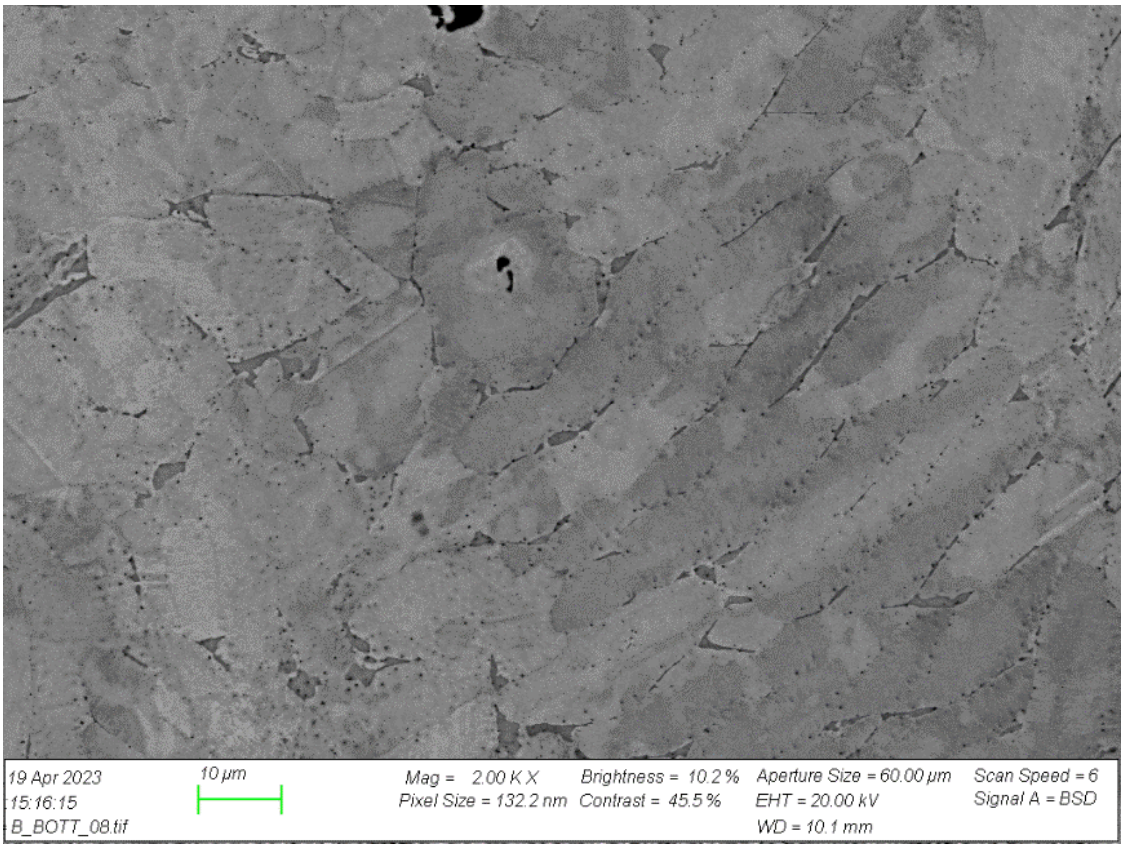

Figure D.1 SEM image

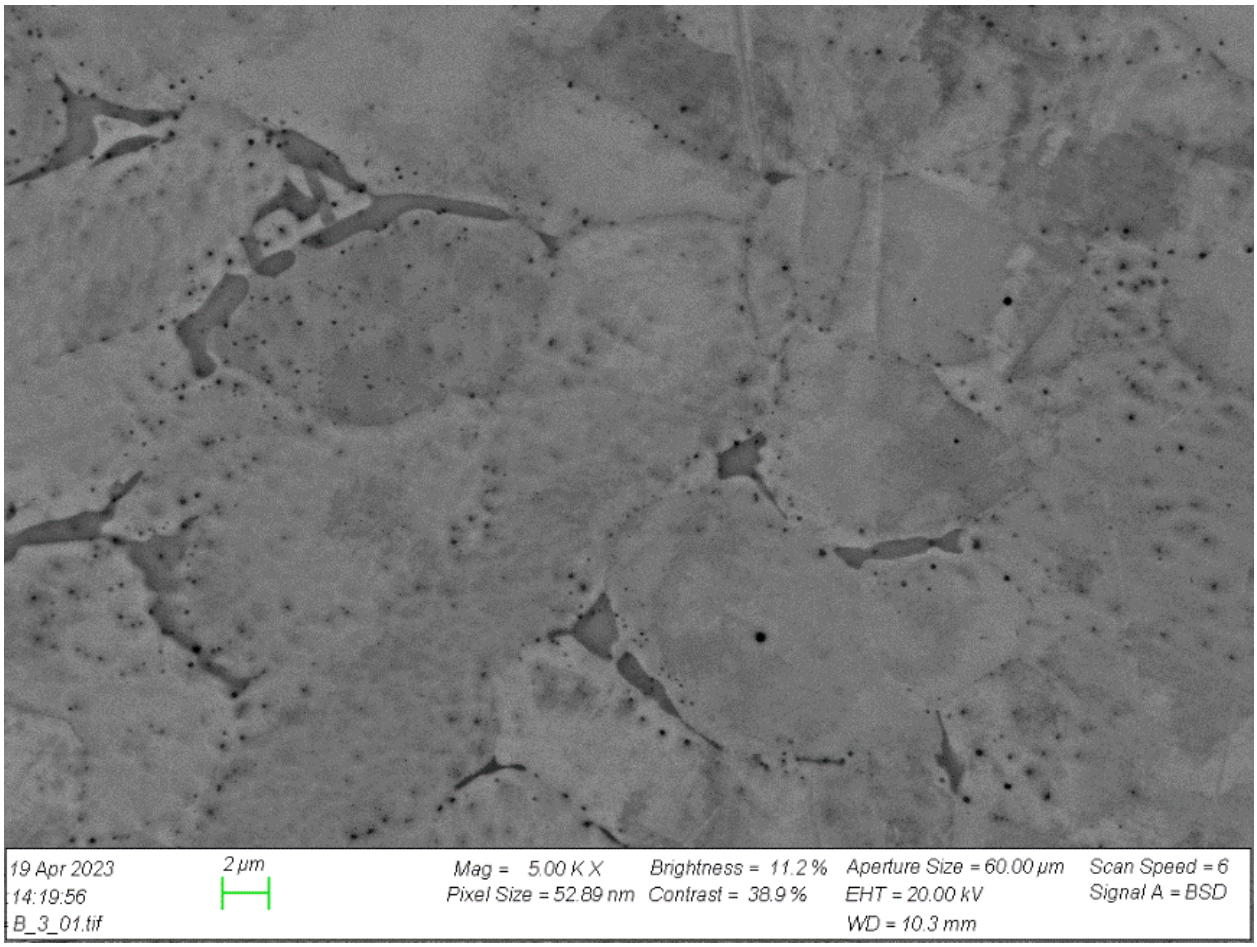

Figure D.2 SEM image

Appendix E - EBSD analysis of grain size in top and bottom sample

```
# Header: Project1::Pattern::CI>0.1::Auto GS (diameter)   10/24/2011
#
Chart:  Grain Size (diameter)

Edge grains included in analysis

Column 1: Diameter [microns]
Column 2: Area Fraction
2.62946; 0.000440538;
3.30526; 3.21334e-005;
4.15475; 0.000184508;
5.22258; 0.000727665;
6.56484; 0.00349528;
8.25208; 0.0112301;
10.373; 0.0214164;
13.0389; 0.033823;
16.3901; 0.0483193;
20.6025; 0.0705566;
25.8976; 0.084347;
32.5536; 0.0947924;
40.9203; 0.105778;
51.4373; 0.113272;
64.6573; 0.0655521;
81.275; 0.0932573;
102.164; 0.0978793;
128.421; 0.0388679;
161.427; 0.0671308;
202.915; 0.0488977;
 ;  ;
Average;  ;
Number; 19.417;
Area; 65.9522;
 ;  ;
Standard Deviation;  ;
Number; 17.6066;
Area; 52.1892;
```

Figure E.1 Grain size (diameter) for the top sample from the EBSD analysis

```
# Header: Project1::Pattern::CI>0.1::Auto GS (diameter)   10/24/2011
#
Chart:  Grain Size (diameter)

Edge grains included in analysis

Column 1: Diameter [microns]
Column 2: Area Fraction
2.62946; 0.000440538;
3.30526; 3.21334e-005;
4.15475; 0.000184508;
5.22258; 0.000727665;
6.56484; 0.00349528;
8.25208; 0.0112301;
10.373; 0.0214164;
13.0389; 0.033823;
16.3901; 0.0483193;
20.6025; 0.0705566;
25.8976; 0.084347;
32.5536; 0.0947924;
40.9203; 0.105778;
51.4373; 0.113272;
64.6573; 0.0655521;
81.275; 0.0932573;
102.164; 0.0978793;
128.421; 0.0388679;
161.427; 0.0671308;
202.915; 0.0488977;
 ;  ;
Average;  ;
Number; 19.417;
Area; 65.9522;
 ;  ;
Standard Deviation;  ;
Number; 17.6066;
Area; 52.1892;
```

Figure E.2 Grain size (diameter) for the bottom sample from the EBSD analysis